Decoherence and Error Correction: Topics in Quantum Computing

by

Vickram Narayn Premakumar

A dissertation presented in partial fulfillment of
the requirements for the degree of

Doctor of Philosophy (Physics)

at the
UNIVERSITY OF WISCONSIN-MADISON
2019

Date of final oral examination: July 26, 2019

The dissertation is approved by the following members of the Final Oral Committee:
Robert Joynt, Professor, Physics
Mark Friesen, Senior Scientist, Physics
Jeffrey Schmidt, Faculty Associate, Physics
Deniz Yavuz, Professor, Physics
Eric Bach, Professor, Computer Science

Abstract

This dissertation investigates problems concerning decoherence and error correction in quantum computer architectures. First we discuss Evanescent-Wave Johnson Noise as a decoherence mechanism. A classical analogy between the Green's functions relevant to describing this noise is used in order to simplify calculations and present results focusing on geometries relevant for small devices. We apply this to model qubit decoherence in the presence of EWJN showing that it could be the dominant noise mechanism for spin qubits in magnetic fields $B \approx 1$ T.

We then turn our attention to characterizing spatial noise correlations in existing qubit devices and strategies to optimize circuit design using correlation information. The concept can be viewed as a Ramsey experiment conducted in a two-dimensional product qubit subspace, allowing us to use many single qubit noise spectroscopy techniques to measure spatial correlations. This is a generalization of decoherence-free subspaces, which have been studied substantially as passive error correction. Next, we describe how to use knowledge of the correlations to choose the best circuit out of many candidates for doing a particular task. The proposed metrics produce predictions on which circuit will result in the highest fidelity under a given noise model, which we verify using numerical simulations.

We demonstrate that a known procedure for coherent-error correction can be made fault tolerant by insisting that C_kNOT gates occur in a single time step. Justification for the simulation of these gates via classical ancillas combined with the Gottesman-Knill theorem is presented by proving that the ancilla and data registers are separable before correction operations. We produce a threshold for an example code on the same order of magnitude as previous work, but with a refined implementation that is fault tolerant.

We continue with the use of redundant syndrome extraction in stabilizer codes to cir-

cumvent majority-rules decision making for conditional operations. We produce simulations comparing the two schemes across a range of models characterized by the independent error rates on qubits and measurements. The most robust realization of this scheme for several codes resemble balanced incomplete block designs, and we explore this correspondence towards generating new codes from designs.

Acknowledgments

The path towards this degree would not have been as enriching and enjoyable without the mentorship of my doctoral advisor, Robert Joynt. I thank him for unreservedly sharing his enthusiasm, knowledge, and season tickets with me over the years. It has truly been a joy to work with you.

I would also like to thank other members of our department Mark Friesen, Mark Eriksson, and Susan Coppersmith for providing invaluable feedback and connections in the quantum computing community to promote the ideas in this work towards reaching people who can make use of them.

Many other physicists provided guidance to me as temporary advisors, course instructors, and collaborators in research. Specifically, I want to thank Maxim Vavilov and Jeff Schmidt for leading many courses that helped me discover subfields of physics that ignited my passion. Additionally, I thank Deniz Yavuz who helped me enormously as I explored new interests in the early stages of my graduate career.

To my fellow students: your camaraderie and unique insightfulness on a variety of topics shaped my interest and abilities in myriad ways. In particular I thank Yuan-Chi Yang, Ekmel Ercan, Danny Crow, Sam Neyens, Alex Cole, Neil Campbell, and Chad Bustard.

A special gratitude goes to my family and friends for their unyielding support and love throughout my time in Wisconsin. As role models and motivators of my education, my parents and elder sister are without parallel. They continually inspire me to devote the necessary hard work, courage and curiosity to grow professionally and personally. My partner, Colleen, has known me longer than almost all of these people and she continues to be everything I need.

Funding Acknowledgments

Unless otherwise stated, this research was sponsored by the Army Research Office (ARO), and was accomplished under Grant Number W911NF-17-1-0274. The views and conclusions contained in this document are those of the authors and should not be interpreted as representing the official policies, either expressed or implied, of the Army Research Office (ARO), or the U.S. Government. The U.S. Government is authorized to reproduce and distribute reprints for Government purposes notwithstanding any copyright notation herein.

Contents

Introduction

The genesis of a quantum computer that conclusively overshadows the computational capabilities of classical architectures has been the motivator for an enormous research effort in the years since Richard Feynman's first proposal on the subject [1]. Interest and development in the project has accelerated, resulting in a variety of implementations, applications, and protocols each of which comes with its own merits and drawbacks. Central to all of these are potential pitfalls that result from the coupling of the physical qubits that make up the computer to the environment. Peter Shor introduced the notion of quantum error correction, showing that the effects of these errors can be arbitrarily reduced by using a suitable encoding of many physical qubits into one logical qubit. This allows a prepared configuration of qubits to persist, effectively storing a quantum memory. However, meaningful quantum operations require not only retaining information, but manipulating it. Protection against the various detrimental effects of this noise can occur at many levels of abstraction. The qubits themselves, the ways in which a single logical qubit is encoded in several, and the particulars of the dynamics of a computation can all be chosen to avoid decoherence.

From the experimental perspective, a slew of different physical manifestations of quantum systems have been used as candidate qubits. Solid state quantum computers offer readily scalable methods of fabrication while superconducting circuits provided the platform for several successful demonstrations of novel algorithms [2, 3]. There are a wealth of quantum error correction (QEC) strategies which leverage the celebrated threshold theorems [4, 5] to handle the faultiness of a computation. Some of the most conceptually interesting schemes fall under the category of Stabilizer codes [6], utilizing group theory to protect information stored in global operators from local disruptions. Despite the power and elegance of these schemes, an important milestone still lies beyond the frontier. The successful demonstration

of a qubit array which can take advantage of QEC to protect quantum information is a realistic and significant near-term goal.

In this thesis, we explore a cross-section of problems associated with handling errors at each of the conceptual strata mentioned above. Our focus is broadly the development of high-fidelity fault-tolerant logical qubits and operations. Chapter 1 focuses on noise at the fundamental level of physical qubits. Spatial noise correlations and optimization of dynamics in existing qubit devices form the subject of Chapter 2. Chapters 3 and 4 focus on stabilizer quantum error correction.

In the first chapter, we consider the effect of residual fields resulting from the random thermal and quantum fluctuations of charge carries in conductors on nearby quantum systems. In analogue to more traditional concepts, we call this Evanescent-Wave Johnson Noise (EWJN). A useful analogy between stochastic field correlation functions and classical electrodynamics is inverted to provide a generalizable strategy for these calculations. The resulting analytic descriptions of noise for many geometries that replicate components in solid state devices are provided, supplemented with numerical simulations where simplifying assumptions are no longer valid. We replicate some well known results to review the field and demonstrate the usefulness of our classical analogy. A framework for utilizing these descriptions to predict qubit dynamics in proximity to conducting surfaces is built up via multipole expansion. We conclude with a comparison to modern experiments, pointing out a distinct signature of EWJN allowing rapid characterization of these fields and a regime in which we expect EWJN to be the dominant noise mechanism.

Chapter 2 outlines strategies to measure and utilize the spatial field correlations in existing qubit devices and circuit designs. We focus on the application to spin qubits in silicon and are able to show experimental results from the implementation of our idea. We begin by describing the protocol and expected results in some reasonable test cases. Assuming a quasistatic Gaussian noise model, we develop analytic results to extract the pairwise statistical correlation and field strengths at various locations in a multi-qubit system using our proposed measurement and a few traditional qubit metrics. We then develop some new metrics generalizing the concept of decoherence-free subspaces to analyze different circuit designs for performing common quantum algorithms to predict which will produce the most pristine

dynamics. We simulate the evolution of these systems and compare them to our proposed metrics across a wide range of noise models to demonstrate the utility of our method. Finally, we propose an extension of this idea to many qubits, making an analogy to random walks in state space.

In Chapter 3 we rectify an ambiguity in the field of coherent error correction. We begin by reviewing fault-tolerance, a central facet of error correction, and its relevance to the situation in coherent error correction, which makes liberal use of entangling gates to condition correction operations on the state of an ancillary set of qubits. We show that previously proposed circuits are not sufficient under a more realistic set of assumptions and demonstrate a need for focusing the scope of these strategies. Using these refinements, we propose a new guiding principle for choosing a circuit to do measurement-free error correction. In order to study this we must extend the typical techniques of classical simulations of quantum circuits relying on a result concerning entanglement of data and ancilla qubits, which we prove.

Chapter 4 investigates a strategy for producing fault-tolerant QEC implementations by taking advantage of the group-theoretic nature of stabilizer codes. By measuring elements of the stabilizer group beyond a set of generators we find that repetition of syndrome extraction is not necessary. We perform calculations varying the rate of physical qubit and syndrome extraction errors independently to show in what regions of parameter space the redundant syndrome extraction schemes outperform the more traditional majority-rules approach. We then draw parallels between the experimental design notion of balanced incomplete block designs and QEC. We produce constraints on the parameters describing a block design allowing us to see which of these objects can be realized as stabilizer codes, showing that the (still incomplete) catalog of designs is a rich source of qubit encodings.

Evanescent-Wave Johnson Noise

0.1 Introduction

The prospect of quantum computing has inspired many designs for the manipulation of small coherent quantum systems - qubits. In order to define and manipulate these objects, they are placed close to small electrodes which often contain many mobile charges and spins. The thermal and quantum motion of these charges and spins creates random electromagnetic fields that can couple to and decohere the qubits, an effect that impedes the controllable dynamics necessary for meaningful computations. This noise is a species of Johnson noise.

J.B. Johnson discovered this noise in 1927 in the course of a research program to improve the performance of amplifiers [7]. H. Nyquist soon explained it theoretically using ingenious applications of equilibrium thermodynamics to thought experiments [8]. When the general relation of fluctuation and dissipation was discovered by H.B. Callen and T.A. Welton in 1951, they regarded their fluctuation-dissipation theorem (FDT) as a "Generalized Nyquist Relation" [9]. The later, more general, theory of linear response of Kubo developed out of the FDT [10]. This is an interesting example of important and general basic science coming from research on very specific technological issues.

The Nyquist formula is

$$\left\langle V^2 \right\rangle_\omega = 2k_B T \; R\left(\omega\right) \tag{1}$$

where

$$\left\langle V^2 \right\rangle_\omega = \int_{-\infty}^{+\infty} dt \; e^{i\omega t} \left\langle V\left(0\right) V\left(t\right) \right\rangle . \tag{2}$$

Here V is the voltage drop between the ends of a resistor with a possibly frequency-dependent resistance R. The angle brackets are an average over the stationary random process that

V represents. The rms voltage noise $\sqrt{\langle V^2 \rangle_\omega}$ is the quantity usually quoted (in units of volts per root Hertz), since it is often practical to measure the drop with a bandpass filter in a frequency range where R is more or less constant. Johnson himself verified that this formula holds independent of the shape, size, or constitution of the resistor. These days, Eq. (1) is recognized as the high-temperature limit of the more general formula

$$\left\langle V^2 \right\rangle_\omega = \hbar\omega \coth\left(\hbar\omega/2k_BT\right) \; R\left(\omega\right) \tag{3}$$

that follows from the quantum-mechanical version of the FDT. For applications to qubits we need a generalization of the Nyquist form of the FDT, which gives the voltage drop between two points in a resistor. In particular, we need a theory that works between any two points irrespective of whether they are on a resistor; we would also like to understand the connection between the Nyquist relation with that other famous kind of thermal electromagnetic field - blackbody radiation. Quantum field theory gives the needed generalization. The main difficulty is to formulate finite-temperature quantum electrodynamics in such a way that the only inputs required are the macroscopic electric and magnetic response functions $\varepsilon\left(\vec{r},\omega\right)$ and $\mu\left(\vec{r},\omega\right)$. The outputs of the theory are the noise spectral densities, which are the field fluctuations at a single spatial point (sufficient to calculate the decoherence of point qubits), and the noise correlation functions which give the fluctuations at spatially separated points (required to calculate the decoherence of extended qubits). We will give precise definitions of these quantities below. The formalism required to do this was constructed in the 1950s by Lifshitz [11] and Rytov [12, 13] and the theory was further developed by Agarwal [14]. These authors built on earlier work of Casimir [15]. An accessible treatment is given by Lifshitz and Pitayevskii [16]. There is a fairly large literature on the application of this formalism to heat transfer and friction in small devices which has been reviewed by Volokitin and Persson [17].

Before proceeding with the development of the formalism, we first give a qualitative picture of how we expect noise to leak out of metallic device elements, taking the lead from a paper of Pendry [18]. Consider a piece of metal surrounded by an insulator. For the sake of argument, let us specify that the metal is hotter than its environment. The

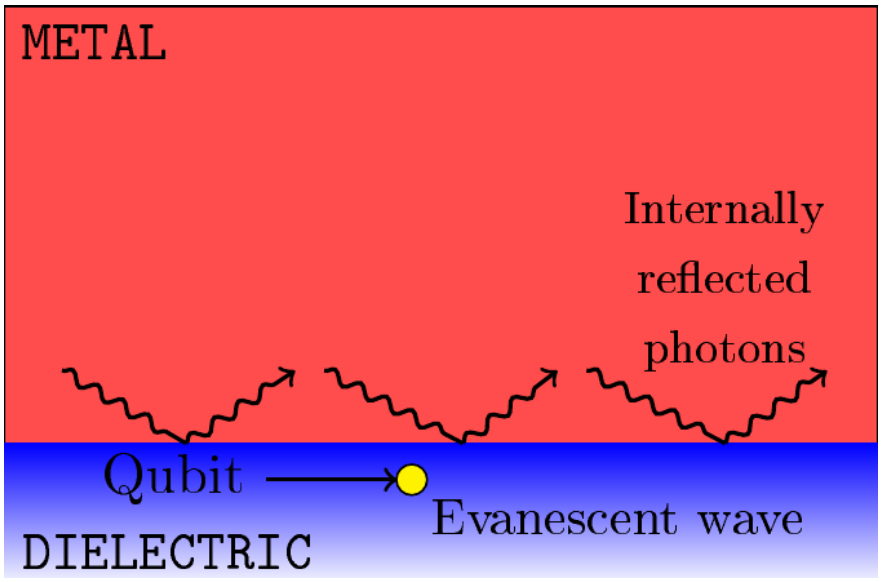

Figure 1: A cartoon depicting evanescent-wave Johnson noise near the surface of a conductor.

Stefan-Boltzmann formula tells us that the total EM power radiated depends only on the surface area and the temperature of the object, not on its conductivity. The radiation is the result of photons thermally generated in the metal leaking out through the surface. The metal has a dielectric function $\varepsilon(\omega) = 1 + 4\pi i\sigma/\omega$, where the conductivity σ nearly always satisfies $\sigma/\omega \gg 1$ (and this is true for all frequencies considered in this work). $|\varepsilon|$ is much greater than unity, so the speed of light (to the extent that it can be defined for the highly overdamped modes of the metal) is small relative to the surrounding insulator. This immediately implies that the photon density of states and the equilibrium density depends on σ. This presents a paradox, since the radiated power is independent of σ. This paradox is resolved by the realization that a high photon density of states is always accompanied by a high probability of internal reflection of the photon [19, 20]. The cancellation of these effects gives the universal coefficient of blackbody radiation. However, internal reflection is always accompanied by an evanescent wave (Fig. 1). This in turn implies that there will be strong Johnson noise near a metallic surface for any material having $|\varepsilon| \gg 1$. This is called evanescent-wave Johnson noise (EWJN). This physical picture tells us that the proper treatment of boundary conditions will be very important. This in turn implies that for ordinary, non-magnetically active metals, the behavior of electric noise is quite different from magnetic noise, since magnetic fields can penetrate those materials much more easily.

It is very important to distinguish between EWJN and the more commonly discussed circuit Johnson noise (CJN). If we consider two separate metallic elements in a small device, usually the path of least resistance between them runs through the external circuit. Thus CJN is a physical effect that involves two or more device elements that convey information about the external circuit to the qubit. EWJN, in contrast, is an effect that occurs even without the external circuit, and fundamentally arises from individual device elements. CJN and EWJN thus come from different physical sources. For the most part, they can be calculated separately and they are basically additive. EWJN is also distinct from charge noise and any other noise that comes from localized defects. The noise sources of EWJN need not be macroscopic, but their dimensions must be large enough that a dielectric function can be defined by the usual coarse-graining procedure of classical electrodynamics. Atomic-scale defects must be treated by different methods.

The implications of Johnson noise for decoherence of atomic qubits were first discussed by Henkel and collaborators [21, 22] , in the context of heating of trapped ions by the walls of the trap. The local noise spectral densities for both electric and magnetic fields relevant to the situation of point qubits near a conducting half-space were calculated and loss and decoherence rates were extracted. These predictions were quantitatively verified in experiments that measured losses from magneto-optical traps [23]. The lifetimes in the experiments are of order 10 s and the distances from the walls 10 to 100 μm. At about the same time, other qubit applications were discussed by Sidles et al. [24]. In semiconductor and some other solid-state implementations of quantum computing, the distance scales are much less than in the atom experiments and this suggests that the effects of Johnson noise could be appreciable for those systems [25, 26, 27, 28, 29, 30]. Indeed, a recent experiment with a diamond film containing NV centers on a silver substrate demonstrated decoherence of qubits due to EWJN in a very direct and quantitative fashion [31].

Charge quantum dot qubits displayed lifetimes in the range of $T_1 \sim 10$ ns, which was shorter than expected based on decoherence mechanisms such as coupling to phonons [32, 33, 34, 35]. This spurred theoretical work on CJN for double quantum dots [36], and even though it appears that it cannot be the main mechanism in this instance, the effects are still appreciable.

There has been a small amount of work on the very interesting topic of noise from micromagnets implanted in semiconductors [19, 20]. However, in this chapter we shall deal only with non-magnetic materials, so the magnetic permeability $\mu = 1$ everywhere. We focus exclusively on EWJN. We cover only analytic calculations and physical considerations. Numerical calculations on realistic devices are not included. To our knowledge, no such calculations exist at present, though the calculations in Ref. [19] represent a start in this direction. It would be a major development project to modify existing FEM software to compute EWJN, since the number of coupled equations is large. However, the formal developments in Sec. 2.2 may suggest ways to simplify the problem.

The literature at present only contains analytic results for the half-space, single film [37], and two-film geometries. In the next section we outline the basic formalism of EWJN. Sec. 2 describes how to apply the results to compute lifetimes of qubits. Sec. 3 gives the applications to electric field noise and decoherence of charge qubits. Sec. 4 is a parallel discussion for magnetic field noise and spin qubits. Sec. 5 gives the current situation with regard to comparison of theory and experiment. Sec. 6 gives a summary and describes the implications for future qubit designs.

The overall structure of the chapter is meant to reflect the logical development of the subject, with reasonably complete derivations of the main results. If the reader's main concern is just with new results, then these are to be found as follows.

- We present exact analogies to equivalent problems in classical electromagnetic theory that greatly simplify the calculations in Sec. 2.2.

- We provide explicit results for the noise spectral density that determines the decoherence of point qubits for new geometries. We find that for the conducting cylinder and electrode, the spectral densities exhibit anisotropies. These anisotropies can serve as a sharp criterion for the presence of EWJN. They can also be exploited to substantially increase T_1 and T_2 by suitable qubit orientation. These results are found in Secs. $4.1 - 4.3$ and $5.1 - 5.3$.

- We compute noise correlation functions that are needed for the determination of decoherence times for extended qubits. These results are found in Secs. $4.1 - 4.3$ and

5.1 – 5.3.

- We describe in detail how to apply these noise calculations to compute relaxation and decoherence times for qubits in the noise field. These results are found in Sec. 3.1 and 3.2.

Overall, the comparisons with present experimental results indicate that EWJN is not the dominant relaxation mechanism for many charge qubit implementations. On the other hand, the observed relaxation time for certain spin qubits can be explained by the calculations we present here.

0.2 General Formalism

Photon Green's Functions

We consider a system at temperature T and regard the dielectric function $\varepsilon(\vec{r},\omega)$ as given. As stated above, $\mu = 1$ everywhere so $\vec{B} = \vec{H}$. We will work in the realm of macroscopic electrodynamics, i.e., all quantities are averaged over distances of order a, where a is an interatomic distance. This excludes a large class of physical situations that can be important in qubit devices, namely those in which the noise sources are few in number or otherwise cannot be be considered as members of a continuum. The results here do not apply to such situations.

Our derivation in this section follows Ref. [16]. We present it here to introduce the concepts and to establish notation.

We shall work in the temporal gauge where the scalar potential $\phi = 0$. The retarded photon Green's function is

$$iG_{ij}(\vec{r},t;\vec{r}\,',t') = \Theta(t-t')\left\langle \widehat{A}_i(\vec{r},t)\,\widehat{A}_j(\vec{r}\,',t') - \widehat{A}_j(\vec{r}\,',t')\,\widehat{A}_i(\vec{r},t)\right\rangle. \tag{4}$$

Here $\Theta(x) = 1$ if $x > 0$ and $\Theta(x) = 0$ if $x < 0$. i,j run over x,y,z. The angle brackets represent a thermal ensemble average. The $\widehat{A}$ are photon operators for the vector potential

in the interaction picture. We define

$$G_{ij}\left(\vec{r},\vec{r}\,',\omega\right)=\int_{-\infty}^{\infty}dt\ e^{i\omega t}G_{ij}\left(\vec{r},t;\vec{r}\,',0\right) \tag{5}$$

and this function satisfies an Onsager relation:

$$G_{ji}\left(\vec{r}\,',\vec{r},\omega\right)=G_{ij}\left(\vec{r},\vec{r}\,',\omega\right). \tag{6}$$

Fortunately, we will not need to consider the operator properties of $\widehat{A}$ in detail. Instead, we will derive a differential equation for G. In the presence of a classical current $\vec{J}$, H' is the perturbation to the free-space Maxwell Hamiltonian with

$$H'=-\frac{1}{c}\int J_i\left(\vec{r},t\right)\ A_i\ d^3r, \tag{7}$$

with a summation convention over Cartesian indices. The expectation value of $\widehat{A}_i$ is given by the Kubo formula

$$\left\langle\widehat{A}_i\left(\vec{r},\omega\right)\right\rangle=-\frac{1}{\hbar c}\int G_{ij}\left(\vec{r},\vec{r}\,',\omega\right)\ J_j\left(\vec{r}\,',\omega\right)\ d^3r\,'. \tag{8}$$

In the following, angle brackets and the argument ω will often be omitted.

In many situations electronic length scales such as the mean free path ℓ is much smaller than all the other lengths in the problem and consequently there is a local relation between the electric displacement and the electric field: $\vec{D}\left(\vec{r}\right)=\varepsilon\left(\vec{r}\right)\vec{E}\left(\vec{r}\right)$. Then Maxwell's equation is

$$\nabla\times\vec{B}=\frac{4\pi}{c}\vec{J}-i\frac{\omega}{c}\varepsilon\left(\vec{r}\right)\vec{E}, \tag{9}$$

and the fields are given in this gauge by

$$\vec{B}=\nabla\times\vec{A}\text{ and }\vec{E}=i\frac{\omega}{c}\vec{A}. \tag{10}$$

Thus we have that

$$-\nabla^2\vec{A}+\nabla\left(\nabla\cdot\vec{A}\right)-\frac{\omega^2\varepsilon\left(\vec{r}\right)}{c^2}\vec{A}=\frac{4\pi}{c}\vec{J} \tag{11}$$

which in index notation with the summation convention is

$$\left[-\delta_{ij}\left(\nabla^2+\frac{\omega^2\varepsilon\left(\vec{r}\right)}{c^2}\right)+\partial_i\partial_j\right]A_i=\frac{4\pi}{c}J_j. \tag{12}$$

Since this is true for any J, it implies that

$$\left[-\delta_{ij}\left(\nabla^2+\frac{\omega^2\varepsilon\left(\vec{r}\right)}{c^2}\right)+\partial_i\partial_j\right]G_{ik}\left(\vec{r},\vec{r}\,'\right)=-4\pi\hbar\,\delta^3\left(\vec{r}-\vec{r}\,'\right)\delta_{jk}. \tag{13}$$

The differential operators act on $\vec{r}$, not $\vec{r}\,'$. For a fixed $\vec{r}\,'$ (source position), this is an inhomogeneous partial differential equation when $j=k$ and a homogeneous partial differential equation when $j\neq k$ for the functions G_{jk}. Tangential $\vec{E}$, normal $D=\varepsilon\vec{E}$ and $\vec{B}=\vec{H}$ are continuous at the boundary between different media. We have that $E_i\left(\vec{r}\right)\sim\left(i\omega/c\right)G_{ij}\left(\vec{r},\vec{r}\,'\right)$ and $B_i\left(\vec{r}\right)\sim\varepsilon_{imn}\partial_m G_{nj}\left(\vec{r},\vec{r}\,'\right)$. Hence the boundary conditions at a surface with a discontinuity in $\varepsilon\left(\vec{r}\right)$ with normal vector $\widehat{n}$ are:

$$\begin{aligned}
\epsilon_{ijk}n_iG_{jm} &\quad \text{continuous for all } k,m\\
\varepsilon n_iG_{im} &\quad \text{continuous for all } m\\
\epsilon_{ijk}\partial_iG_{jm} &\quad \text{continuous for all } k,m.
\end{aligned}$$

Now assume that we can solve these differential equations and have the response function G. Then an application of the FD theorem yields

$$\int e^{i\omega(t-t\,')}\left\langle A_i\left(\vec{r},t\right)A_j\left(\vec{r}\,',t\,'\right)\right\rangle\;d\left(t-t\,'\right) \tag{14}$$

$$=\left\langle A_i\left(\vec{r}\right)A_j\left(\vec{r}\,'\right)\right\rangle_\omega \tag{15}$$

$$=-\coth\left(\frac{\hbar\omega}{2k_BT}\right)\times\operatorname{Im}G_{ij}\left(\vec{r},\vec{r}\,',\omega\right). \tag{16}$$

As we will see below, the relaxation of a charge qubit with level separation ω in the neighborhood of $\vec{r}$ and $\vec{r}\,'$ will be determined by a correlation function of the type

$$\left\langle E_i\left(\vec{r}\right)E_j\left(\vec{r}\,'\right)\right\rangle_\omega=-\frac{\omega^2}{c^2}\coth\left(\frac{\hbar\omega}{2k_BT}\right)\operatorname{Im}G_{ij}\left(\vec{r},\vec{r}\,',\omega\right). \tag{17}$$

The relaxation of a spin qubit in the neighborhood of $\vec{r}$ and $\vec{r}\,'$ with level separation ω will be determined by a correlation function of the type

$$\left\langle B_i\left(\vec{r}\right) B_j\left(\vec{r}\,'\right)\right\rangle_\omega = -\coth\left(\frac{\hbar\omega}{2k_BT}\right) \times \epsilon_{ikm}\epsilon_{jnp}\partial_k\partial'_n \operatorname{Im} G_{mp}\left(\vec{r},\vec{r}\,',\omega\right). \tag{18}$$

We shall also have occasion to refer to the mixed correlation function. Thus the single function $\operatorname{Im} G$ yields all the field correlations in the system. This method is general for a closed system. The system is completely specified once the dielectric function $\epsilon(\vec{r},\omega)$ is given everywhere in space.

Physical Analogy

Physical intuition for the meaning of $G_{ik}\left(\vec{r},\vec{r}\,',\omega\right)$, and a practical calculation method, may be obtained by noting the similarity of Eqs. (12) and (13). Place a fictitious point electric dipole $\vec{p}$ at the point $\vec{r}\,'$ The current is

$$\vec{J}^{(f)}\left(\vec{r}\right) = -i\omega\vec{p}\,\delta^3\left(\vec{r}-\vec{r}\,'\right). \tag{19}$$

and the electric field is given by

$$\left[\partial_i\partial_l - \delta_{il}\nabla^2 - \delta_{il}\,\frac{\omega^2\varepsilon\left(\vec{r}\right)}{c^2}\right]\, E_l^{(f)}\left(\vec{r}\right) = p_i\frac{4\pi\omega^2}{c^2}\delta^3\left(\vec{r}-\vec{r}\,'\right). \tag{20}$$

On the other hand, multiplying Eq. (13) by p_k and summing over k we find:

$$\left[\partial_i\partial_l - \delta_{il}\nabla^2 - \delta_{il}\,\frac{\omega^2\varepsilon\left(\vec{r}\right)}{c^2}\right]\, G_{lk}\left(\omega;\vec{r},\vec{r}\,'\right)p_k = -4\pi\hbar\; p_i\;\delta^3\left(\vec{r}-\vec{r}\,'\right). \tag{21}$$

Comparison of Eqs. (20) and (21) says that

$$G_{lk}\left(\omega;\vec{r},\vec{r}\,'\right)p_k = -\frac{\hbar c^2}{\omega^2}E_l^{(f)}. \tag{22}$$

and, using Eq. (17)

$$\langle E_i(\vec{r})\, E_j(\vec{r}\,')\rangle_\omega \;\; p_j = \hbar \coth\left(\frac{\hbar\omega}{2k_BT}\right) \mathrm{Im}\, E_i^{(f)} \text{ (no sum)}. \tag{23}$$

Hence if we wish to find (say) G_{xy}, we solve the fictitious classical problem of an oscillating dipole $\vec{p} = (0, p_y, 0)$ at the point $\vec{r}\,'$ and compute $E_x^{(f)}$ at the point $\vec{r}$. Then

$$G_{xy}(\vec{r}, \vec{r}\,') = -\frac{\hbar c^2}{\omega^2} E_x^{(f)}/p_y. \tag{24}$$

We can compute all 9 components of G in this way.

There is a similar analogy for magnetic fluctuations. The current of a point magnetic dipole $\vec{m}$ at $\vec{r}\,'$ may be written as

$$J_i^{(f)}(\vec{r}) = c\, \varepsilon_{ijk}\, \partial_j \delta^3(\vec{r} - \vec{r}\,') \;\; m_k, \tag{25}$$

which creates a fictitious magnetic field $B^{(f)}(\vec{r}, \vec{r}\,')$ at $\vec{r}$. It is related to G by

$$\frac{1}{\hbar}\epsilon_{ijk}\epsilon_{lmn}\, m_n \partial_i \partial'_m G_{jl}(\vec{r}, \vec{r}\,') = B_k^{(f)}(\vec{r}, \vec{r}\,'). \tag{26}$$

Hence if we wish to find the magnetic correlations, we first solve the fictitious classical problem of the magnetic field $\vec{B}^{(f)}(\vec{r}, \vec{r}\,')$ at the point $\vec{r}$ resulting from an oscillating point magnetic dipole $\vec{m}$ at the point $\vec{r}\,'$. For example, to find the physical magnetic field noise spectral density we place a point magnetic dipole $\vec{m}$ in the jth direction at $\vec{r}\,'$, compute $B_i^{(f)}(\vec{r}, \vec{r}\,')$, and then

$$\langle B_i(\vec{r})\, B_j(\vec{r}\,')\rangle = \frac{\hbar}{m_j} \coth(\hbar\omega/2k_BT)\, \mathrm{Im}\, B_i^{(f)}(\vec{r}, \vec{r}\,'). \tag{27}$$

The Maxwell equations relate $\vec{E}$ at even orders in ω with $\vec{B}$ at odd orders and vice versa, so the theory has two uncoupled sectors. This is the reason that we need the two separate analogies represented by Eqs. (22) and (26).

In the fictitious problem, the equations satisfied by the fields in the vacuum are $\nabla^2 \vec{E}^{(f)} =$

0, $\nabla^2\vec{B}^{(f)}=0$, $\nabla\cdot\vec{E}^{(f)}=4\pi\rho/\varepsilon_d$, $\nabla\cdot\vec{B}^{(f)}=4\pi\vec{J}/c$, and in the metal we have $\nabla^2\vec{E}^{(f)}+2i\delta^{-2}\vec{E}^{(f)}=0$, $\nabla^2\vec{B}^{(f)}+2i\delta^{-2}\vec{B}^{(f)}=0$, $\nabla\cdot\vec{E}^{(f)}=0$, $\nabla\cdot\vec{B}^{(f)}=4\pi\vec{J}/c$, in the quasistatic case. The boundary conditions are that the tangential component of $\vec{E}^{(f)}$ and $\vec{B}^{(f)}$ are continuous at the interface of dielectric and metal, while the normal component $E_n^{(f)}$of $\vec{E}^{(f)}$ satisfies $(4\pi i\sigma/\omega)\,E_n^{(f)}(m)=\varepsilon_d E_n^{(f)}(d)$, where $E_n^{(f)}(m), E_n^{(f)}(d)$ is the normal component of E in the metal (respectively, the dielectric) as the surface is approached. σ is the DC conductivity of the metal. ε_d is the dielectric constant in the dielectric material. These results show that the quantum and thermal fluctuations of the electromagnetic field can be computed solely using the methods of classical electrodynamics. Furthermore, they suggest that it may be possible to modify standard FEM software tools to compute EWJN.

The dipole analogy makes clear at a formal level that the physics of EWJN is closely related both the image charges and to van der Waals forces. The currents induced by the fictitious dipole can be thought of as a distributed fluctuating image charge, much as we think of the induced currents in the van der Waals attraction.

Quasistatic Approximation

The subject of this chapter is the random electric and magnetic fields that decohere qubits in the neighborhood of small metallic objects. The characteristic frequencies for the decoherence rarely exceed a few GHz, so we restrict our attention to frequencies at or below this range. For this reason we employ the quasistatic approximation from the start, setting the vacuum wavevector $k=\omega/c=0$. In the interior of a metal object with conductivity σ the characteristic length scale of the fields is the skin depth $\delta=c/\sqrt{2\pi\sigma\omega}$. The inverse skin depth $\delta^{-1}=c/\sqrt{2\pi\sigma\omega}$ is proportional to $\sqrt{(\sigma/\omega)}k\gg k$ and it is retained in the theory. For example, the term $\omega^2\varepsilon(\vec{r})/c^2$ in Eq. (12) can be neglected when $\vec{r}$ is in the dielectric or vacuum where $\varepsilon\sim 1$ but not when $\vec{r}$ is in the metal. In this approximation, radiation fields are neglected. We assume that the Drude model is a good approximation for the metals in question, and that $\omega\ll 1/\tau$, where τ is the relaxation time of electrons in the metals. The dielectric function is always approximated as $\varepsilon=4\pi i\sigma/\omega$.

Nonlocal Effects

We focus on the cases where local response is valid. Roughly speaking, this is when the distance of $\vec{r}$ and $\vec{r}\,'$ from the nearest metal surface is greater than the electron mean free path in the metal. However, when the distance to the metal tends to zero, the local expressions for noise strengths diverge, which is clearly unphysical. For completeness, we briefly outline how to include nonlocality in the theory. Generally $\vec{D}\left(\vec{r}\right)$, the electric displacement, depends on $\vec{E}\left(\vec{r}\,'\right)$ according to $D_i\left(\vec{r},t\right) = \int d^3r\,'\,\varepsilon_{ij}\left(\vec{r}-\vec{r}\,',t-t\,'\right)E_j\left(\vec{r}\,',t\,'\right)$ and when Fourier transformed this becomes $D_i\left(\vec{k},\omega\right) = \varepsilon_{ij}\left(\vec{k},\omega\right)E_j\left(\vec{k},\omega\right)$. Eq. (13) becomes

$$\left(-\delta_{ij}\nabla^2+\partial_i\partial_j\right)G_{ik}\left(\vec{r},\vec{r}\,'\right)-\delta_{ij}\frac{\omega^2}{c^2}\int d^3r''\varepsilon_{im}\left(\vec{r},\vec{r}\,''\right)G_{mk}\left(\vec{r}\,'',\vec{r}\,'\right) \tag{28}$$

$$=-4\pi\hbar\delta^3\left(\vec{r}-\vec{r}\,'\right)\delta_{jk}. \tag{29}$$

Use of this equation with an appropriate choice for $\varepsilon\left(\vec{r},\vec{r}\,''\right)$ cures the unphysical divergence at small distances. In practice, to date only the problems of a conducting half-space and conducting films have been treated using the nonlocal formalism [30, 29, 37].

0.3 Application to Qubits

In this section we treat relaxation and dephasing of qubits. Relaxation is due to absorption or spontaneous emission of a photon, the latter being thought of as a an electromagnetic mode of a metallic object. Dephasing is due to modulation of the energy level separation of a qubit by random electromagnetic fields.

Relaxation

A qubit system in a noisy environment is described by a Hamiltonian $H = H_q + H_n(t)$ where H_q admits two eigenstates $|0\rangle, |1\rangle$ such that $H_q|i\rangle = \epsilon_i|i\rangle$. The relaxation rate for such a

qubit in the presence of EWJN is given by the Golden Rule-type formula

$$\frac{1}{T_1} = \frac{1}{\hbar^2}\int_{-\infty}^{\infty} \overline{\langle 0|H_n(t)|1\rangle \langle 1|H_n(0)|0\rangle} e^{-i\omega t} dt \tag{30}$$

Consider a qubit with charge, mass, and g-factor e, m, and g respectively placed in a time dependent electromagnetic field described by $\vec{A}(r,t)$. The full Hamiltonian is

$$H = \frac{1}{2m}\left(\vec{\Pi} - \frac{e}{c}\vec{A}\right)^2 + V(\vec{r}) - \frac{eg}{2m}\vec{B}\cdot\vec{S}, \tag{31}$$

where $\vec{\Pi} = -i\hbar\nabla$. Here we will restrict ourselves to $\mathcal{O}(e)$ so the Hamiltonian can be written

$$H = \frac{\vec{\Pi}^2}{2m} + V(\vec{r}) - \frac{e}{2mc}\left(\vec{\Pi}\cdot\vec{A} + \vec{A}\cdot\vec{\Pi}\right) - \frac{eg}{2m}\vec{B}\cdot\vec{S}. \tag{32}$$

Imposing the gauge condition $\phi = 0$ we find a Hamiltonian readily treated in the interaction picture. The charge distribution generating the noise is contained in the metal, so at a nearby qubit we have $\nabla\cdot E = \nabla^2\phi + \frac{1}{c}\partial_t(\nabla\cdot\vec{A}) = 0$. For finite frequency noise, this implies $\nabla\cdot\vec{A} = 0$, and thus $[\vec{\Pi}, \vec{A}(\vec{r})] = -i\hbar\nabla\cdot\vec{A}(\vec{r}) = 0$. The time dependence of the system is entirely due to the electromagnetic noise and the static Hamiltonian $H_q = \frac{\vec{\Pi}^2}{2m} + V(\vec{r})$. We are left with

$$H = H_q + H_n(t) \tag{33}$$

$$H_n(t) = -\frac{e}{mc}\vec{A}(r,t)\cdot\vec{\Pi} - \frac{eg}{2mc}\vec{B}(r,t)\cdot\vec{S}. \tag{34}$$

Our interaction Hamiltonian can be written as a spatial Taylor series as follows

$$H_n(t) = -\frac{e}{mc}\left[A_i(0,t) + \left(\nabla_j A_i(r,t)\right)_{r=0} r_j + \dots\right]\Pi_i - \frac{eg}{2mc}B_i S_i. \tag{35}$$

This allows us to treat the relevant matrix elements term by term in multipole moments, as described in [38]. Truncating the series at second order and evaluating the off-diagonal matrix elements gives us

$$\frac{1}{T_1^E} = \frac{1}{\hbar^2}\langle p_i\rangle\langle p_l\rangle^* \langle E_i(\vec{r})E_l(\vec{r}\,')\rangle_\omega \quad ; \quad \frac{1}{T_1^B} = \frac{1}{\hbar^2}\langle m_i\rangle\langle m_l\rangle^* \langle B_i(\vec{r})B_l(\vec{r}\,')\rangle_\omega \tag{36}$$

$$\frac{1}{T_1^{cross}} = \frac{1}{\hbar^2}\left(\langle p_i\rangle \langle m_n\rangle^* \langle E_i(\vec{r})B_n(\vec{r}\,')\rangle_\omega + \langle m_k\rangle \langle p_l\rangle^* \langle B_k(\vec{r})E_l(\vec{r}\,')\rangle_\omega\right). \tag{37}$$

Above we set $\hbar\omega = \epsilon_1 - \epsilon_0$ via Eq. (30). For brevity we also use $\langle x\rangle \equiv \langle 0|x|1\rangle$ and $\langle F_i(t)F_j(0)\rangle_\omega = \langle F_iF_j\rangle_\omega$. Here we only include dipole contributions; higher order multipole moments and more details of the calculation are treated in the appendix.

In the case of the spin qubit the states $|0\rangle, |1\rangle$ are up and down states of the spin part of the wavefunction. Hence $|0\rangle = |\psi_0\rangle \otimes |\uparrow\rangle$ where $|\psi_0\rangle$ is the orbital part of the wavefunction which is common to both states of the spin qubit. Immediately we see that all the spatial operator matrix elements $\langle p_i\rangle = \langle q_{ij}\rangle = \langle l_i\rangle = 0$. Hence the above expression simplifies to

$$\frac{1}{T_1} = \frac{1}{\hbar^2}\left(\frac{eg}{2m}\right)^2 \langle S_k\rangle \langle S_n\rangle^* \langle B_k(\vec{r})B_n(\vec{r}\,')\rangle_\omega. \tag{38}$$

Spatially localized qubits are defined as those whose spatial extent is much less than the typical wavelength of the noise field. For them, only the local ($\vec{r} = \vec{r}\,'$) noise correlations are needed. For example, a local spin qubit whose and down states are eigenstates of S_z, has a relaxation time given by

$$\frac{1}{T_1} = \left(\frac{eg}{4m}\right)^2 \left(\langle B_x(\vec{r})B_x(\vec{r})\rangle_\omega + \langle B_y(\vec{r})B_y(\vec{r})\rangle_\omega\right). \tag{39}$$

Dephasing

Qubit relaxation is due to the off-diagonal matrix elements $\langle 0|\, H_n\, |1\rangle$ and $\langle 1|\, H_n\, |0\rangle$ of the noise Hamiltonian. The diagonal elements $\langle 0|\, H_n\, |0\rangle$ and $\langle 1|\, H_n\, |1\rangle$ produce dephasing. If the initial state is $\left(1/\sqrt{2}\right)[|0\rangle + |1\rangle]$, and the state at time t is $\left(1/\sqrt{2}\right)\left[|0\rangle + e^{i\phi(t)}\,|1\rangle\right]$ then ϕ is random after a time T_2. The basic formulas for T_2 are as follows. We have

$$\frac{1}{T_2} = \frac{1}{2T_1} + \frac{1}{T_\phi}. \tag{40}$$

where T_ϕ is the dephasing time. For a Johnson-type noise mechanism, the Gaussian approximation for T_ϕ should be very accurate, since many modes of the metal contribute to the noise. T_ϕ is then calculated in the following way. Again let the applied field be in the ith direction. The initial condition is $\phi\,(t=0) = 1$. We then repeatedly measure $X = |0\rangle\langle 1| + |0\rangle\langle 1|$,

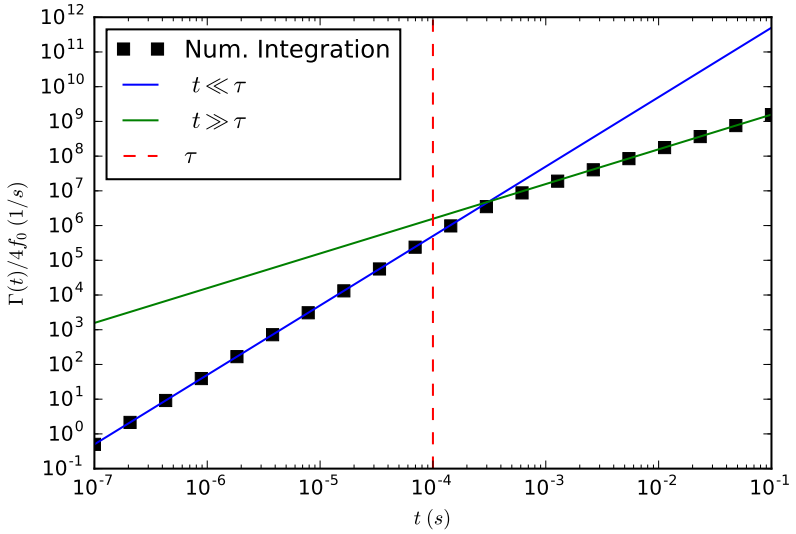

Figure 2: Eq. (42) for $S(\omega) = f_0\ \omega \coth\left(\frac{\hbar\omega}{2k_BT}\right)$ at $T = 0.1$ K and $\tau = 0.1$ ms plotted alongside approximate results for Gaussian noise ($t \ll \tau$) and exponential decay ($t \gg \tau$).

average to get $\overline{X\left(t\right)}$ and the function $\Gamma_i\left(t\right)$ is defined by

$$\overline{X\left(t\right)} = \exp\left[-\Gamma\left(t\right)\right] X\left(0\right) \cos\omega t. \tag{41}$$

and the Gaussian result for $\Gamma\left(t\right)$ is

$$\Gamma\left(t\right) = \frac{t^2}{2} \int_{-\infty}^{\infty} d\omega\ S\left(\omega\right) \frac{\sin^2\left(\omega t/2\right)}{\left(\omega t/2\right)^2}, \tag{42}$$

with

$$\begin{aligned} S\left(\omega\right) = \frac{1}{\hbar^2} \int_{-\infty}^{\infty} dt\ & \overline{\left[\left\langle 1\right| H_n\left(t\right)\left|1\right\rangle - \ \left\langle 0\right| H_n\left(t\right)\left|0\right\rangle\right]} \\ & \times \overline{\left[\left\langle 1\right| H_n\left(0\right)\left|1\right\rangle - \ \left\langle 0\right| H_n\left(0\right)\left|0\right\rangle\right]}\ e^{-i\omega t}. \end{aligned} \tag{43}$$

Evidently we need the diagonal matrix elements of the time-dependent part of the Hamil-

tonian from Eq. (34). Defining moments $p_i = er_i$ and $m_i = \frac{e}{2mc}(l_i + gS_i)$.

$$\begin{aligned}\langle 1|H_n(t)|1\rangle - \langle 0|H_n(t)|0\rangle =& - B_k(t)\left(\langle m_k\rangle_1 - \langle m_k\rangle_0\right) \\ &+ E_k(t)\left(\langle p_k\rangle_1 - \langle p_k\rangle_0\right)\end{aligned}$$

To keep things short let $\Delta x = (\langle 1|x|1\rangle - \langle 0|x|0\rangle)$ for any operator x. The integral kernel becomes

$$\begin{aligned}S(\omega) = \frac{1}{\hbar^2}\big[&\langle B_iB_j\rangle_\omega \Delta m_i\Delta m_j - \langle B_iE_j\rangle_\omega \Delta m_i\Delta p_j \\ &- \langle E_iB_j\rangle_\omega \Delta p_i\Delta m_j + \langle E_iE_j\rangle_\omega \Delta p_i\Delta p_j\big]\,. \end{aligned} \tag{44}$$

In order to make use of Eq. (42) we need to make some mild assumptions on the frequency dependence of the noise spectral density terms. We can write

$$\Gamma(t) = t^2\int_0^{1/\tau} d\omega\ f(\omega)\ \omega\coth\left(\frac{\hbar\omega}{2k_BT}\right)\frac{\sin^2(\omega t/2)}{(\omega t/2)^2}. \tag{45}$$

Again, $f(\omega)$ contains all the information about conductivity, qubit position, device geometry, etc., but it depends weakly on frequency at low frequency, and here we will take it to be independent of frequency $f(\omega) = f_0$ until it falls rapidly to zero at $\omega = 1/\tau$, where τ is the electron relaxation time. We note first that at very short times ($t \ll \tau, \hbar/k_BT$) we always get $\Gamma(t) \sim t^2/t_0^2$ (Gaussian decay), where

$$t_0^2 = \frac{4\tau^2}{f_0}\tanh\left(\frac{\hbar}{2k_BT\tau}\right).$$

As a result, Gaussian decay is only observed when the noise is quasi-static. Exponential decay at longer times is the most important from the standpoint of EWJN. This is where $t \gg \tau$ and $t \gg \hbar/k_BT$ and then we can write

$$\Gamma(t) = 4f_0 \int_0^{t/2\tau} dx \ \coth\left(\frac{\hbar x}{k_B T t}\right) \frac{\sin^2 x}{x}$$
$$\approx 2\pi f_0 \ \frac{k_B T t}{\hbar}.$$

Hence, at any experimentally accessible temperature

$$\frac{1}{T_\phi} = \frac{2\pi f_0 k_B T}{\hbar}. \tag{46}$$

We see that only off diagonal elements of the multipole moments determine T_1 and all of the matrix elements come into the determination of T_2. If the expectation values of the multipole moments are not significantly different between the ground and excited qubit states T_ϕ^{-1} will be small and ${T_2}^{-1} \approx (2T_1)^{-1}$. Even if not, T_1 and T_2 will generally be of the same order of magnitude, which distinguishes EWJN from many other noise mechanisms.

In many experiments, it appears that the noise spectrum has two components, a "$1/f$" component that dominates at low frequencies, and a white component that is bigger at high frequencies. Using the qubit as a spectrometer [39] it has been shown that this happens both in GaAs devices [40] and in Si devices [41]. Echo techniques can mitigate the low-frequency noise but not the more pernicious white part. T_2^{echo} , the decoherence time after echoing, can serve as a diagnostic for EWJN in this situation. The experiment of Ref. [40] is particularly interesting in this regard, since it shows that the white component of the noise has a strong temperature dependence which the $1/f$ part is largely temperature (T) independent, strongly suggesting different origins for the two types of noise. However, T_2^{echo} was proportional to T^{-2} , while Eq. (46) would predict a T^{-1} behavior.

0.4 Electric noise

The noise spectral density $\langle E_i(\vec{r})\, E_j(\vec{r}\,')\rangle_\omega$ generally involves four length scales: $|\vec{r} - \vec{r}\,'|$, the distance over which the correlations are to be measured; d, the distance from the qubit to the conducting object(s); $\delta = c/\sqrt{2\pi\sigma\omega}$, the skin depth in the conductor(s); and L, the

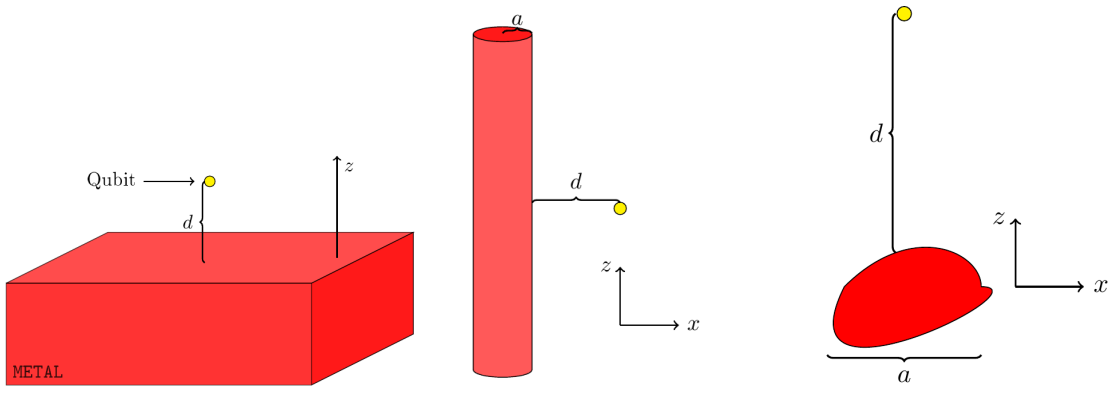

(a) Half Space (b) Cylinder (c) Distant Object

Figure 3: Various qubit system geometries treated in this chapter.

linear size of the conducting object(s). In practice L may be larger or smaller than δ and we give results for both cases where possible. In most cases, the size of the qubit is small, which means that usually the case $\vec{r} \approx \vec{r}\,'$ is of interest, and $|\vec{r} - \vec{r}\,'|$ is the smallest length in the problem. However, qubits can also be extended objects, so we will give formulas as a function of $\vec{r} - \vec{r}\,'$ where possible. As stated above, the vacuum wavelength is always taken to be infinite. The simple geometries treated in this work are shown in Fig. 3.

We will focus first on some limiting cases in which at least one of the other three lengths is very different from the two others.

Half Space

There is a semi-infinite slab of metal with conductivity σ occuping the half-space $z < 0$. We are interested in the electric noise in a dielectric with dielectric constant ϵ at $z < 0$.

Point Qubit

We first focus on some simple methods to compute $G_{ij}\left(\vec{r}, \vec{r}\,' = \vec{r}\right) = \delta_{ij} G_{ii}\left(\vec{r}, \vec{r}\,' = \vec{r}\right)$, which is sufficient for the calculation of the deocherence of a point qubit. This case lends itself to some simple approximations that are physically illuminating. The results in the subsection are well-known [13, 42, 43] and are included here for completeness and to establish notation.

Image Regime To understand this problem physically, we first outline the solution when $d \ll \delta$, since the problem is then essentially elementary. The greater part of the electric field is concentrated within a sphere of radius of order d of the dipole. This implies that inside the metal we have that $\nabla^2 \vec{E} = (-2i/\delta^2)\,\vec{E} \approx 0$, since the skin depth δ may be taken to be large. The problem now reduces to the image problem for a static point charge in a medium with dielectric constant ε_d located at a distance d from a half space with dielectric constant $\varepsilon_m \approx 4\pi i\sigma/\omega$. For $z > 0$ we have the equations $\nabla \cdot \vec{E} = 4\pi\rho = 4\pi\delta^3(\vec{r} - \vec{r}\,')$ and $\nabla \times \vec{E} = 0$. For $z < 0$, we have $\nabla \cdot \vec{E} = 0$ and $\nabla \times \vec{E} = 0$. At the interface we have $\varepsilon_d E_z(z = 0_+) = \varepsilon_m E_z(z = 0_-)$ and $E_{x,y}(z = 0_+) = E_{x,y}(z = 0_-)$. This is the textbook image problem. Hence the solution for $z > 0$ is given by $E = -\nabla\Phi$, with $\Phi_1(\vec{r}) = q/|\vec{r} - \vec{r}\,'| + q'/|\vec{r} - \vec{r}\,''|$ and for $z < 0$ by $\Phi_2(\vec{r}) = q''/|\vec{r} - \vec{r}\,'|$. Here $q' = -q\left[(\varepsilon_m - \varepsilon_d)/(\varepsilon_m + \varepsilon_d)\right]$ and $q'' = q\left[(2\varepsilon_m)/(\varepsilon_m + \varepsilon_d)\right]$. This satisfies the differential equations and the boundary conditions. Hence the textbook image solution carries over to this case.

We will calculate the $\langle E_x(\vec{r})\,E_x(\vec{r})\rangle_\omega$ correlation function first, so we place a fictitious dipole $\vec{p} = p\widehat{x}$ at $\vec{r}\,' = (0, 0, d)$. Then we need the induced field at $\vec{r}$. It is produced by the image dipole $\vec{p}\,'$ at $\vec{r}\,''$:

$$p' = -p\frac{\varepsilon_m - \varepsilon_d}{\varepsilon_m + \varepsilon_d} \approx -p\left(1 + \frac{i\omega\varepsilon_d}{2\pi\sigma}\right) \tag{47}$$

and the field from this is

$$E_x'^{(f)}(\vec{r}) = p'\frac{3(\vec{r} - \vec{r}\,'')_x(\vec{r} - \vec{r}\,'')_x - |\vec{r} - \vec{r}\,''|^2}{|\vec{r} - \vec{r}\,''|^5} = p\left(1 + \frac{i\omega\varepsilon_d}{2\pi\sigma}\right)\frac{1}{(2d)^3} \tag{48}$$

so

$$G_{xx}(\vec{r}, \vec{r}, \omega) = -\frac{\hbar c^2}{\omega^2}\left(1 + \frac{i\omega\varepsilon_d}{2\pi\sigma}\right)\frac{1}{(2d)^3} \tag{49}$$

and using Eq. (22) we find at the position $\vec{r} = \vec{r}\,'$ of the qubit that the physical local noise spectral density is

$$\langle E_x(\vec{r})\,E_x(\vec{r})\rangle_\omega = \hbar\frac{\omega\varepsilon_d}{16\pi\sigma d^3}\coth\left(\frac{\hbar\omega}{2k_BT}\right). \tag{50}$$

which at low temperatures $k_B T \ll \hbar\omega$ reduces to

$$\langle E_x(\vec{r})\, E_x(\vec{r})\rangle_\omega = \hbar\frac{\omega\varepsilon_d}{16\pi\sigma d^3}, \tag{51}$$

and at high temperatures $k_B T \gg \hbar\omega$ to

$$\langle E_x(\vec{r})\, E_x(\vec{r})\rangle_\omega = \frac{k_B T\varepsilon_d}{8\pi\sigma d^3}. \tag{52}$$

Of course cylindrical symmetry implies that $\langle E_y(\vec{r})\, E_y(\vec{r})\rangle_\omega = \langle E_x(\vec{r})\, E_x(\vec{r})\rangle_\omega$.

It is important to note that the electric noise is *inversely* proportional to σ. For really good metals, the screening is complete and there is no dissipation and therefore no fluctuations in the field. It is a general result that the result for $\vec{E}^{(f)}$ depends only on the *ratio* of dielectric constants in the two media, that is, on $(4\pi i\sigma/\omega)/\varepsilon_d$. This follows immediately from inspection of the boundary condition, which is the only place that ε_d enters the calculation. The d^{-3} dependence follows immediately from the physical analogy to the image problem.

Now we will do the $\langle E_z(\vec{r})\, E_z(\vec{r}\,')\rangle_\omega$ correlation function, so we place a dipole $\vec{p} = p\widehat{z}$ at $\vec{r}\,' = (0,0,d)$. Then we need the induced field at $\vec{r}$. The calculation proceeds as for the x direction except for a change in sign of the fictitious image dipole $\vec{p}\,'$ at $\vec{r}\,'' = (0,0,-d)$ with the result that

$$\langle E_z(\vec{r}\,')\, E_z(\vec{r}\,')\rangle_\omega = \hbar\frac{\omega\varepsilon_d}{8\pi\sigma d^3}\coth\left(\frac{\hbar\omega}{2k_B T}\right), \tag{53}$$

which is greater than $\langle E_x(\vec{r}\,')\, E_x(\vec{r}\,')\rangle_\omega$ by a factor of 2. This anisotropy is quite significant for detailed exploration of the theory by experiment.

Induction regime This regime is characterized by the opposite limit $d \gg \delta$. The qubit is far away from the interface on the length scale of the penetration depth. The image problem does not carry over directly since the electric field in the metal satisfies $\nabla^2\vec{E}^{(f)} = (-2i/\delta^2)\,\vec{E}^{(f)}$ in the metal and δ^{-2} cannot be neglected, as it was in the image regime. However, we may now use the fact that the field penetrates only a short distance into the metal, and this allows us to develop a perturbation series in ω for the complex amplitudes

$\vec{E}^{(f)}, \vec{B}^{(f)}$ in the frequency domain. At order ω^0 we have an electric field $\vec{E}^{(f)}$ but $\vec{B}^{(f)}$ vanishes. $\vec{E}^{(f)}$ is the static field from the previous image calculation that is normal to the interface. At order ω^1 there is a magnetic field that corresponds to the static electric field according to the equation $\nabla \times \vec{B} = -i\omega E/c$. To compute $\vec{B}^{(f)}$ at this order we again put a dipole $\vec{p} = p\widehat{x}$ at $\vec{r}\,' = (0, 0, d)$ together with its image dipole $-p\widehat{x}$ at $\vec{r}\,'' = (0, 0, -d)$. This corresponds to a current $\vec{J}(\vec{r}) = p\left(\partial\ \delta^3\left(\vec{r} - \vec{r}\,'\right)/\partial x\right) - p\left(\partial\ \delta^3\left(\vec{r} - \vec{r}\,''\right)/\partial x\right)$. Computing the magnetic field due to this current we have:

$$B_y^{(f)}(z=0) = \frac{-2ipd\omega}{c\left(\rho^2 + d^2\right)^{3/2}} \text{ and } B_z^{(f)}(z=0) = B_x^{(f)}(z=0) = 0, \tag{54}$$

correct to order ω. $B_y^{(f)}$ is continuous at the interface and $\nabla^2 \vec{B}^{(f)} = -2i\delta^{-2}\vec{B}^{(f)}$ for $z < 0$. The crucial point is that since δ^{-2} is large we may neglect the x and y derivatives in both $\vec{B}^{(f)}$ and $\vec{E}^{(f)}$ for $z < 0$ and we have that

$$B_y^{(f)} = \frac{-2ipd\omega}{c\left(\rho^2 + d^2\right)^{3/2}} \exp\left[(1-i)\, z/\delta\right]. \tag{55}$$

Since $\nabla \times \vec{E} = i\omega\vec{B}/c$ for $z < 0$, consistency requires that

$$\frac{\partial E_x^{(f)}}{\partial z} = (1-i)\,\delta^{-1} E_x^{(f)}(z) = i\omega B_y^{(f)}(z)/c \tag{56}$$

at order ω^2. Solving these equations gives

$$E_x^{(f)}(z=0) = \frac{(1+i)\, pd\delta\omega^2}{c^2\left(\rho^2 + d^2\right)^{3/2}}. \tag{57}$$

$E_x^{(f)}$ is continuous at the interface so we also get a correction to the field for $z > 0$ at order ω^2.

For $z > 0$ the field components satisfy the Laplace equation $\nabla^2 \vec{E}^{(f)} = 0$, so we can get the field everywhere by applying Green's theorem to the components of $\vec{E}^{(f)}$ Using Eqs. (22)

and (23) we find

$$\langle E_x(\vec{r})\, E_x(\vec{r})\rangle_\omega = \langle E_y(\vec{r})\, E_y(\vec{r})\rangle_\omega = \frac{\hbar\omega}{8\pi d^2\sigma\delta}\coth\left(\frac{\hbar\omega}{2k_BT}\right) \tag{58}$$
$$\approx \begin{cases} \frac{\hbar\omega}{8\pi d^2\sigma\delta} & \text{for } k_BT \ll \hbar\omega \\ \frac{\hbar\omega}{4\pi d^2\sigma\delta} & \text{for } k_BT \gg \hbar\omega. \end{cases}$$

Since $\delta \sim \frac{1}{\sqrt{\omega\sigma}}$, in the classical limit we have that the noise is proportional to $\sqrt{\omega/\sigma}$, an interesting contrast to the ω/σ dependence in the image regime.

For the z-z correlation function the derivation is only slightly different. We now put a dipole $\vec{p} = p\hat{z}$ at $\vec{r}\,' = (0,0,d)$. $\vec{J}(\vec{r}) = p\left(\partial\ \delta^3\left(\vec{r}-\vec{r}\,'\right)/\partial z\right) + p\left(\partial\ \delta^3\left(\vec{r}-\vec{r}\,''\right)/\partial z\right)$. The result for the noise spectral density is

$$\langle E_z(\vec{r},\omega)\, E_z(\vec{r},\omega)\rangle_\omega = \frac{\hbar\omega}{8\pi d^2\sigma\delta}\coth\left(\frac{\hbar\omega}{2k_BT}\right). \tag{59}$$

This is the same as Eq. (58), so the noise becomes isotropic at large distances from a metal surface.

Summary of Approximate Results for the Point Qubit. The two regimes are distinguished by the relative magnitudes of d and δ - the distance of the source from the half space and the skin depth. The following physical considerations serve as the basis for understanding electric field noise in small devices.

The image regime of small d/δ is fairly easily understood. In the fictitious problem, the electric field penetrates the metal in the same way it does in the textbook case of two dielectrics of strongly different dielectric constants. The field is strongly screened at the surfaces so that the field lines bend sharply at the interface. This field dissipates energy at the usual rate $\sim \sigma\left|\vec{E}\right|^2$ per unit volume in the fictitious problem, and the physical fluctuations are also proportional to this. However, the "impedance mismatch" dominates to the extent that $\left|\vec{E}\right| \sim 1/\sigma$ in the metal overall and the noise spectral density at a given frequency is proportional to $1/\sigma$. The noise is stronger for poor conductors since the field penetrates further. Once the dependence on the conductivity has been determined, the

$1/d^3$ spatial dependence follows by dimensional analysis or noting that the fictitious field is produced by an image dipole.

The induction regime of large d/δ is somewhat different. The electric field outside the metal is, again, essentially normal to the interface. This induces a magnetic field parallel to the interface which penetrates only a distance δ into the metal. This in turn induces an orthogonal electric field parallel to the surface that dissipates energy. The volume in which the energy is dissipated is of thickness δ, so the dissipation is proportional to δ. Thus the image result is reduced by the factor δ/d, and the noise spectral density is proportional to $1/d^2\sqrt{\sigma}$.

Extended Qubits

For extended qubits, we need the full $\vec{r}$ and $\vec{r}\,'$ dependence of G. We compute using a method that will be used repeatedly in what follows. Details are given in the appendix, along with explicit forms for the components of the noise tensors. We place a fictitious dipole $\vec{p} = p\hat{z}$ at $\vec{r}\,' = (0, 0, d)$ and find the induced field

$$\begin{aligned}\vec{E}^{(ind)}(\vec{r}) = -\frac{p}{2\pi}\int d^2q\ \ (-iq_x, -iq_y, q)\ \ e^{-qd} \\ \times \frac{1-(\varepsilon_m/\varepsilon_d)\,q/\alpha}{1+(\varepsilon_m/\varepsilon_d)\,q/\alpha} e^{i\vec{q}\cdot\vec{\rho}} e^{-qz}\end{aligned} \tag{60}$$

for $z > 0$, and the corresponding electric noise is given by Eq. (23):

$$\begin{aligned}\left\langle \vec{E}\,(\vec{r} = (\vec{\rho}, z))\, E_z\,(\vec{r}\,' = (0,0,d))\right\rangle_\omega = -\frac{\hbar}{2\pi}\coth\frac{\hbar\omega}{2k_BT} \\ \times \mathrm{Im}\int d^2q\ \ (-iq_x, -iq_y, q)\ \ e^{-qd}\frac{1-(\varepsilon_m/\varepsilon_d)\,q/\alpha}{1+(\varepsilon_m/\varepsilon_d)\,q/\alpha} e^{i\vec{q}\cdot\vec{\rho}} e^{-qz}\end{aligned} \tag{61}$$

The integral is complicated, but it can be evaluated numerically and it simplifies in the limits of large and small d.

When $d \ll \delta$, $\alpha \approx q$ and we find for the physical noise

$$\left\langle \vec{E}\,(\vec{r})\, E_z\,(\vec{r}\,')\right\rangle_\omega \approx -\frac{\hbar\omega\varepsilon_d}{2\pi\sigma}\coth\frac{\hbar\omega}{2k_BT}\nabla\frac{d+z}{\left[(d+z)^2+\rho^2\right]^{3/2}} \tag{62}$$

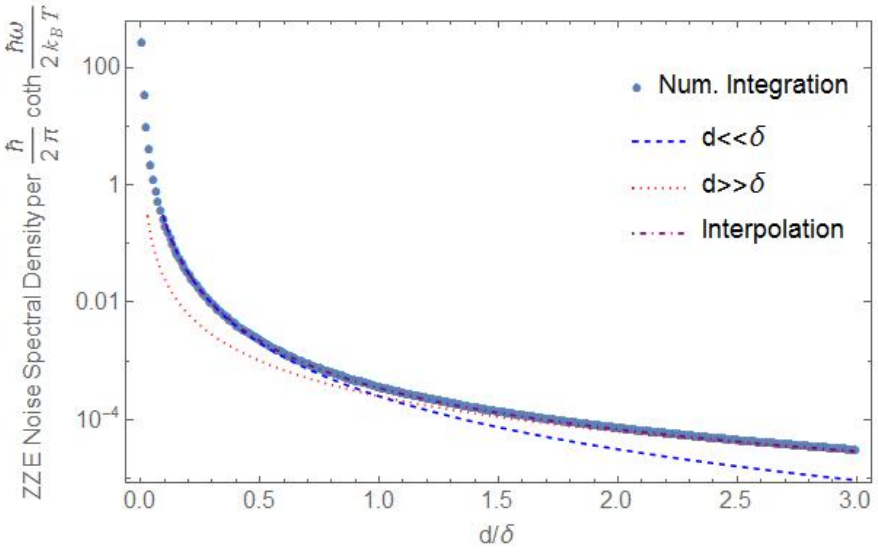

Figure 4: Numerical integration of Eq. (61), the electric noise spectral density for a localized qubit in the half-space geometry, compared with image and induction regime approximate results. $\frac{\sigma}{\omega} = 100$ and $p = 2.17$ for the interpolated function Eq. (67).

The diagonal component of this equation reduces to Eq. (53) when $\vec{r} = \vec{r}\,' = (0, 0, d)$, satisfying an important check. This case has the unusual feature of anticorrelations in E_z for large lateral separations of $\vec{r} - \vec{r}\,'$: $\rho > \sqrt{2}\,(d + z)$. This implies that in the appropriate geometry there can be cancellations in the integral that determines qubit decoherence. This can be incorporated as a design feature.

For $d \gg \delta$ (but still $d \ll \delta\sigma/\omega$) we have $\alpha \approx (1 - i)\,\delta^{-1}$ and the physical noise correlation function is

$$\left\langle \vec{E}\,(\vec{r})\,E_z\,(\vec{r}\,')\right\rangle_\omega = -\frac{\hbar\omega\varepsilon_d}{2\pi\sigma\delta}\coth\frac{\hbar\omega}{2k_BT}\nabla\frac{1}{\left[(d+z)^2+\rho^2\right]^{1/2}} \tag{63}$$

Again, it can be verified that the diagonal component of this equation reduces to Eq. (59) when $\vec{r} = \vec{r}\,' = (0, 0, d)$. The situation for $\langle\vec{E}(r)E_x(r')\rangle_\omega$ is somewhat more complicated because of the lack of cylindrical symmetry. However, the method of the previous section does not depend on the symmetry and it can still be used. We now use $\vec{p} = p\hat{x}$. This leads to a fictitious induced electric field for $z > 0$:

$$\vec{E}^{(ind)}\,(\vec{r}) = -\frac{p}{2\pi}\frac{\partial}{\partial x}\nabla\int d^2q\;\frac{1}{q}e^{-q(d+z)}\frac{1-(\varepsilon_m/\varepsilon_d)\,q/\alpha}{1+(\varepsilon_m/\varepsilon_d)\,q/\alpha}e^{iq_xx+iq_yy} \tag{64}$$

and the physical noise correlation is

$$\left\langle \vec{E}\left(\vec{r}\right) E_x\left(\vec{r}\,'\right)\right\rangle_\omega = -\frac{\hbar}{2\pi}\frac{\partial}{\partial x}\nabla\int d^2q\; e^{-q(d+z)}\,\mathrm{Im}\,\frac{1-\left(\varepsilon_m/\varepsilon_d\right)q/\alpha}{1+\left(\varepsilon_m/\varepsilon_d\right)q/\alpha}e^{iq_x x+iq_y y}\coth\frac{\hbar\omega}{2k_BT}. \quad (65)$$

For $d \ll \delta$ we can calculate the diagonal element of the physical noise spectral density and show it is in agreement with Eq. (50). For $d \gg \delta$ (but still $d \ll \delta\omega/\sigma$) we have

$$\left\langle \vec{E}\left(\vec{r}\right) E_x\left(\vec{r}\right)\right\rangle_\omega = \frac{\hbar}{2\pi}\frac{\omega\varepsilon_d}{\sigma\delta}\nabla\left\{\frac{x}{\rho^2}\left[1-\frac{d+z}{\left[(z+d)^2+\rho^2\right]^{1/2}}\right]\right\}\coth\frac{\hbar\omega}{2k_BT}, \quad (66)$$

and the various components of the tensor may be calculated from this expression.

It is difficult to give detailed physical interpretations of the expressions for nonlocal correlations, other than to point out the dependence on the components of $\vec{r}-\vec{r}'$ has takes the form of inverse power laws consistent with the picture of a fluctuation-induced force.

Between Induction and Image Regimes

In general Eq. (61) cannot be simplified, but in both the image and induction regime we can find analytic results (Eqs. (53) and (59)). Using these two results, we can interpolate a function to compute correlation functions for qubit geometries that do not fall into either of the extremal cases treated here. For two functions f_1 and f_2 we define a family of interpolated functions

$$f_{int}(p) = \left(f_1^p + f_2^p\right)^{\frac{1}{p}} \quad (67)$$

and search for the $p \in \mathbb{R}$ that optimizes the interpolated function's agreement with the extended qubit noise spectral density. The interpolated functions are plotted alongside numerical results for Eqs. (61) and (94) in Fig. 4 and Fig. 6 respectively.

Conducting Cylinder

We consider a infinite conducting circular cylinder (conductivity σ and radius a) with its axis along the z-direction. There is a qubit at the point $\vec{r}\,' = (d, 0, 0)$. We wish to compute $\langle B_i\left(\vec{r}\,'\right) B_i\left(\vec{r}\,'\right)\rangle$ with $i = x, y, z$. We're particularly interested in the anisotropy of relaxation

times, which depend on the ratios of this correlation function for different values of i. The most common case is when the skin depth $\delta \gg a$. We will also be mainly interested in thin wires also in the sense that $d \ll a$. This means that the fictitious applied field is slowly varying over the cylinder. The the problem reduces to a computation of the electric polarizability.

The problem of the *magnetic* polarizability of a conducting cylinder in a uniform field is a standard one [44]. We modify the solution to obtain the electric polarizability $\vec{\beta}$, defined by $P_i = \pi a^2 \beta_i E_i$, where P_i is the electric dipole moment per unit length in direction i. We find

$$\beta_x = \frac{1}{2\pi} \frac{4\pi i\sigma/\omega - C}{4\pi i\sigma/\omega + C} \tag{68}$$

with

$$C = -1 + \frac{kaJ_0(ka)}{J_1(ka)}. \tag{69}$$

and $k = (1+i)/\delta$.

Again, the most interesting case (and the easiest one to calculate) is when $\delta \gg a$, so $|ka| \ll 1$ and

$$\frac{kaJ_0(ka)}{J_1(ka)} \approx ka \frac{1}{ka/2} = 2, \tag{70}$$

and then we find

$$\operatorname{Im} \beta_x = \frac{\omega}{\pi\sigma}. \tag{71}$$

When $d \gg a$ we can integrate along the z-axis assuming uniform applied field. We find

$$\langle E_x(\vec{r}\,') E_x(\vec{r}\,')\rangle = \frac{123\omega\hbar a^2}{256\sigma d^5} \coth\left(\frac{\hbar\omega}{2k_B T}\right) \tag{72}$$

and

$$\langle E_y(\vec{r}\,') E_y(\vec{r}\,')\rangle = \frac{3\omega\hbar a^2}{32\sigma d^5} \coth\left(\frac{\hbar\omega}{2k_B T}\right). \tag{73}$$

We may calculate the noise correlation for the z-direction in the same way. However, end effects are likely to be very important for this case. We present the result as a conjecture

to be investigated in further work:

$$\langle E_z(\vec{r}\,')\,E_z(\vec{r}\,')\rangle = \frac{27\pi\hbar a^4}{2048 d^5\delta^2}\coth\left(\frac{\hbar\omega}{2k_BT}\right). \tag{74}$$

The infinite cylinder geometry differs qualitatively from the other cases considered in that the dimension of the source object in the z-direction is always long compared with δ, while the most interesting case in physical devices is where the radius a and the qubit separation d are short compared with δ. This results in an anisotropy which is not merely a dimensionless geometrical factor but which also depends on δ and therefore on the frequency.

Distant Object

We now treat the electrical noise of a metallic object far away from the qubit ($d \gg L$). We consider a fictitious point dipole $\vec{p}$ at $\vec{r}\,'$, the metallic object approximated by a sphere at the origin and an observation point $\vec{r}$. Eq. (17) gives the correlation function:

$$\langle E_i(\vec{r})\,E_k(\vec{r}\,')\rangle = \hbar\coth\left(\frac{\hbar\omega}{2k_BT}\right)\times \mathrm{Im}\left[\alpha(\omega)\right]\frac{9x_ix_k'\,\vec{r}\cdot\vec{r}\,' + \delta_{ik}r^2r'^2 - 3x_ix_kr'^2 - 3x_i'x_k'r^2}{r^5r'^5}, \tag{75}$$

where now $\vec{E}$ is the physical fluctuating field. The local noise at $\vec{r}$ is

$$\langle E_i(\vec{r})\,E_k(\vec{r}\,'=\vec{r})\rangle = \hbar\coth\left(\frac{\hbar\omega}{2k_BT}\right)\mathrm{Im}\left(\alpha\right)\frac{3x_ix_k+\delta_{ik}r^2}{r^8}. \tag{76}$$

The r^{-6} dependence is familiar from the van der Waals force, which has a similar physical origin.

The *anisotropy* in lifetimes of a qubit in the presence of a spherical electrode is independent of the value of α. If the qubit is located at $\vec{r} = r\hat{z}$, then

$$\langle E_x(\vec{r})\,E_x(\vec{r})\rangle = \langle E_y(\vec{r})\,E_y(\vec{r})\rangle = \hbar\coth\left(\frac{\hbar\omega}{2k_BT}\right)\frac{\mathrm{Im}\left[\alpha(\omega)\right]}{r^6} \tag{77}$$

$$\langle E_z(\vec{r})E_z(\vec{r})\rangle = 4\hbar\coth\left(\frac{\hbar\omega}{2k_BT}\right)\frac{\mathrm{Im}\left[\alpha(\omega)\right]}{r^6}. \tag{78}$$

The anisotropy

$$\langle E_z(\vec{r})\, E_z(\vec{r})\rangle = 4\,\langle E_x(\vec{r})\, E_x(\vec{r})\rangle \tag{79}$$

is stronger than in the half-space case. Thus the problem of noise from a distant metallic object reduces to a calculation of $\mathrm{Im}\left[\alpha(\omega)\right]$, the dissipative part of the polarizability of the electrode. To get α, we need to calculate the change in the charge density of the electrode due to a distant oscillating dipole, and the electric field that results from this charge. We do this now in two limits.

Image Regime We first consider a metallic sphere of radius a with $\delta \gg a$. Once again the fictitious problem is mathematically identical with that of a dielectric sphere in a static field, so we may simply transcribe the textbook formulas for the polarizability:

$$\alpha = \frac{\varepsilon_m/\varepsilon_d - 1}{\varepsilon_m/\varepsilon_d + 2} a^3 \approx \left(1 + \frac{3i\omega\varepsilon_d}{4\pi\sigma}\right) a^3. \tag{80}$$

Hence

$$\langle E_i(\vec{r})\, E_k(\vec{r})\rangle = \frac{3\hbar\omega\varepsilon_d a^3}{4\pi\sigma} \frac{3x_i x_k + \delta_{ik} r^2}{r^8} \coth\left(\frac{\hbar\omega}{2k_B T}\right) \tag{81}$$

For a metallic ellipsoid with radii a_x, a_y, a_z in the x, y, z directions the coordinate system is aligned with the axes of the ellipsoid and the polarizability tensor satisfies $\alpha_{ij} = \delta_{ij}\alpha_{ii}$ with

$$\alpha_{ii} = \frac{1}{3} \frac{\varepsilon_m/\varepsilon_d - 1}{1 + (\varepsilon_m/\varepsilon_d - 1)\, n_i} a_x a_y a_z \approx \left(1 + \frac{i\omega\varepsilon_d}{12 n_i^2 \pi\sigma}\right) a_x a_y a_z. \tag{82}$$

The depolarizing factors n_x, n_y, n_z are positive and satisfy $n_x + n_y + n_z = 1$ and n_i are decreasing functions of a_i. In particular, if $a_x < a_y < a_z$ then $n_x > n_y > n_z$. The connection between the n_i and the a_i involves elliptic integrals. Exact expressions and tables may be found in [45]. Using Eq. (138) we have

$$\begin{aligned}
\langle E_i(\vec{r})\, E_k(\vec{r}\,')\rangle &= \hbar \coth\left(\frac{\hbar\omega}{2k_B T}\right) \mathrm{Im}\left(\alpha_{jj}\right) f_{kj}(\vec{r}\,')\, f_{ij}(\vec{r}) \\
&= \frac{\hbar\omega\varepsilon_d V}{16\pi^2\sigma} \coth\left(\frac{\hbar\omega}{2k_B T}\right) \times \frac{1}{n_j^2} \frac{3x_k' x_j' - \delta_{kj} r'^2}{r'^5} \frac{3x_i x_j - \delta_{ij} r^2}{r^5},
\end{aligned} \tag{83}$$

a distance r from the center of the ellipsoid of volume V. To understand the physics of this

formula, think of a qubit at $\vec{r} = r\widehat{z}$ with the origin of coordinates at the center of the ellipsoid. Then the off-diagonal components of the noise tensor vanish and the formula exhibits the anisotropy mentioned above. This expression confirms the intuition that the noise should be stronger in the directions where the axis is longer, since the polarizability is greater.

Induction regime Again we first consider a metallic sphere of radius a. We find

$$\alpha = \frac{3\,(1+i)\,\omega a^4}{8\pi\delta\sigma} \tag{84}$$

for the polarizability in the induction regime. Using Eq. (76), we have that if the qubit is located at $\vec{r} = r\widehat{z}$, then

$$\langle E_x\,(\vec{r} = r\widehat{z})\,E_x\,(\vec{r} = r\widehat{z})\rangle = \langle E_y\,(\vec{r} = r\widehat{z})\,E_y\,(\vec{r} = r\widehat{z})\rangle = \frac{3\hbar\omega a^4}{8\pi\sigma\delta r^6}\coth\left(\frac{\hbar\omega}{2k_BT}\right) \tag{85}$$

$$\langle E_z\,(\vec{r} = r\widehat{z})\,E_z\,(\vec{r} = r\widehat{z})\rangle = \frac{3\hbar\omega a^4}{2\pi\sigma\delta r^6}\coth\left(\frac{\hbar\omega}{2k_BT}\right). \tag{86}$$

General result The problem of the polarization of a metallic sphere is exactly solvable for all d/δ but it is not trivial. The method may be found in [46], and it is discussed in [47], but seems not to have been solved prior to 2008.

The polarizability α for the sphere of radius a is given by

$$a^{-3}\alpha = -\frac{1}{2}\frac{\kappa^2 a\ j_0 + (1+2\varepsilon)\ \ j_0'}{\kappa^2 a\ j_0 + (1-\varepsilon)\ \ j_0'}. \tag{87}$$

The symbols are defined as $\kappa = (1+i)\,/\delta$, $j_0 = (1/\kappa a)\sin\kappa a$, $j_0' = (1/a)\cos\kappa a - (1/\kappa a^2)\sin\kappa a$.

To obtain the first correction in the case $\delta \gg a$ we expand to first order in ω/σ and a/δ, (always assuming $\omega/\sigma \ll a/\delta$) and find

$$j_0 \approx 1,\ \ j_0' \approx -\frac{1}{3}\kappa^2 a \tag{88}$$

and we have

$$\alpha = a^3\left(1 + \frac{3i\omega}{4\pi\sigma}\right), \tag{89}$$

in agreement with Eq. (80) for the dissipative part. Note that the term that is zeroth-order in ω gives a polarizability $\alpha = a^3$, which is the proper static limit given in many textbooks.

When $\delta \ll a$, then

$$j_0 \approx \frac{i}{2\kappa a} e^{-i(1+i)a/\delta}, \quad j_0{}' \approx \frac{1}{2a} e^{-i(1+i)a/\delta}$$

and

$$\alpha \approx a^3 \left(1 + \frac{3a\,(1+i)\,\omega}{8\pi\sigma\delta}\right). \tag{90}$$

As ω increases, we find that $\operatorname{Im}\alpha$ increases, so it is a monotonic function of ω. The results in this section are easily understood physically, since they correspond to the dissipative part of the van der Waals interaction. This gives the familiar r^{-6} dependence to the fluctuation fields.

Multiple Objects

Real devices tend to have complex geometries with multiple metallic device elements. A modern spin qubit experiment may involve a back gate or an accumulation gate having a layer or half-space shape. There may be up to tens of finger gates for lateral or voltage control that are approximately cylindrical. Clearly a numerical approach is indicated for these cases, which is beyond the scope of this chapter. We therefore limit ourselves to a few remarks.

In many cases, it may be reasonable to regard different metallic elements as noise sources that are statistically independent. If this assumption holds, then

$$\langle E_i\,(\vec{r})\,E_j\,(\vec{r}\,')\rangle_\omega = \sum_{s=1}^{N} \langle E_i\,(\vec{r})\,E_j\,(\vec{r}\,')\rangle_\omega^{(s)}, \tag{91}$$

where the (s) indexes the sources, of which there are N total. The various noise sources add incoherently.

The physical analogy of Sec. 2 shows that this assumption cannot be be strictly correct. The various device elements are in fact all driven by a single fictitious dipole and they are

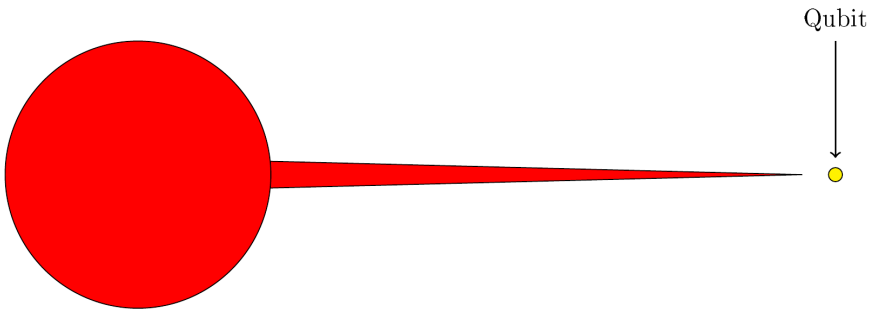

Figure 5: A depiction of the geometry used to model sharp points in device architectures.

therefore in phase. However, unless the qubit occupies a position of high symmetry with regard to at least one pair of metallic objects. This can occur: it is common to place qubits near the tips of opposing finger gates. However, in most other cases the symmetry is low and Eq. (91) can be used.

Sharp Points

A serious concern for qubit decoherence is the geometrical enhancement of noise in the neighborhood of surface asperities of conductors. The question is whether the well-known divergence of local field strengths at such structures carries over to noise. This is not a particularly pressing issue for for semiconductor qubits where gate features are only defined on length scales of 10 nm or longer. But one may also consider tunneling devices closer to scanning tunneling microscopes with much sharper tips. However, it can be seen fairly simply that electric noise is not greatly enhanced by asperities in the case that δ is greater than the size of the surface feature (the usual case). We imagine a spherical geometry with a sharp point added on top, and a qubit near the point (See Fig. 5). Qualitatively, the quasistatic electric field lines will gather at the point, giving the familiar lightning-rod effect. However, these lines are outside the object and they do not produce the dissipation that is associated with field fluctuations and noise. Inside, the magnitude of the field is reduced by a factor ω/σ. This internal field produces currents and it is therefore the field associated with the dissipative part of the response, and, in turn, to the noise strength. These currents run away from the point and give rise to the surface charge $\sigma(\vec{r}\,')$ whose density diverges at the tip as $r^{-1+\nu}$, $\nu = [2\ln(2/\alpha)]^{-1}$, where α is half the opening angle of the tip, taken here

as a cone (*i.e.*, $\alpha = 0$ for an infinitely sharp tip). The presence of the logarithm means that $\nu \ll 1$ even for a very sharp tip. Note $\nu > 0$.

The z component of the fictitious electric field at the point $\vec{r} = (0, 0, -d)$ is proportional to

$$\begin{aligned} E_z^{(f)}(\vec{r}) &\sim \int_0^p d^2 r' \frac{\sigma(\vec{r}\,')(\vec{r} - \vec{r}\,')_z}{|\vec{r} - \vec{r}\,'|^3} \\ &\sim \int_0^p \sin\alpha \; r' dr' \frac{(r')^{-1+\nu}(-d - r'\cos\alpha)}{\left|(r')^2 + d^2 + 2dr'\cos\alpha\right|^{3/2}} \end{aligned} \tag{92}$$

where p is an upper cutoff on the size of the cone. We are only interested in the small d behavior, which follows from simple scaling arguments as $E_z^{(f)} \sim d^{\nu+1/2}$ and this carries over to the physical field fluctuations $\langle E_z(\vec{r}) E_z(\vec{r})\rangle_\omega \sim d^{\nu+1/2}$. So the divergence of the fields as the point is approached along the surface does not carry over to the noise in the immediate region near the tip but outside the conductor.

Charge qubits

To understand qubit decoherence in the presence of noise, the frequency dependence of the noise is of paramount importance. To this end, write the noise spectral density $\langle E_i(\vec{r}) E_j(\vec{r}\,')\rangle$from EWJN as

$$\langle E_i(\vec{r}) E_j(\vec{r}\,')\rangle_\omega = f(\omega) \; \omega \; \coth\left(\frac{\hbar\omega}{2k_B T}\right), \tag{93}$$

where all spatial and device geometry information is contained in $f(\omega)$. For EWJN, $f(\omega) \to f_0$, a constant as $\omega \to 0$. f_0 sets the overall scale of the noise strength. In addition there is a high-frequency cutoff $1/\tau$ at the relaxation time for the conduction electrons in the metal. Thus $f(\omega) \to 0$ when $\omega \gg 1/\tau$. Physically, the factor of ω comes from the connection of noise to dissipation. Photons are non-interacting bosons - hence the cotangent factor. This sort of noise is white, or at least white-ish. This means that echo techniques are not likely to be very useful for extending qubit lifetimes when EWJN is the dominant source of decoherence. This noise is essentially the same as that of the well-known spin-boson

model and the results are well known, so we only briefly summarize results here and give no derivations.

There are three frequency regime for the spectral density. 1. When $0 \leq \omega < 2k_BT/\hbar$, then $\langle E_i(\vec{r})\, E_j(\vec{r}\,')\rangle_\omega = 2k_BTf_0/\hbar$. 2. When $2k_BT/\hbar < \omega < 1/\tau$ we have $\langle E_i(\vec{r})\, E_j(\vec{r}\,')\rangle = f(\omega)\ \omega$, where typically the frequency dependence of $f(\omega)$ is weak. 3. When $\omega > 1/\tau$, then the frequency dependence is material-dependent but we may usually assume that the noise is cut off.

In regime 1, the fluctuations are thermal. Regime 2 is the quantum regime and the linear spectrum is refered to as "ohmic". Regime 3 is above the the high-frequency cutoff, whose presence is implicit here. The symbol σ denotes the DC conductivity; however, no equation in which it appears can be used at frequencies greater than $1/\tau$. This frequency range is generally in the infrared for metals.

The qubit energy level separation is $\hbar\omega_0$ and ω_0 may be in either Regime 1 or Regime 2, depending on the implementation. No existing implementation operates in Regime 3.

0.5 Magnetic Noise

Half Space

For magnetic noise the image method is not useful, so we proceed directly to general results for extended qubits. Again, we are interested in a metal with conductivity σ that occupies the half space $z < 0$. The equations satisfied by the fields are the same as for the electric case. The only difference for magnetic fields is that $\vec{B}$, unlike $\vec{E}$, is continuous at the interface, since we dealing with non-magnetic materials. The derivations for magnetic noise are similar to those for electric noise so we mainly give results

For this problem we place a fictitious magnetic dipole moment $\vec{m}$ at the point $\vec{r}\,' = (0, 0, d)$ and the physical noise spectral density is

$$\left\langle \vec{B}\left(\vec{r}\right) B_z\left(\vec{r}\,'\right)\right\rangle_\omega = \frac{\hbar}{4\pi\delta^2}\coth\frac{\hbar\omega}{2k_BT}\,\mathrm{Im}\int d^2q\frac{1}{q^2}\;\left(q_x,q_y,iq\right)e^{-q(z+d)}e^{iq_xx+iq_yy} \tag{94}$$
$$= -\frac{\hbar}{4\pi\delta^2}\coth\frac{\hbar\omega}{2k_BT}\nabla\int d^2q\frac{1}{q^2}e^{-q(z+d)}e^{iq_xx+iq_yy}.$$

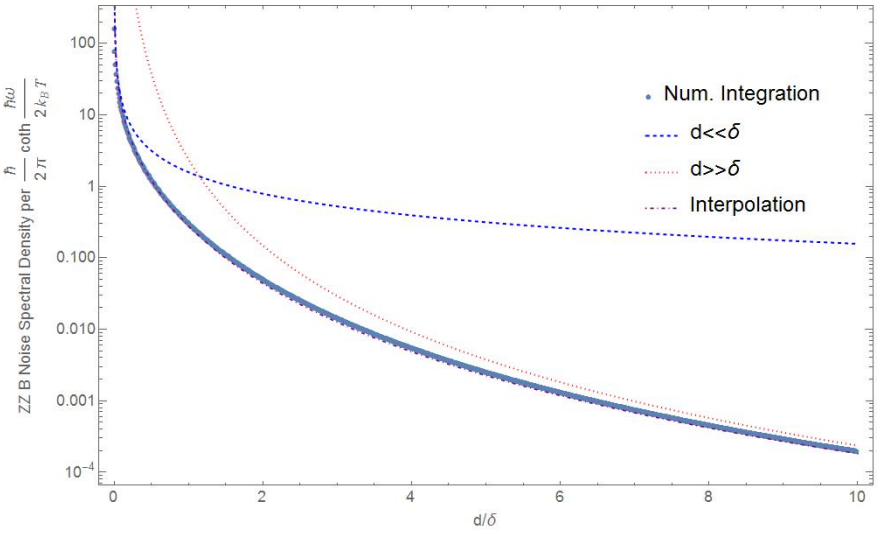

Figure 6: Numerical integration of Eq. (94), the magnetic noise spectral density for a localized qubit in the half-space geometry, compared with image and induction regime approximate results. $\frac{\sigma}{\omega} = 100$ and $p = -0.358$ for the interpolated function Eq. (67).

For a point qubit ($\vec{r} = \vec{r}\,'$) we have

$$\left\langle B_z\left(\vec{r}\right) B_z\left(\vec{r}\right)\right\rangle_\omega = \frac{\hbar}{4d\delta^2}\coth\frac{\hbar\omega}{2k_BT}. \tag{95}$$

And in the high T limit this reduces to

$$\left\langle B_z\left(\vec{r}\right) B_z\left(\vec{r}\right)\right\rangle_\omega = \frac{k_BT}{2\omega d\delta^2}. \tag{96}$$

The $1/d$ dependence comes from integrating the $1/r^3$ behavior of the dipole interaction over the half space. This is in contrast the the $1/d^3$ dependence of the electric field noise. The difference is due to the fact that metals screen electric, but not magnetic, fields. This relatively slow spatial decays is the main reason that magnetic noise is likely to be of more

practical importance in devices. For $d \gg \delta$ we have

$$\frac{1-q/\alpha}{1+q/\alpha} \approx (1 + q\delta + iq\delta), \tag{97}$$

and

$$\left\langle \vec{B}(\vec{r})\, B_z(\vec{r}\,') \right\rangle_\omega = -\frac{\hbar\delta}{2\pi} \coth\frac{\hbar\omega}{2k_BT} \nabla \int d^2q\; q\; e^{-q(z+d)} e^{iq_x x + iq_y y}$$

For a point qubit only the diagonal component is nonzero:

$$\langle B_z(\vec{r})\, B_z(\vec{r})\rangle_\omega = \frac{3\hbar\delta}{8d^4} \coth\frac{\hbar\omega}{2k_BT}. \tag{98}$$

The x-component is more complicated because of the lack of cylindrical symmetry, but the essential procedure is the same. We find

$$\left\langle \vec{B}(\vec{r})\, B_x(\vec{r}\,') \right\rangle_\omega = \frac{\hbar}{2\pi} \coth\frac{\hbar\omega}{2k_BT} \frac{\partial}{\partial x} \nabla\, \mathrm{Im} \int d^2q\; \frac{1}{q} \frac{1-q/\alpha}{1+q/\alpha} e^{iq_x x + iq_y y - q(z+d)}$$

For $d \ll \delta$ this is

$$\left\langle \vec{B}(\vec{r})\, B_x(\vec{r}\,') \right\rangle_\omega = -\frac{\hbar}{2\delta^2} \coth\frac{\hbar\omega}{2k_BT} \frac{\partial}{\partial x} \nabla \int_0^\infty dq\; \frac{1}{q^2} e^{-q(z+d)} J_0(q\rho)$$

At $\vec{r} = \vec{r}\,'$ we have that only the diagonal component is non-vanishing and

$$\langle B_x(\vec{r}\,')\, B_x(\vec{r}\,')\rangle = \frac{\hbar}{8d\delta^2} \coth\frac{\hbar\omega}{2k_BT}.$$

In the high T limit this reduces to

$$\langle B_x(\vec{r}\,')\, B_x(\vec{r}\,')\rangle = \frac{k_BT}{4d\omega\delta^2}.$$

For $d \gg \delta$ we get

$$\left\langle \vec{B}(\vec{r})\, B_x(\vec{r}\,') \right\rangle_\omega = -\hbar\delta \coth\frac{\hbar\omega}{2k_BT} \frac{\partial}{\partial x} \nabla \frac{\partial}{\partial z} \frac{1}{\left[(d+z)^2 + \rho^2\right]^{1/2}}.$$

For $\vec{r} = \vec{r}\,'$ only the diagonal component is nonzero:

$$\langle B_x(\vec{r}\,')\, B_x(\vec{r}\,')\rangle_\omega = \frac{3\hbar\delta}{16\pi d^4}\coth\frac{\hbar\omega}{2k_BT}.$$

In the high T limit this becomes

$$\langle B_x(\vec{r}\,')\, B_x(\vec{r}\,')\rangle_\omega = \frac{3\hbar\delta}{8\pi d^4}.$$

Overall, the most notable difference between electric noise and magnetic noise is that electric noise is screened by a metal and magnetic noise is not. This accounts for the $1/d$ dependence in the $d << \delta$ case for magnetic noise. This relatively slow decline in strength suggests that magnetic noise is, somewhat counter to intuition, more like to be important in small devices. This will be confirmed in Sec. 6 where comparisons to experiment are presented.

Cylinder

In this section, we consider a infinitely long conducting circular cylinder as a source of EWJN. The cylinder has conductivity σ and radius a and its axis is along the z-direction. This geometry is important, since cylindrical microwave antennas are used for single qubit rotations. There is a qubit at the point $\vec{r}' = (d, 0, 0)$. We wish to compute $\langle B_i(\vec{r}')\, B_i(\vec{r}')\rangle$ with $i = x, y, z$. We're particularly interested in the anisotropy of relaxation times, which depend on the ratios of this correlation function for different values of i. The most common case is when the skin depth $\delta \gg a$. We will also be mainly interested in thin wires also in the sense that $d \gg a$.

We need the solution to the problem of the magnetic polarizability of a conducting cylinder in a uniform field. This is given by [44]. The polarizabilities α_i are defined by the

formulas

$$M_x = \pi a^2 \alpha_x B_x$$
$$M_y = \pi a^2 \alpha_y B_y$$
$$M_z = \pi a^2 \alpha_z B_z,$$

where M_i is the magnetic moment per unit length in direction i. Here

$$\alpha_x = \alpha_y = -\frac{1}{2\pi}\left[1 - \frac{2}{ka}\frac{J_1(ka)}{J_0(ka)}\right],$$
$$\alpha_z = -\frac{1}{4\pi}\left[1 - \frac{2}{ka}\frac{J_1(ka)}{J_0(ka)}\right],$$

with $k = (1+i)/\delta$. We will mainly need the imaginary part in the limit where $\delta \gg a$, which is

$$\operatorname{Im}\alpha_x = \operatorname{Im}\alpha_y = \frac{a^2}{8\pi\delta^2}$$
$$\operatorname{Im}\alpha_z = \frac{a^2}{16\pi\delta^2}.$$

According to the usual prescription, we find

$$\langle B_z(\vec{r})\, B_z(\vec{r})\rangle = \frac{27\pi\hbar a^2}{256 d^5} \operatorname{Im}\left[\frac{2}{ka}\frac{J_1(ka)}{J_0(ka)}\right] \coth\left(\frac{\hbar\omega}{2k_B T}\right), \tag{99}$$

valid for any value of δ/a.

When $a \ll \delta$ we expand the Bessel functions for small argument and find

$$B_z^{(ind)} = \frac{\pi a^2 \alpha_z m}{d^5}\frac{27\pi}{128}$$
$$\langle B_z(\vec{r})\, B_z(\vec{r})\rangle = \frac{27\pi\hbar a^4}{2048 d^5\delta^2}\coth\left(\frac{\hbar\omega}{2k_B T}\right).$$

The same computation can be performed for the x and y directions. The results for $i = j = x$ are

$$\langle B_x(\vec{r})\, B_x(\vec{r})\rangle = \frac{123\pi\hbar a^2}{256 d^5}\,\mathrm{Im}\left[\frac{2}{ka}\frac{J_1(ka)}{J_0(ka)}\right]\coth\left(\frac{\hbar\omega}{2k_BT}\right), \tag{100}$$

valid for any value of δ/a and for $a \ll \delta$ we have

$$\langle B_x(\vec{r})\, B_x(\vec{r})\rangle = \frac{123\pi\hbar a^4}{1024\; d^5\delta^2}\coth\left(\frac{\hbar\omega}{2k_BT}\right), \tag{101}$$

while for $i = j = y$

$$\langle B_y(\vec{r})\, B_y(\vec{r})\rangle = \frac{3\pi\hbar a^2}{32 d^5}\,\mathrm{Im}\left[\frac{2}{ka}\frac{J_1(ka)}{J_0(ka)}\right]\coth\left(\frac{\hbar\omega}{2k_BT}\right), \tag{102}$$

valid for any value of δ/a and for $a \gg \delta$

$$B_y^{(ind)} = \frac{\pi a^2\alpha_y m}{d^5}\frac{3\pi}{16}$$
$$\langle B_y(\vec{r})\, B_y(\vec{r})\rangle = \frac{3\pi\hbar a^4}{128 d^5\delta^2}\coth\left(\frac{\hbar\omega}{2k_BT}\right).$$

These considerations lead to very subtantial anisotropy in the correlation functions and in the relaxation times. We have that for $d \gg a$

$$\langle B_x(\vec{r})\, B_x(\vec{r})\rangle : \langle B_y(\vec{r})\, B_y(\vec{r})\rangle : \langle B_z(\vec{r}\,')\, B_z(\vec{r})\rangle = 82 : 16 : 9. \tag{103}$$

The cylindrical geometry occurs when wires or antennas are close to the qubit. The anisotropy can serve as a signature of noise originating from such a structure. The pattern of the anisotropy with the z-z correlations exceeding the x-x correlations is not difficult to understand. The longer dimension corresponds naturally to greater polarizabilty and therefore to stronger noise.

Distant Object

We now treat the magnetic noise of a metallic object whose maximum linear dimension is short compared with the distance to the qubit: $d \gg L$. We consider a fictitious point magnetic dipole $\vec{m}$ at $\vec{r}\,'$ and a magnetically polarizable metallic object at the origin. The

observation point is $\vec{r}$. Since L is small, we may take the field $\vec{B}'$ at the object due to the test dipole to be uniform over the object. If we assume that the electrode is spherical and its dielectric function is isotropic then the magnetic polarizability can be written as $\beta_{jn}(\omega) = \delta_{jn}\beta(\omega)$ and Eq. (27) gives the physical correlation function:

$$\langle B_i(\vec{r})\, B_k(\vec{r}\,')\rangle = \hbar \coth\left(\frac{\hbar\omega}{2k_BT}\right) \operatorname{Im}\beta \frac{3x_j'x_k' - \delta_{jk}r'^2}{r'^5}\frac{3x_ix_j - \delta_{ij}r^2}{r^5}$$

This manifestly satisfies the Onsager relation

$$G_{ik}(\omega;\vec{r},\vec{r}\,') = G_{ki}(\omega;\vec{r}\,',\vec{r})\,. \tag{104}$$

The local noise at $\vec{r} = \vec{r}\,'$ is

$$\langle B_i(\vec{r})\, B_k(\vec{r}\,' = \vec{r})\rangle = \hbar \coth\left(\frac{\hbar\omega}{2k_BT}\right) \operatorname{Im}(\beta)\, \frac{3x_ix_k + \delta_{ik}r^2}{r^8}. \tag{105}$$

Thus the problem reduces to a calculation of $\operatorname{Im}[\beta(\omega)]$, the dissipative part of the polarizability of the electrode. For a spherical electrode with radius a and conductivity σ, we have that [44]

$$\operatorname{Im}\beta = -\frac{3\delta^2 a}{4}\left[1 - \frac{a\sinh(2a/\delta) + \sin(2a/\delta)}{\cosh(2a/\delta) - \cos(2a/\delta)}\right], \tag{106}$$

which reduces when $\delta \gg a$ to

$$\operatorname{Im}\beta = \frac{a^5}{15\delta^2} \tag{107}$$

and when $\delta \ll a$ to

$$\operatorname{Im}\beta = \frac{3a^2\delta}{4}. \tag{108}$$

Notice that the *anisotropy* in lifetimes of a qubit in the presence of a spherical electrode is independent of β. If the qubit is located at $\vec{r} = r\hat{z}$, then

$$\langle B_x(\vec{r})\, B_x(\vec{r}\,' = \vec{r})\rangle = \langle B_y(\vec{r})\, B_y(\vec{r}\,' = \vec{r})\rangle = \hbar \coth\left(\frac{\hbar\omega}{2k_BT}\right) \frac{\operatorname{Im}[\beta(\omega)]}{r^6} \tag{109}$$

$$\langle B_z(\vec{r})\, B_z(\vec{r}\,' = \vec{r})\rangle = 4\hbar \coth\left(\frac{\hbar\omega}{2k_BT}\right)\frac{\mathrm{Im}\left[\beta(\omega)\right]}{r^6}. \tag{110}$$

The r^{-6} dependence is familiar from the van der Waals force, which has a similar physical origin. The anisotropy

$$\langle B_z(\vec{r})\, B_z(\vec{r})\rangle = 4\langle B_x(\vec{r})\, B_x(\vec{r})\rangle \tag{111}$$

is stronger than in the half-space case.

0.6 Comparison With Experiment

In this section we provide some numerical estimates for the noise strength and the resulting qubit relaxation times, which will allow us to evaluate the relevance of EWJN for current experiments. We shall focus on the half-space geometry, since this case is the important one for existing devices; the greatest masses of metal in semicoductor qubit systems are usually in global gates.

Charge Qubits

The noise spectral energy density is of some interest. Taking $\omega = 10^9/s$, $\sigma = 10^{17}/s$, we get $\delta = c/\sqrt{2\pi\sigma\omega} = 12\times10^{-4}$ cm $= 12\ \mu$ and we will only consider the regime $d \ll \delta$. The vacuum wavelength $\lambda = 60$ cm is the longest length in the problem and plays no role in our quasistatic regime. At a distance d from a half space we find and $T = 1$K and $\varepsilon_d = 10$ we have:

$$\langle E_x(d)\, E_x(d)\rangle_\omega \approx \frac{k_BT}{8\pi\sigma d^3} = 9\times10^{-22}\frac{erg}{cm^3}s. \tag{112}$$

This noise will relax qubits. In Fig. 7 we give numerical estimates for T_1 of a charge qubit in a half-space geometry. The curves are plotted using Eqs. (36) and (53) assuming a point qubit. Each curve represents $T_1(d)$ for various values of the distance d from the half space and the dot separation L, the latter being listed in the inset. We have assumed $\omega = 10^9$ s^{-1}, $\sigma = 10^{16}$ s^{-1}, $T = 0.1$ K. Indicated on the figure are experimental values for T_1 and the predictions our model makes based on estimates of the particular experiment's

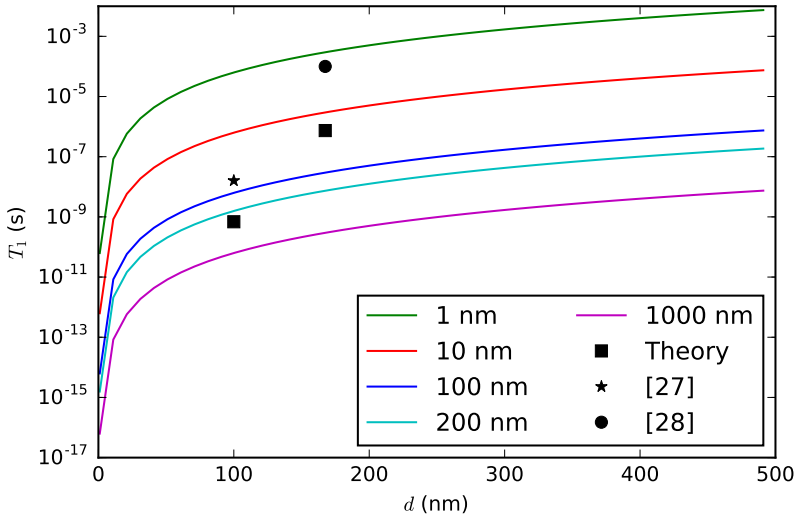

Figure 7: The charge qubit relaxation time T_1 as a function of the distance d from the qubit to a planar metal gate for various values of the dot separation, as listed in the inset. The experimental data are taken from Ref. [34, 35]. The theoretical predictions are indicated by solid squares. The qubit operating frequency is taken as $\omega = 10^9$ s^{-1}, while the conductivities are roughly estimated as $\sigma = 10^{16}$ s^{-1}. The temperature is $T = 0.1$ K.

qubit and surrounding geometry. The measured values are an order of magnitude or two smaller than the predictions made by our model, indicating that EWJN is probably not the dominant mechanism behind qubit relaxation in these experiments. However, the estimates here are made with very limited knowledge of the particular experimental values of d and L, which are normally not very accurately determined. Since $T_1 \propto d^3/L^2$ a factor of 2 could account for an order of magnitude correction. A further serious source of uncertainty is that σ is not measured and generally is poorly known. If σ is too large, the mean free path is the electrons in the metal may become comparable to the gate dimensions, invalidating the local electrodynamics used in this thesis. These considerations taken together mean that it is difficult to give a clear evaluation of the role of EWJN in charge qubit experiments. In any case, it seems safe to say that even rather minor improvements in other decoherence mechanisms would make the EWJN mechanism competitive with the others.

Spin qubits

We can now repeat the numerical estimates for the noise strength and the resulting qubit relaxation times for magnetic noise and spin qubits.

The noise energy density is again of some interest. With $\omega = 10^9/s$, $\sigma = 10^{17}/s$, $T = 1$ K, $d = 50$ nm from a half space we have:

$$\langle B_z B_z \rangle_\omega \approx \frac{\pi k_B T \sigma}{dc^2} = 3.0 \times 10^{-15} \frac{erg\dot{s}}{cm^3} \tag{113}$$

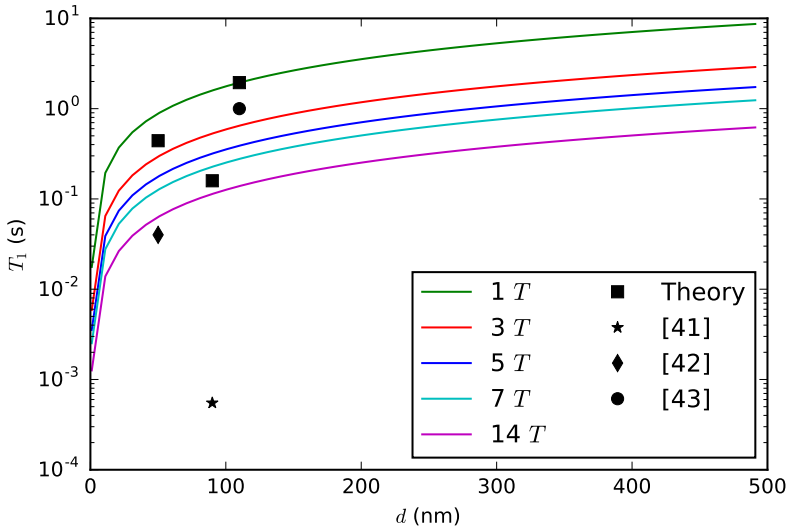

Figure 8: The spin qubit relaxation time T_1 as a function of the distance d from the qubit to a planar metal gate for various values of the external magnetic field, as listed in the inset. The experimental data are taken from Ref. [48, 49, 50]. The theoretical predictions are indicated by solid squares. The conductivities are roughly estimated as $\sigma = 10^{16}$ s^{-1}. The temperature is $T = 0.1$ K.

This noise will relax qubits. In Fig. 8 we give numerical estimates for T_1 of a spin qubit in a half-space geometry. The curves are plotted using Eq. (36) assuming a point qubit. Each curve represents $T_1(d)$ for various values of the distance d from the half space for a fixed B field, which enters T_1 via $\hbar\omega = g\mu B$ with $g = 2$. We have assumed $\sigma = 10^{16}$ s^{-1}, $T = 0.1$ K. Indicated on the figure are experimental values for T_1 and the predictions our model makes based on estimates of the particular experiment's qubit and surrounding geometry. The

geometries are somewhat better determined in these experiments, meaning that that the main source of uncertainty is in the conductivity σ, which may differ from our assumption by an order of magnitude.

The experimental values shown in Fig. 7 are in small devices characterized by linear dimensions of order 100 nm, but we note that in certain MOS devices the relevant distances can be closer to 10 nm [51, 52]. Other qubit architectures such as atom traps, ion traps, or superconductors, are generally considerably larger. This makes it unlikely that EWJN plays a large role in the decoherence of these devices, since the power-law falloffs reduce the noise strength at the qubit positions. This could change as these devices are miniaturized [53, 54].

0.7 Multipole moments in T_1 and T_2

The expressions in Eqs. (36) and (44) can be generalized to higher order multipole moments by keeping more terms in the Taylor expansion of the electromagnetic potentials. Define the electric moments $q_i = er_i$, $q_{ij} = er_ir_j$ and magnetic dipole $m_i = \frac{e}{2mc}((\vec{r} \times \vec{\Pi})_i + gS_i)$. We then have

$$[H_q, p_i] = -\frac{i\hbar e}{m}\Pi_i$$
$$[H_q, q_{ij}] = -\frac{i\hbar q}{m}\left(r_i\Pi_j + r_j\Pi_i - i\hbar\delta_{ij}\right).$$

We can find the quadrupole contribution by expanding Eq. (34) and keeping track of all first derivative terms giving us

$$\begin{aligned}
\langle 0|H_n(t)|1\rangle &= -\frac{e}{mc}\left[A_i(0,t)\,\langle 0|\Pi_i|1\rangle\right. \\
&\quad \left. +\,\langle 0|\left(\nabla_j A_i(r,t)\right)_{r=0} r_j\Pi_i|1\rangle\right] - \frac{eg}{2mc}B_i\,\langle 0|S_i|1\rangle \\
&= i\frac{\omega}{c}\,\langle 0|p_i|1\rangle\,A_i(0,t) - \frac{e}{mc}\langle 0|\frac{1}{2}[\nabla_j A_i]_{r=0}(r_i\Pi_j + r_j\Pi_i)|1\rangle \\
&\quad - \frac{e}{2mc}(\nabla\times\vec{A})_{k,r=0}\langle 0|\epsilon_{ijk}r_j\Pi_i|1\rangle - \frac{eg}{2mc}B_i\,\langle 0|S_i|1\rangle \\
&= i\frac{\omega}{c}\left(\langle 0|p_i|1\rangle\,A_i(0,t) + \frac{1}{2}[\nabla_j A_i]_{r=0}\,\langle 0|q_{ij}|1\rangle\right) \\
&\quad - B_k(0,t)\,\langle 0|m_k|1\rangle\,.
\end{aligned}$$

We have employed the vector identity

$$\begin{aligned}
[\nabla_j A_i(r,t)]_{r=0}\,r_j\Pi_i &= \frac{1}{2}[\nabla_j A_i]_{r=0}(r_i\Pi_j + r_j\Pi_i) \\
&\quad - \frac{1}{2}\epsilon_{ijk}(\nabla\times\vec{A})_{k,r=0}r_j\Pi_i.
\end{aligned}$$

Now we can work out an expression for T_1 using Eq. (30)

$$\begin{aligned}
\frac{1}{T_1} = \frac{1}{\hbar^2}\Big[&\langle p_i\rangle\,\langle p_l\rangle^*\,\langle E_iE_l\rangle_\omega + \frac{1}{2}\,\langle p_i\rangle\,\langle q_{lm}\rangle^*\,\langle E_i\nabla_m E_l\rangle_\omega + \frac{1}{2}\,\langle q_{ij}\rangle\,\langle p_l\rangle^*\,\langle\nabla_j E_iE_l\rangle_\omega \\
&+ \langle p_i\rangle\,\langle m_n\rangle^*\,\langle E_iB_n\rangle_\omega + \langle m_k\rangle\,\langle p_l\rangle^*\,\langle B_kE_l\rangle_\omega + \langle m_k\rangle\,\langle m_n\rangle^*\,\langle B_kB_n\rangle_\omega \\
&- \frac{1}{2}\,\langle q_{ij}\rangle\,\langle m_n\rangle^*\,\langle\nabla_j E_iB_n\rangle_\omega + \frac{1}{2}\,\langle m_k\rangle\,\langle q_{lm}\rangle^*\,\langle B_k\nabla_m E_l\rangle_\omega + \frac{1}{4}\,\langle q_{ij}\rangle\,\langle q_{lm}\rangle^*\,\langle\nabla_j E_i\nabla_m E_l\rangle\Big]\,.
\end{aligned}$$

A naive application of the analysis from the preceeding calculation would indicate that E-field noise will not contribute to diagonal elements of $H_n(t)$, but this is due to the incomplete application of the gauge condition $\phi = 0$. If we begin with the gauge-invariant Schrö dinger equation with an arbitrary scalar potential $\phi(r,t)$ and vector potential obeying $\nabla\cdot\vec{A} = 0$ and eliminate the residual gauge freedom via $\vec{A}\,'(r,t) = \vec{A}(r,t) + \nabla\alpha(r,t)$, $\phi\,'(r,t) = \phi(r,t) -$

$\dot{\alpha}(r,t) = 0$ and $\psi\,' = e^{-ie\alpha/\hbar}\psi(r,t)$ we find that the wave function obeys

$$i\hbar\dot{\psi} = \left(e^{ie\alpha/\hbar}H\,'^{-ie\alpha/\hbar} - e\dot{\alpha}\right)\psi. \tag{114}$$

The Hamiltonian H' in the gauge with no scalar potential is complemented by the gauge fixing term that retains the electric field contribution in the equations of motion. The operator we need in Eq. (43) can be expanded in Taylor series as

$$\begin{aligned} H_n(t) = &-\frac{e}{mc}\left(A_i(0,t) + \left[\nabla_j A_i(r,t)\right]_{r=0} r_j + \dots\right)\Pi_i \\ &- \frac{eg}{2mc}B_i S_i. - e\left(\dot{\alpha}(0,t) + \nabla_j\dot{\alpha}(0,t)r_j + \dots\right). \end{aligned} \tag{115}$$

Now turning to the relevant matrix elements of Eq. (34) with the gauge term (equivalently, the scalar potential), we begin by treating the vector potential terms

$$\begin{aligned} -\frac{e}{mc}\langle 1|A_i(0,t)\Pi_i|1\rangle &= \frac{i}{\hbar c}A_i(0,t)\left(\langle 1|p_i H_q|1\rangle - \langle 1|H_q p_i|1\rangle\right) \\ &= \frac{i}{\hbar c}A_i(\epsilon_1-\epsilon_1)\langle 1|p_i|1\rangle = 0, \\ -\frac{e}{mc}\langle 1|\nabla_j A_i r_j\Pi_i|1\rangle &= -\frac{e}{mc}\left[\frac{1}{2}\nabla_j A_i\langle 1|r_i\Pi_j + r_j\Pi_i|1\rangle\right. \\ &\qquad \left. + \frac{1}{2}B_k\langle 1|l_k|1\rangle\right] \\ &= -\frac{e}{mc}\left(\frac{i\hbar}{2}\nabla_j A_i\delta_{ij}\right) - \frac{e}{2mc}B_k\langle 1|l_k|1\rangle \\ &= -\frac{e}{2mc}B_k\langle 1|l_k|1\rangle. \end{aligned}$$

The last equality follows from $\nabla\cdot\vec{A} = 0$. We have $E_i(r,t) = -\nabla_i\dot{\alpha}(r,t)$. Using the same methods we obtain an expression for the integral kernel $S(\omega)$ for T_2 to quadrupole order.

$$\begin{aligned} S(\omega) = \frac{1}{\hbar^2}\Big[&\langle B_i(t)B_j(0)\rangle_\omega \Delta m_i\Delta m_j - \langle B_i(t)E_j(0)\rangle_\omega \Delta m_i\Delta p_j - \langle E_i(t)B_j(0)\rangle_\omega \Delta p_i\Delta m_j \\ &+ \langle E_i(t)E_j(0)\rangle_\omega \Delta p_i\Delta p_j + \frac{1}{2}\left(\langle\nabla_i E_j(t)B_k(0)\rangle_\omega \Delta q_{ij}\Delta m_k + \langle\nabla_i E_j(t)E_k(0)\rangle_\omega \Delta q_{ij}\Delta p_k\right. \\ &\left. + \langle B_i(t)\nabla_j E_k(0)\rangle \Delta m_i\Delta q_{jk} + \langle E_i(t)\nabla_j E_k(0)\rangle_\omega \Delta p_i\Delta q_{jk}\right) \frac{1}{4}\langle\nabla_i E_j(t)\nabla_k E_l(0)\rangle_\omega \Delta q_{ij}\Delta q_{kl}\Big] \end{aligned}$$

0.8 Spectral Density Tensors

Here we include the details and off-diagonal components of the noise spectral density tensor for the simple geometries treated in the main body of the chapter.

Electric Noise

Place a fictitious electric dipole moment $\vec{p}$ at the point $\vec{r}\,' = (0,0,d)$ in the half-space geometry. The electric field in free space would be

$$E_j^{(ed)}(\vec{r}) = -\frac{\partial}{\partial x_j}\vec{p}\cdot\nabla\frac{1}{|\vec{r}-\vec{r}\,'|} = -p_k\frac{\partial}{\partial x_j}\frac{\partial}{\partial x_k}\frac{1}{|\vec{r}-\vec{r}\,'|}, \tag{116}$$

which satisfies $\nabla\cdot\vec{E}^{(ed)} = 4\pi\rho$ with $\rho = -\vec{p}\cdot\nabla\delta^3(\vec{r}-\vec{r}_0)$.

We will represent this fictitious field by using the identity

$$\frac{1}{|\vec{r}-\vec{r}\,'|} = \frac{1}{2\pi}\int\frac{d^2q}{q}\; e^{i\vec{q}\cdot\vec{\rho}}e^{-q|z-d|}, \tag{117}$$

where $\vec{q} = (q_x, q_y)$ and $\vec{\rho} = (x,y)$. Thus

$$E_j^{(ed)}(\vec{r}) = -\frac{p_k}{2\pi}\int\frac{d^2q}{q}\frac{\partial}{\partial x_j}\frac{\partial}{\partial x_k}\; e^{i\vec{q}\cdot\vec{\rho}}e^{-q|z-d|}. \tag{118}$$

The induced field for $z>0$ is expanded as

$$E_j^{(ind)}(\vec{r}) = -\frac{p}{2\pi}\int d^2q\; f_j(\vec{q})\, e^{i\vec{q}\cdot\vec{\rho}}e^{-qz}, \tag{119}$$

and the Maxwell equations imply

$$\nabla^2\vec{E}^{(ind)} = 0,\;\; \nabla\cdot\vec{E}^{(ind)} = 0,\;\; z>0, \tag{120}$$

so

$$q = \sqrt{q_x^2 + q_y^2}$$
$$iq_x f_x + iq_y f_y = q f_z.$$

The induced field for $z < 0$ is defined by

$$E_j^{(ind)}(\vec{r}) = -\frac{p}{2\pi} \int d^2q \; g_j(\vec{q})\, e^{i\vec{q}\cdot\vec{\rho}} e^{\alpha z} \tag{121}$$

and we have

$$\nabla^2 \vec{E}^{(ind)} + 2i\delta^{-2}\vec{E}^{(ind)} = 0, \; \nabla \cdot \vec{E}^{(ind)} = 0, \; z < 0 \tag{122}$$

and $\operatorname{Re}\alpha > 0$ and so

$$\alpha^2 = q_x^2 + q_y^2 - 2i\delta^{-2} = q^2 - 2i\delta^{-2}$$
$$iq_x g_x + iq_y g_y = -\alpha g_z.$$

The tangential component of $\vec{E}$ is continuous but the normal component satisfies $\vec{E}_{norm,out} = \varepsilon \vec{E}_{norm,in} \approx (4\pi i\sigma/\omega)\, \vec{E}_{norm,in}$, so $\left|\vec{E}_{norm,out}\right| \gg \left|\vec{E}_{norm,in}\right|$. $\vec{B}$ is continuous. The fictitious dipole $\vec{p} = p\hat{z}$ produces a field for $0 < z < d$

$$E_x^{(ed)}(\vec{r}) = -\frac{p}{2\pi} \int d^2q \; iq_x \; e^{i\vec{q}\cdot\vec{\rho}} e^{q(z-d)}$$
$$E_y^{(ed)}(\vec{r}) = -\frac{p}{2\pi} \int d^2q \; iq_y \; e^{i\vec{q}\cdot\vec{\rho}} e^{q(z-d)}$$
$$E_z^{(ed)}(\vec{r}) = -\frac{p}{2\pi} \int d^2q \; q \; e^{i\vec{q}\cdot\vec{\rho}} e^{q(z-d)},$$

and the induced field is defined by

$$\vec{E}^{(ind)} = -\frac{p}{2\pi} \int d^2q \; \vec{f}(\vec{q})\, e^{i\vec{q}\cdot\vec{\rho} - qz} \text{ for } z > 0 \text{ and}$$
$$\vec{E}^{(ind)} = -\frac{p}{2\pi} \int d^2q \; \vec{g}(\vec{q})\, e^{i\vec{q}\cdot\vec{\rho} + \alpha z} \text{ for } z < 0.$$

The boundary conditions yield

$$\begin{aligned} iq_x e^{-qd} + f_x &= g_x \\ iq_y e^{-qd} + f_y &= g_y \\ qe^{-qd} + f_z &= (\varepsilon_m/\varepsilon_d)\, g_z \\ iq_x f_x + iq_y f_y &= q f_z \\ iq_x g_x + iq_y g_y &= -\alpha g_z. \end{aligned}$$

The solution is

$$(f_x, f_y, f_z) = (-iq_x, -iq_y, q)\, e^{-qd} \frac{1 - (\varepsilon_m/\varepsilon_d)\, q/\alpha}{1 + (\varepsilon_m/\varepsilon_d)\, q/\alpha}, \tag{123}$$

which gives us an integral expression for the induced field and thus 61. For $\vec{p} = p\hat{x}$ the dipole produces a field for $0 < z < d$

$$\begin{aligned} E_x^{(ed)}(\vec{r}) &= \frac{p}{2\pi} \int \frac{d^2q\ q_x^2}{q}\ e^{i\vec{q}\cdot\vec{\rho}} e^{q(z-d)} \\ E_y^{(ed)}(\vec{r}) &= \frac{p}{2\pi} \int \frac{d^2q\ q_x q_y}{q}\ e^{i\vec{q}\cdot\vec{\rho}} e^{q(z-d)} \\ E_z^{(ed)}(\vec{r}) &= -\frac{ip}{2\pi} \int \frac{d^2q\ q_x q}{q}\ e^{i\vec{q}\cdot\vec{\rho}} e^{q(z-d)}. \end{aligned}$$

For $d \ll \delta$ we find

$$\begin{aligned} \operatorname{Im} \vec{E}^{(ind)}(\vec{r}) &= -\frac{p}{2\pi} \frac{\omega\varepsilon_d}{2\pi\sigma} \frac{\partial}{\partial x} \nabla \int d^2q\ \frac{1}{q} e^{-q(d+z)} e^{iq_x x + iq_y y} \\ &= -\frac{p}{2\pi} \frac{\omega\varepsilon_d}{\sigma} \frac{\partial}{\partial x} \nabla \frac{1}{\left[(z+d)^2 + \rho^2\right]^{1/2}} \\ &= \frac{p}{2\pi} \frac{\omega\varepsilon_d}{\sigma} \nabla \frac{x}{\left[(z+d)^2 + \rho^2\right]^{3/2}}. \end{aligned}$$

So, for example,

$$\operatorname{Im} E_x^{(ind)}(\vec{r}) = -\frac{p}{2\pi} \frac{\omega\varepsilon_d}{\sigma} \frac{2x^2 - (z+d)^2 - y^2}{\left[(z+d)^2 + \rho^2\right]^{5/2}}. \tag{124}$$

In the regime $d \gg \delta$ we find

$$\begin{aligned}\operatorname{Im} \vec{E}^{(ind)}(\vec{r}) &= -\frac{p}{2\pi}\frac{\omega\varepsilon_d}{2\pi\sigma\delta}\frac{\partial}{\partial x}\nabla \int d^2q\ \frac{1}{q^2} e^{-q(d+z)} e^{iq_x x + iq_y y} \\ &= \frac{p}{2\pi}\frac{\omega\varepsilon_d}{\sigma\delta}\nabla\left\{\frac{x}{\rho^2}\left[1 - \frac{d+z}{\left[(z+d)^2+\rho^2\right]^{1/2}}\right]\right\},\end{aligned}$$

which gives us the correlation functions presented in the main text.

For $\vec{p} = p\hat{z}$, $\vec{r}\,' = (0,0,d)$ and $d \ll \delta$ the matrix elements are:

$$\left\langle E_z(\vec{r})\, E_z(\vec{r}\,')\right\rangle_\omega = \frac{\hbar\omega\varepsilon_d}{2\pi\sigma}\frac{2(d+z)^2-\rho^2}{\left[(d+z)^2+\rho^2\right]^{5/2}}\coth\frac{\hbar\omega}{2k_BT}, \tag{125}$$

$$\left\langle E_x(\vec{r})\, E_z(\vec{r}\,')\right\rangle_\omega = \frac{3\hbar\omega\varepsilon_d}{2\pi\sigma}\frac{x(d+z)}{\left[(d+z)^2+\rho^2\right]^{5/2}}\coth\frac{\hbar\omega}{2k_BT}, \tag{126}$$

$$\left\langle E_y(\vec{r})\, E_z(\vec{r}\,')\right\rangle_\omega = \frac{3\hbar\omega\varepsilon_d}{2\pi\sigma}\frac{y(d+z)}{\left[(d+z)^2+\rho^2\right]^{5/2}}\coth\frac{\hbar\omega}{2k_BT}. \tag{127}$$

When $d \gg \delta$ we have

$$\left\langle E_z(\vec{r})\, E_z(\vec{r}\,')\right\rangle_\omega = \frac{\hbar\omega\varepsilon_d}{2\pi\sigma\delta}\frac{d+z}{\left[(d+z)^2+\rho^2\right]^{3/2}}\coth\frac{\hbar\omega}{2k_BT}, \tag{128}$$

$$\left\langle E_x(\vec{r})\, E_z(\vec{r}\,')\right\rangle_\omega = \frac{\hbar\omega\varepsilon_d}{2\pi\sigma\delta}\frac{x}{\left[(d+z)^2+\rho^2\right]^{3/2}}\coth\frac{\hbar\omega}{2k_BT}, \tag{129}$$

$$\left\langle E_y(\vec{r})\, E_z(\vec{r}\,')\right\rangle_\omega = \frac{\hbar\omega\varepsilon_d}{2\pi\sigma\delta}\frac{y}{\left[(d+z)^2+\rho^2\right]^{3/2}}\coth\frac{\hbar\omega}{2k_BT}. \tag{130}$$

Now we turn to the solution for $\vec{p} = p\hat{x}$ and $d \ll \delta$. The matrix elements are

$$\left\langle E_x(\vec{r})\, E_x(\vec{r}\,')\right\rangle_\omega = -\frac{\hbar}{2\pi}\frac{\omega\varepsilon_d}{\sigma}\frac{2x^2-(z+d)^2-y^2}{\left[(z+d)^2+\rho^2\right]^{5/2}}\coth\frac{\hbar\omega}{2k_BT}, \tag{131}$$

$$\left\langle E_y(\vec{r})\, E_x(\vec{r}\,')\right\rangle_\omega = \frac{3\hbar\omega\varepsilon_d}{2\pi\sigma}\frac{xy}{\left[(z+d)^2+\rho^2\right]^{5/2}}\coth\frac{\hbar\omega}{2k_BT} \tag{132}$$

$$\left\langle E_z(\vec{r})\, E_x(\vec{r}\,')\right\rangle_\omega = -\frac{3\hbar\omega\varepsilon_d}{2\pi\sigma}\frac{x(d+z)}{\left[(z+d)^2+\rho^2\right]^{5/2}}\coth\frac{\hbar\omega}{2k_BT}, \tag{133}$$

and comparison with Eq. (126) shows that the Onsager relation is satisfied.

The components when $d \gg \delta$ are:

$$\left\langle E_x\left(\vec{r}\right) E_x\left(\vec{r}\,'\right)\right\rangle_\omega = \frac{\hbar}{2\pi}\frac{\omega\varepsilon_d}{\sigma\delta}\coth\frac{\hbar\omega}{2k_BT}\times \left\{\frac{y^2-x^2}{\rho^4}\left[1-\frac{d+z}{\left[(z+d)^2+\rho^2\right]^{1/2}}\right]+\frac{x^2\left(d+z\right)}{\rho^2\left[(z+d)^2+\rho^2\right]^{3/2}}\right\} \tag{134}$$

$$\left\langle E_y\left(\vec{r}\right) E_x\left(\vec{r}\,'\right)\right\rangle_\omega = -\frac{\hbar}{2\pi}\frac{\omega\varepsilon_d}{\sigma\delta}\coth\frac{\hbar\omega}{2k_BT}\times \frac{xy}{\rho^2}\left\{\frac{2}{\rho^2}\left[1-\frac{d+z}{\left[(z+d)^2+\rho^2\right]^{1/2}}\right]-\frac{d+z}{\left[(z+d)^2+\rho^2\right]^{3/2}}\right\}. \tag{135}$$

$$\left\langle E_z\left(\vec{r}\right) E_x\left(\vec{r}\,'\right)\right\rangle_\omega = -\frac{\hbar}{2\pi}\frac{\omega\varepsilon_d}{\sigma\delta}\frac{x}{\left[(z+d)^2+\rho^2\right]^{3/2}}\coth\frac{\hbar\omega}{2k_BT}, \tag{136}$$

and comparison with Eq. (129) shows that the Onsager relation is satisfied.

For the distant object geometry Since L, the qubit size, is small, we may take the field $\vec{E}\,'$ at the electrode due to the test dipole to be uniform over the object. It is given by

$$\begin{aligned} E_j'\left(\vec{r}=0\right) &= p_k\ \partial_j\partial_k\frac{1}{|\vec{r}\,'|} \\ &= p_k\frac{3x_j'x_k'-\delta_{jk}r'^2}{r'^5} = p_k f_{jk}(\vec{r}), \end{aligned}$$

where we have defined the dipole function

$$f_{ij}\left(\vec{r}\right) \equiv \frac{3x_ix_j-\delta_{ij}r^2}{r^5}. \tag{137}$$

We shall take only the first term in the multipole expansion of the field produced by the object. We will write this dipole as $\vec{p}^{(el)}$ ("el" for "electrode".) It can be written as

$p_j^{(el)}(\omega) = \alpha_{jn}(\omega) E_n'(\omega)$. At the observation point $\vec{r}$ the (again fictitious) field is

$$\begin{aligned} E_i(\vec{r}) &= p_j^{(el)} \partial_i \partial_j \frac{1}{|\vec{r}|} \\ &= \alpha_{jn} E_n' f_{ij}(\vec{r}) \\ &= \alpha_{jn} p_m' f_{mn}(\vec{r}\,') f_{ij}(\vec{r}), \end{aligned}$$

This leads directly to

$$\langle E_i(\vec{r}) E_k(\vec{r}\,') \rangle = \hbar \coth\left(\frac{\hbar\omega}{2k_B T}\right) \mathrm{Im}(\alpha_{jn}) f_{kn}(\vec{r}\,') f_{ij}(\vec{r}). \tag{138}$$

Hence only the polarizability of the object is relevant in the problem. If we assume that the electrode is spherical and its dielectric function is isotropic then $p_j^{(sph)}(\omega) = \alpha(\omega)\delta_{jn} E_n'(\omega)$ and

$$\begin{aligned} E_i^{(sp)}(\vec{r}) &= \alpha(\omega) p_k' f_{jk}(\vec{r}\,') f_{ij}(\vec{r}) \\ &= \alpha(\omega) p_k' \frac{9x_i x_k' \, \vec{r}\cdot\vec{r}\,' + \delta_{ik} r^2 r'^2 - 3x_i x_k r'^2 - 3x_i' x_k' r^2}{r^5 r'^5}. \end{aligned}$$

Using Eq. (22), we have

$$-\frac{\omega^2}{\hbar c^2} G_{ik}(\omega; \vec{r}, \vec{r}\,') = \alpha(\omega) f_{ij}(\vec{r}) f_{jk}(\vec{r}\,'). \tag{139}$$

This manifestly satisfies the Onsager relation

$$G_{ik}(\omega; \vec{r}, \vec{r}\,') = G_{ki}(\omega; \vec{r}\,', \vec{r}). \tag{140}$$

And we find

$$\langle E_i(\vec{r}) E_k(\vec{r}\,') \rangle = \hbar \coth\left(\frac{\hbar\omega}{2k_B T}\right) \mathrm{Im}[\alpha(\omega)] f_{kj}(\vec{r}\,') f_{ij}(\vec{r}). \tag{141}$$

Magnetic Noise

To find the noise tensor in the half space we place a magnetic dipole moment $\vec{m} = m\hat{z}$ at $\vec{r} = (0, 0, d)$ in analogy to the electric field noise calculation. The magnetic field due to this fictitious dipole in free space would be

$$B_j^{(md)}(\vec{r}) = m_i \frac{\partial}{\partial x_i} \frac{\partial}{\partial x_j} \frac{1}{|\vec{r} - \vec{r}\,'|}, \tag{142}$$

which satisfies $\nabla \times \vec{B}^{(md)} = 4\pi \vec{J}/c$ and $\vec{J} = \vec{m} \times \nabla \delta^3(\vec{r} - \vec{r}\,')$. Proceeding analogously to Eq. (116), we have

$$B_j^{(md)}(\vec{r}) = \frac{m_k}{2\pi} \int \frac{d^2q}{q} \frac{\partial}{\partial x_j} \frac{\partial}{\partial x_k}\, e^{i\vec{q}\cdot\vec{\rho}} e^{-q|z-d|}. \tag{143}$$

where $\vec{q} = (q_x, q_y)$ and $\vec{\rho} = (x, y)$, and

$$\vec{B}^{(ind)}(\vec{r}) = -\frac{m}{2\pi} \int d^2q\ \ (-iq_x, -iq_y, q)\, e^{-qd} \frac{1 - q/\alpha}{1 + q/\alpha} e^{iq_x x + iq_y y - qz} \quad \text{for } z > 0. \tag{144}$$

For $d \ll \delta$ we find

$$\begin{aligned} \frac{1 - q/\alpha}{1 + q/\alpha} &= \frac{\sqrt{q^2 - 2i\delta^{-2}} - q}{\sqrt{q^2 - 2i\delta^{-2}} + q} \\ &\approx \left(-\frac{i}{2q^2\delta^2} \right) \end{aligned}$$

and

$$\vec{B}^{(ind)}(\vec{r}) = \frac{im}{4\pi\delta^2} \int d^2q \frac{1}{q^2}\ \ (-iq_x, -iq_y, q)\, e^{-q(z+d)} e^{iq_x x + iq_y y} \quad \text{for } z > 0 \tag{145}$$

For $\vec{m} = m\hat{z}$ and $d \ll \delta$ the components of the noise tensor in the half space are:

$$\langle B_z(\vec{r})\, B_z(\vec{r}\,')\rangle_\omega = \frac{\hbar}{2\delta^2} \frac{1}{\left[(d+z)^2 + \rho^2\right]^{1/2}} \coth \frac{\hbar\omega}{2k_B T}, \tag{146}$$

$$\langle B_x(\vec{r})\, B_z(\vec{r}\,')\rangle_\omega = \frac{\hbar}{2\delta^2} \frac{x}{\rho^2} \left\{ 1 - \frac{(d+z)}{\left[(d+z)^2 + \rho^2\right]^{1/2}} \right\} \coth \frac{\hbar\omega}{2k_B T} \tag{147}$$

$$\left\langle B_y\left(\vec{r}\right)B_z\left(\vec{r}\,'\right)\right\rangle_\omega = \frac{\hbar}{2\delta^2}\frac{y}{\rho^2}\left\{1-\frac{(d+z)}{\left[(d+z)^2+\rho^2\right]^{1/2}}\right\}\coth\frac{\hbar\omega}{2k_BT}. \tag{148}$$

In the regime where $d \gg \delta$ we have

$$\left\langle B_z\left(\vec{r}\right)B_z\left(\vec{r}\,'\right)\right\rangle_\omega = -\hbar\delta\coth\frac{\hbar\omega}{2k_BT}\times\left[\frac{-6\left(z+d\right)^3+9\rho^2\left(z+d\right)}{\left[(d+z)^2+\rho^2\right]^{7/2}}\right], \tag{149}$$

$$\left\langle B_x\left(\vec{r}\right)B_z\left(\vec{r}\,'\right)\right\rangle_\omega = -\hbar\delta\coth\frac{\hbar\omega}{2k_BT}\times\left[\frac{-12x\left(z+d\right)^2+3x\rho^2}{\left[(d+z)^2+\rho^2\right]^{7/2}}\right] \tag{150}$$

$$\left\langle B_y\left(\vec{r}\right)B_z\left(\vec{r}\,'\right)\right\rangle_\omega = -\hbar\delta\coth\frac{\hbar\omega}{2k_BT}\times\left[\frac{-12y\left(z+d\right)^2+3y\rho^2}{\left[(d+z)^2+\rho^2\right]^{7/2}}\right]. \tag{151}$$

Now we turn to $\vec{m} = m\hat{x}$ and $d \ll \delta$ where the components are

$$\left\langle B_x\left(\vec{r}\right)B_x\left(\vec{r}\,'\right)\right\rangle_\omega = \frac{\hbar}{2\delta^2}\coth\frac{\hbar\omega}{2k_BT}\left[\frac{x^2-y^2}{\rho^2}\left\{\left[(d+z)^2+\rho^2\right]^{1/2}-(d+z)\right\}-\frac{x^2}{\rho^2\left[(d+z)^2+\rho^2\right]^{1/2}}\right].$$

$$\begin{aligned}\left\langle B_y\left(\vec{r}\right)B_x\left(\vec{r}\,'\right)\right\rangle_\omega &= \frac{\hbar}{2\delta^2}\coth\frac{\hbar\omega}{2k_BT}\frac{\partial}{\partial x}\left[\frac{y}{\rho}\int_0^\infty dq\ \frac{1}{q}e^{-q(z+d)}J_1\left(q\rho\right)\right] \\ &= \frac{\hbar}{2\pi}\coth\frac{\hbar\omega}{2k_BT}\frac{\partial}{\partial x}\left[\frac{y}{\rho^2}\left\{\left[(d+z)^2+\rho^2\right]^{1/2}-(d+z)\right\}\right] \\ &= -\frac{\hbar}{4\pi\delta^2}\coth\frac{\hbar\omega}{2k_BT}\left[\frac{-2xy}{\rho^4}\left\{\left[(d+z)^2+\rho^2\right]^{1/2}-(d+z)\right\}+\frac{xy}{\rho^2}\left[(d+z)^2+\rho^2\right]^{-1/2}\right]\end{aligned} \tag{152}$$

$$\begin{aligned}\left\langle B_z\left(\vec{r}\right)B_x\left(\vec{r}\,'\right)\right\rangle_\omega &= -\frac{\hbar}{2\delta^2}\coth\frac{\hbar\omega}{2k_BT}\frac{\partial}{\partial x}\frac{\partial}{\partial z}\int_0^\infty dq\ \frac{1}{q^2}e^{-q(z+d)}J_0\left(q\rho\right) \\ &= \frac{\hbar}{2\delta^2}\coth\frac{\hbar\omega}{2k_BT}\frac{\partial}{\partial x}\int_0^\infty dq\ \frac{1}{q}e^{-q(z+d)}J_0\left(q\rho\right) \\ &= -\frac{\hbar}{2\delta^2}\coth\frac{\hbar\omega}{2k_BT}\frac{x}{\rho^2}\left\{\left[(d+z)^2+\rho^2\right]^{1/2}-(d+z)\right\}.\end{aligned} \tag{153}$$

On the other hand when $d \gg \delta$ we find

$$\left\langle B_x\left(\vec{r}\right)B_x\left(\vec{r}\,'\right)\right\rangle_\omega = \hbar\delta\coth\frac{\hbar\omega}{2k_BT}\left(d+z\right)\frac{3\left(d+z\right)^2+3\rho^2-15x^2}{\left[(d+z)^2+\rho^2\right]^{7/2}} \tag{154}$$

$$\langle B_y(\vec{r})\, B_x(\vec{r}\,')\rangle_\omega = -15\hbar\delta \coth\frac{\hbar\omega}{2k_BT}\frac{xy\,(d+z)}{\left[(d+z)^2+\rho^2\right]^{7/2}} \tag{155}$$

$$\langle B_z(\vec{r})\, B_x(\vec{r}\,')\rangle_\omega = \hbar\delta \coth\frac{\hbar\omega}{2k_BT}\frac{-12x\,(d+z)^2+3x\rho^2}{\left[(d+z)^2+\rho^2\right]^{7/2}}. \tag{156}$$

The distant object geometry results can be obtained by placing a fictitious dipole near a magnetically polarizable electrode. Since $d \gg L$ we assume the field generated by this electrode is uniform over the qubit and given by

$$B_k'(0) = m_j\ f_{kj}(\vec{r}\,'), \tag{157}$$

where again $f_{jk}(\vec{r}) = (3r_ir_j - r^2\delta_{ij})/r^5$. We shall take only the first term in the multipole expansion of the field produced by the object, which is completely characterized by its dipole moment $\vec{m}\,'$. Assuming linear response yields $m_i' = \beta_{ij}B_j'$, where β_{ij} is the magnetic polarizability of the object. At the observation point $\vec{r}$ the (again fictitious) field is

$$\begin{aligned} B_i(\vec{r}) &= m_m' f_{im}(\vec{r}) \\ &= \beta_{mk} m_j\ f_{kj}(\vec{r}\,')\, f_{im}(\vec{r}), \end{aligned}$$

and the prescription following Eq. 26 then gives the physical noise function as

$$\langle B_i(\vec{r})\, B_j(\vec{r}\,')\rangle = \hbar\,\mathrm{Im}(\beta_{mk})\ f_{kj}(\vec{r}\,')\, f_{im}(\vec{r}) \coth(\hbar\omega/k_BT). \tag{158}$$

This leads directly to

$$\langle B_i(\vec{r})\, B_k(\vec{r}\,')\rangle = \hbar \coth\left(\frac{\hbar\omega}{2k_BT}\right)\mathrm{Im}(\beta_{jn})\, f_{kn}(\vec{r}\,')\, f_{ij}(\vec{r}). \tag{159}$$

.

0.9 Discussion

Qubits with long relaxation times are necessary for quantum computation. Most such devices are controlled electrically. This creates a control – isolation dilemma: connections from the outside world are what make the devices useful, but they are also sources of decoherence. In particular, one may wish to place charge or spin qubits close to metallic device elements used to confine or control the qubits. However, the fluctuating currents and charges in metals give rise to noise that leaks out of the metal into the surrounding region, decohereing the qubits. This is standard physics, (though not often treated in textbooks) and results for the noise spectral densities near a half plane are well known. However, results for the more complicated geometries of real devices have not been available at all. The results presented above represent a first step in the direction of repairing this situation.

Most importantly, we have given a streamlined method for the calculation of both noise spectral densities and noise correlation functions. We have presented new results for the spectral density of cylinders and distant objects, and for the noise correlation functions for half spaces and distant objects. The new method also enables us to give more qualitative, but still useful, discussions of issues such as asperities on metal surfaces.

Numerical estimates of the effect of EWJN on qubits indicates that it is proabably not a dominant effect on the current generation of charge qubit devices. For spin qubits the situation is different. Experiments in which the gates are close to the qubits may already be showing the effects of EWJN.

Spatial Noise Correlations

0.10 Introduction

The most basic justification of the pursuit of quantum computation is the existence of threshold theorems. They tell us that if a certain precision at the qubit level can be achieved, then a workable quantum computer (in principle of arbitrary size) can be made. These thresholds also give concrete goals for hardware performance in systems containing only a few qubits. However, threshold theorems generally make the key assumption that errors on different qubits occur in statistically independent fashion [55]. Some relaxation of this condition can be allowed [56, 57], but error correction then becomes more complicated and resource-intensive. On the other hand, it is known that correlations in noise can actually be used to fight noise-induced degradation in performance, using the concept of decoherence-free subspaces (DFS) [58, 59, 60, 61]. The resources involved in utilizing DFS appear to be less than in most error-correction schemes.

This situation raises some interesting questions. If the noise is correlated, is this fundamentally good or bad for quantum computation? If we have the choice of dealing with the situation by error correction or DFS, which is less expensive? If we do not have a DFS, but there are some correlations in the noise, is it still possible to reduce the computation's susceptibility to noise by appropriate protocols?

We investigate these questions here in two stages. We begin by looking at a small system of only two physical qubits. With very small systems such as this, quantum error correction is of course out of the question. Furthermore, the use of a DFS would prohibit any nontrivial quantum information processing. We will show, however, that significant error *mitigation* is still possible. In an era when quantum computing resources are not nearly sufficient

for true error correction, this is an appropriate subject of research [62]. We will describe methods that may be used for any such system. For illustration purposes, we will use a concrete experimental example: two electron spin qubits in a Si/SiGe heterostructure [63]. This system has the great advantage that it is completely programmable, and we have some insight into the types of noise to be expected [64, 2]. In the second stage of our work, we extend the concepts used for two-qubit systems to many-qubit systems, as far as possible. The overall aim is to understand how to improve quantum information processing when noise correlations are present.

Sec. II introduces the model and constructs the framework to describe the spatial and time correlations in the noise, limiting the discussion to dephasing noise. In Sec. III we propose a measurement scheme to obtain these correlations, which is a simple and easily understood extension of methods used for single qubits [65, 66, 67]. It can also be viewed as a concrete application of much more general schemes given in some recent papers [66, 68, 69, 70]. We apply these methods to the specific system in question to obtain the important auto- and cross-correlation functions. In Sec. IV, we generalize DFS concepts to obtain measures of decoherence that are local in Hilbert space and use these measures to show how to improve the robustness of a quantum circuit. This increases the fidelity obtained for a given quantum information processing task. In Sec. V we apply the method to the model two-qubit system and discuss the advantages and limitations of our recommendations for error mitigation. Sec. VI treats the extensions to many-qubit systems and and addresses the scalability of the method. In Sec. VII we conclude by considering possible generalizations to other error models and how to combine our method with quantum error correction.

0.11 Noise Correlations

The model Hamiltonian for two qubits subject to dephasing noise is

$$H = H_0 + H_g(t) + H_n(t).$$

It consists of

$$H_0 = b_1 Z_1 + b_2 Z_2,$$

a static Hamiltonian that provides the qubit splittings b_1 and b_2 in energy units. (b_1 and b_2 need not be magnetic fields.) $H_g(t)$ is the gate Hamiltonian that is used to do qubit operations. X_i, Y_i, Z_i are the Pauli matrices on site i. The noise Hamiltonian is

$$H_n(t) = \delta b_1(t) Z_1 + \delta b_2(t) Z_2.$$

In the case of electron spins in an inhomogeneous magnetic field, this choice of H models random electric fields that move the qubits and vary their splittings. We use the product basis $\{|00\rangle, |01\rangle, |10\rangle, |11\rangle\}$, which also forms an eigenbasis for H_0. The single-qubit dephasing times $T_2^{(1)}$ and $T_2^{(2)}$ for qubits 1 and 2 are determined by the local noise spectra

$$S_{ij}(\omega) = \int_{-\infty}^{\infty} \langle \delta b_i(t)\ \delta b_j(0)\rangle \cos\omega t\ dt \equiv \langle \delta b_i\ \delta b_j\rangle_\omega$$

on the two qubits. In the simplest theory [71] we have

$$\frac{1}{T_2^{(j)}} = \frac{4}{\hbar^2} \lim_{\omega\to 0} S_{jj}(\omega)$$

as long as the longitudinal relaxation time $T_1^{(j)} >> T_2^{(j)}$, which is usually the case. More accurate formulas can be used, but they do not change the basic physics that T_2 comes from the noise spectrum at low frequencies.

We propose an experiment to measure

$$S_{12}(\omega) = \int_{-\infty}^{\infty} \langle \delta b_1(t)\ \delta b_2(0)\rangle \cos\omega t\ dt \equiv \langle \delta b_1\ \delta b_2\rangle_\omega .$$

This is a correlation function of the noise at different spatial locations.

Measuring $S_{12}(\omega)$ is of interest for two reasons.

First, it tells us something about the nature of the noise. For example, in semiconductor implementations with charge qubits, charge noise is often the dominant decoherence mechanism [72]. If this is due to defects that are far from the qubits, then the noise from the random electric field has wavelengths much longer than the separation of the qubits, and the random electric field is about the same at the two qubits. The opposite limit is when the defect lies between the qubits when we expect anticorrelation in the electric field.

Second, we can use the information to design noise-resistant operations, which is the focus of this work. If $\langle \delta b_1 \ \delta b_2 \rangle_\omega$ is large and positive, then $\langle (\delta b_1 + \delta b_2)(\delta b_1 + \delta b_2) \rangle_\omega$ is large and $\langle (\delta b_1 - \delta b_2)(\delta b_1 - \delta b_2) \rangle_\omega$ is small. Looking back at the noise Hamiltonian for this model we see

$$H_n(t) \approx \delta b_1(t)(Z_1 + Z_2),$$

which only couples to $Z_{tot} = Z_1 + Z_2$. This means that the subspace spanned by $\{|01\rangle, |10\rangle\}$ is approximately a decoherence-free subspace. Conversely, if If $\langle \delta b_1 \ \delta b_2 \rangle_\omega$ is large and negative, then

$$H_n(t) \approx \delta b_1(t)(Z_1 - Z_2)$$

and the subspace spanned by $\{|00\rangle, |11\rangle\}$ is approximately a decoherence-free subspace. By working "near" the appropriate subspace we can get a lower error rate. This is essentially the same idea as singlet-triplet qubits [73], where only two levels are used to define a single logical qubit. Our aim here is quite different. We keep the full 2-qubit system and see if we can use the noise correlations to help design a small quantum information processing device. Since the ultimate aim of the work is to improve the performance of the device, we limit our focus in what follows to correlations that are most likely to lead to simple usable DFSs. As we will see, this limitation also means that out methods work well only when dephasing noise dominates over other noise.

Clearly, the definition of $S_{ij}(\omega)$ generalizes immediately to multiple qubits. We can define cross-correlation functions for any pair and it may well happen that only short-range pairwise correlations are important. The usefulness of such generalizations will be discussed

further in Sec. VI.

0.12 Measuring Correlations

In this section we suggest an experimental strategy to determine the spatial correlations. They are determined by means of a measurement analogous to the measurement of Ramsey fringes. In the 4-dimensional two-qubit space we may choose any 2-dimensional subspace to perform the measurement. However, as we have noted, some subspaces are more likely than others to be DFSs, and these are the most likely to be of real usefulness. Hence we will focus on the two subspaces that are DFSs when the noise is perfectly correlated and when it is perfectly anticorrelated.

Experiment 1. Ramsey in the $\{|00\rangle, |11\rangle\}$ basis.

Let the north pole of a Bloch sphere be $|00\rangle$ and the south pole be $|11\rangle$. We start in the state $|00\rangle$ and then use H_g to make a $\pi/2$ rotation about the y-axis preparing the state

$$\Psi_+(t=0) = \frac{1}{\sqrt{2}}(|00\rangle + |11\rangle),$$

and then let it evolve under the influence of H_0 alone. Then we have

$$\Psi_+(t) = \frac{1}{\sqrt{2}} e^{-i(b_1+b_2)t}|00\rangle + \frac{1}{\sqrt{2}} e^{i(b_1+b_2)t}|11\rangle,$$

and if we make another $\pi/2$ rotation about the y-axis and then measure the probability of being in the state $|11\rangle$ after a time t we get

$$P_+ = \frac{1}{2} + \frac{1}{2}\cos\left[2(b_1+b_2)t\right],$$

so the period is $\tau_+ = \pi/(b_1+b_2)$. The experiment is illustrated in Fig. 1. If we now add in H_n, the noise, we find

$$P_+ = \frac{1}{2} + \frac{1}{2} e^{-t/T_2^{(+)}} \cos\left[2(b_1+b_2)t\right],$$

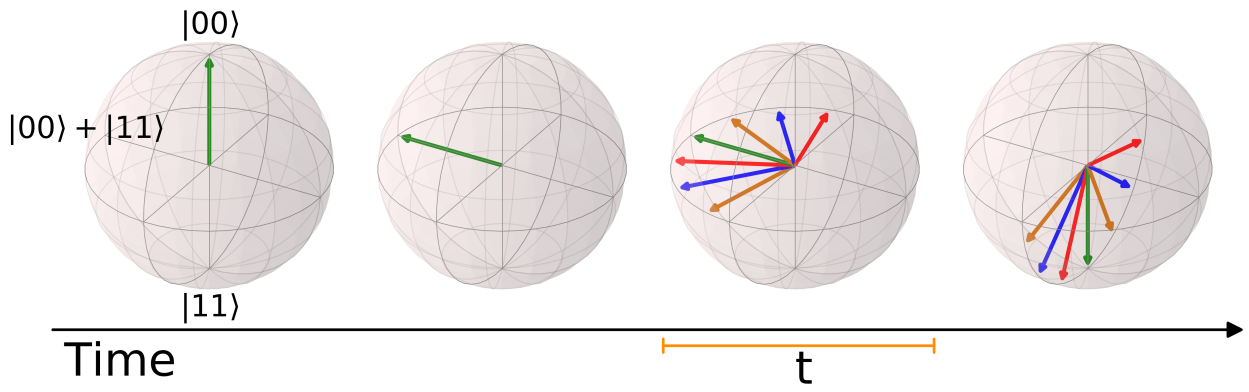

Figure 9: Illustration of the proposed Ramsey-type experiments to measure noise correlations in a Bloch-sphere representation. $T_2^{(+)}$ and $T_2^{(-)}$ are determined by the time decay of the amplitude on the South Pole in Experiments 1 and 2 respectively.

in a certain time window longer than the inverse cut-off time of the noise. (At shorter times the decay is Gaussian.) Here $1/T_2^{(+)}$ is given by the integral of the Fourier transform of $4\left\langle[(\delta b_1+\delta b_2)]^2\right\rangle_\omega$, a windowing function that depends on the approximation being used, and some other factors involving the temperature, $\hbar$, etc. Omitting these prefactors and others that depend on the precise form of the power spectrum we have that

$$1/T_2^{(+)} \sim \left\langle[(\delta b_1+\delta b_2)]^2\right\rangle_\omega .$$

The number of oscillations observed will be N_+, which is

$$N_+ = \frac{T_2^{(+)}}{\tau_+} \sim \frac{b_1+b_2}{4\pi\left\langle[(\delta b_1+\delta b_2)]^2\right\rangle_\omega}.$$

In the case of perfectly anticorrelated collective dephasing N_+ diverges, a signature of a perfect DFS.

Experiment 2. Ramsey in the $\{|01\rangle, |10\rangle\}$ basis.

We start in the state $|01\rangle$ and then use H_g to make a $\pi/2$ rotation about the y-axis in the $\{|01\rangle, |10\rangle\}$ subspace preparing the state

$$\Psi_-(t=0) = \frac{1}{\sqrt{2}}(|01\rangle + |10\rangle).$$

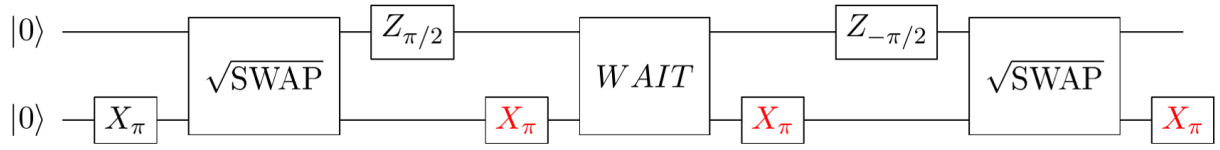

Figure 10: A circuit for performing the Ramsey experiment described in Sec. III. The final three X rotations on the second qubit should be included to prepare Ψ_- and left out for Ψ_+.

We have

$$\Psi_-(t) = \frac{1}{\sqrt{2}} e^{-i(b_1-b_2)t} |01\rangle + \frac{1}{\sqrt{2}} e^{i(b_1-b_2)t} |10\rangle ,$$

and the probability of being in the state $|10\rangle$ after a time t is

$$P_- = \frac{1}{2} + \frac{1}{2} \cos\left[2\left(b_1 - b_2\right) t\right] ,$$

so the period is $\tau_- = \pi / |b_1 - b_2|$. As above, we have

$$1/T_2^{(-)} \sim 4 \left\langle [(\delta b_1 - \delta b_2)]^2 \right\rangle_\omega ,$$

and the number of oscillations is

$$N_- = \frac{T_2^{(-)}}{\tau_-} \sim \frac{|b_1 - b_2|}{4\pi \left\langle [(\delta b_1 - \delta b_2)]^2 \right\rangle_\omega} .$$

For perfectly correlated collective dephasing $(b_1 = b_2)$, N_- diverges, and again we have a DFS.

These two experiments suffice to identify the approximate DFS. If $T_2^+ \gg T_2^-$ then we have the "+" subspace, while if If $T_2^- \gg T_2^+$ then we have the "-" subspace, This determination then fixes all the protocols that we will recommend below. If there is strong noise that also flips the qubits, then (absent artificial symmetries) we do not expect to have even an approximate DFS.

Remarks

There are several gate sequences that will perform the measurements of correlated noise. A particularly simple set is shown in Fig. reffig:swseq.

Once the determination of $T_2^{(+)}$ and $T_2^{(-)}$ has been made, we extract the correlation function $S_{12}(\omega)$ as follows. Since

$$\begin{aligned}\frac{1}{T_2^{(\pm)}} &\sim 4\left\langle\left[(\delta b_1 \pm \delta b_2)\right]^2\right\rangle_\omega \\ &= 4\left\langle(\delta b_1)^2 \pm 2\delta b_1 \delta b_2 + (\delta b_2)^2\right\rangle_\omega\end{aligned}$$

we deduce that

$$\frac{1}{T_2^{(\pm)}} = \frac{1}{T_2^{(1)}} + \frac{1}{T_2^{(2)}} \pm \frac{8}{\hbar^2}\lim_{\omega\to 0} S_{12}(\omega).$$

This determines $S_{12}(\omega)$, which can also be thought of as a quantity that breaks a sum rule on the T_2's - the direction of the breaking depending on whether the noise is correlated or anticorrelated. Of course this is only a rough relation. If there are differences in frequency dependences of the various $S_{ij}(\omega)$ this can modify the conclusions. There is of course nothing in this analysis that limits it to a two-qubit system. In a many-qubit system, $S_{ij}(\omega)$ can be measured in exactly the same way for all pairs.

For ease of presentation we have stuck to the approximation that dephasing depends only on the zero-frequency limit of the S_{ij}'s. Obviously this is not the case for general frequency dependences, and the appropriate modifications lead to substantial quantitative changes in the various T_2's [74]. However, the theory is the same for $T_2^{(+)}$ and $T_2^{(-)}$ as it is for the usual single-particle quantities $T_2^{(1)}$ and $T_2^{(2)}$, so the standard improved formulas can also be applied to better determine the cross-correlation functions. Furthermore, the noise spectroscopy experiments that have now become routine in single-qubit experiments [67] to determine $S_{11}(\omega)$ can be done in exactly the same way to find $S_{12}(\omega)$. The "wait" period in Fig. reffig:swseq is modified to include a sequence of X_1X_2 gates corresponding to a frequency comb which decouples the system from noise at specific frequencies [65, 66]. This can be varied to reconstruct the entire noise spectrum.

0.13 Local Decoherence Measures

With the noise correlations determined, how can we use the knowledge gained to improve the performance of a quantum information processing device? DFS theory offers a simple solution. We set the initial state of the computation to be in the DFS, and we design all subsequent unitary operations so that they never rotate the state out of the DFS. This procedure in principle eliminates decoherence.

In the 2-qubit system with a 2-dimensional DFS we do not have this luxury. The DFS is a two-dimensional subspace so no non-trivial quantum operations are possible. Furthermore, a realistic many-qubit system will not admit a perfect DFS. Still, we can hope to reduce decoherence for the two-qubit system, even if the DFS is only approximate. For a given processing task, many gate sequences are usually possible. The idea is to choose the one most resistant to correlated noise. We achieve this by taking inspiration from the DFS procedure.

In the pure dephasing model we are considering, the only candidates for perfect DFSs are $\text{span}\{|00\rangle, |11\rangle\}$ and $\text{span}\{|01\rangle, |10\rangle\}$. If $T_2^{(+)}/T_2^{(-)}$ is finite, then there is no DFS. Nevertheless, if $T_2^{(+)}/T_2^{(-)} < 1$, then $\text{span}\{|01\rangle, |10\rangle\}$ is the "good" subspace and if $T_2^{(+)}/T_2^{(-)} > 1$, then $\text{span}\{|11\rangle, |00\rangle\}$ is the "good" subspace. As might be expected from symmetry, our conclusions are equally valid for the two cases.

Since the subspaces are good but not perfect, this picture suggests the idea of defining a measure of decoherence for every point in the Hilbert space when noise correlations are present. We call these "local" decoherence measures, "local" here referring to Hilbert space, not real space.

We define two such measures. The first is a geometric measure, called $d_g(|\psi\rangle)$, where $|\psi\rangle$ is any vector in the 4-dimensional 2-qubit space. Let B be an orthonormal basis for the DFS. The projection operator onto the DFS is

$$P = \sum_{|\phi\rangle \in B} |\phi\rangle \langle\phi| ,$$

and then

$$d_g = |(I - P)\psi|^2$$

returns the square of the perpendicular Hilbert space distance from ψ to the DFS. This gives a very simple geometric picture of the decoherence rate of the state as depending only on the distance to the DFS. Clearly $d_g \leq 1$ and $d_g = 0$ for $|\psi\rangle$ in the DFS.

The second decoherence measure, called $d_c\ (|\psi\rangle)$, is obtained by studying the purity γ of a density matrix ρ of the 2-qubit system, defined as $\gamma = \mathrm{Tr}(\rho^2)$. $\gamma = 1$ for a pure state since then $\gamma = \mathrm{Tr}(\rho^2) = \mathrm{Tr}(\rho) = 1$. For the completely mixed state $\rho = I/D$, where D is the dimension of the Hilbert space we find $\gamma = 1/D$. Our interest is in the case $D = 4$. To use γ to form a local measure of decoherence in the Hilbert space we imagine initializing the system at time $t = 0$ in the state $\rho\,(0) = \rho_0 = |\psi\rangle\,\langle\psi|$ so that $\gamma\,(t = 0) = 1$ and then watching γ decrease with time under the influence of the noise Hamiltonian H_n. Denote averages of $\cdot$ over noise realizations by $[\cdot]_{av}$. In this case, $d\rho/dt = \rho' = -i\hbar[\rho, H_n]_{av}$. We are only interested in the short-time behavior of γ so we get

$$\begin{aligned}
\gamma(\delta t) &= \mathrm{Tr}\left[\rho(\delta t)\right]^2 \\
&\approx 1 - \mathrm{Tr}\left[\delta t \rho_0' + \frac{1}{2}\delta t^2 \rho_0''\right]^2 \\
&= 1 - \frac{\delta t^2}{2}\mathrm{Tr}\rho_0\rho_0'' \\
&= 1 - \delta t^2 \mathrm{Tr}\left[\rho_0^2 H_n^2 - \rho_0 H_n \rho_0 H_n\right]_{av}
\end{aligned}$$

We identify

$$d_c(|\psi\rangle) = Tr\left[\rho_0^2 H_n^2 - \rho_0 H_n \rho_0 H_n\right]_{av}$$

as a measure of decoherence that describes how susceptible the pure state $\rho(t)$ is to mixing by the noise. Once again, $\rho_0 = |\psi\rangle\,\langle\psi|$ so d_c is a decoherence measure associated with a point in the Hilbert space of the computer. $d_c = 0$ if $|\psi\rangle$ is in the DFS since H_n acts as a constant operator in the DFS and $[\rho_0, H_n] = 0$. Unlike d_g, however, there is no upper bound on d_c, and d_c has no natural normalization. However, it is only used for comparison of circuits, so this is not a severe drawback.

The two measures differ considerably in their generality. d_g relies only on the identification of a DFS and can be thought of as an extension of the DFS concept. By contrast, to compute d_c one needs only the noise Hamiltonian. d_g is simple to compute and to visualize.

But d_c gives a more complete picture of the decoherence. It is possible that the decoherence is not even a monotonic function of the distance from the approximate DFS. d_g obviously does not capture this possibility. Finally, d_c can clearly be computed also for mixed states, while d_g cannot be, at least by the above definition.

In the course of a quantum information process, an ideal computer remains in a pure state $|\psi(t)\rangle$ that traverses a path in Hilbert space from the initial state $|\psi(t=0)\rangle$ to the desired final state $|\psi(t=t_f)\rangle$ that encodes the answer to the computation or other process. Given this trajectory we can also compute $d_g(t)$ and $d_c(t)$. If these quantities are big on average over the interval $0 \leq t \leq t_f$, then we expect poor fidelity in the result. Of course there is a choice of gate sequences (actually an infinite number) that will take the computer from $|\psi(t=0)\rangle$ to $|\psi(t=t_f)\rangle$. The choice is usually determined by brevity and experimental constraints.

The central contention of this chapter is that one should also take into account the minimization of decoherence. A gate sequence that minimizes $d_g(t)$ and/or $d_c(t)$ in the presence of correlated noise should be preferred. Of course for this small system the fidelity itself can easily be computed and used to minimize the decoherence. However, it is often difficult to understand purely numerical calculations of the infidelity, and the use of d_g and d_c gives physical insight and, as we shall see, can also suggest generalizations to larger systems.

0.14 Results

We test these ideas on two quantum information processing tasks that can be carried out in two-qubit systems, the Deutsch-Jozsa algorithm and Bell-state preparation. These choices were motivated mainly by the fact that they have been carried out successfully in recent experiments [63] so we can use sequences that have actually been shown to be successful. Note that the Bell-state preparation is part of the circuit required for the measurements described in Sec. III.

Noise Model

During the course of the tasks the system is subjected to quasi-static noise with $\vec{\delta b} \equiv (\delta b_1, \delta b_2)^T$ sampled from a bivariate Gaussian distribution with density

$$f(\delta b_1, \delta b_2) = \frac{1}{2\pi\sqrt{\det \Sigma}} \exp\left(-\frac{1}{2}\vec{\delta b}^T \Sigma^{-1} \vec{\delta b}\right).$$

The model assumes zero mean (any deviation from this can be absorbed into the static Hamiltonian H_0) and covariance

$$\Sigma = \begin{pmatrix} \sigma_1^2 & c\sigma_1\sigma_2 \\ c\sigma_1\sigma_2 & \sigma_2^2 \end{pmatrix}$$

where $\sigma_{1,2}$ is the noise strength at qubits 1 and 2 and and c is their statistical correlation. We begin with a simple model in which there is complete correlation of the noise: $\delta b_1(t) \propto \delta b_2(t)$. The strength of the noise may be different on the two qubits. This is quantified by a qubit asymmetry $r = \sigma_1/\sigma_2$, the ratio of the width of the field distribution on qubit 1 to that on qubit 2. For $r = 1$ we are in the "-" subspace. We stress that this fully characterizes the assumed noise model, whether or not several mechanisms contribute to the decoherence.

Further, we take the noise to be quasistatic, so in general noisy non-unitary evolution is achieved by averaging over unitary transformations obtained from exponentiating H_n. For this case, we can develop analytic expressions for the decay times.

$$U = e^{-iH_n t/\hbar} = \begin{pmatrix} e^{-i(b_1+b_2)t/\hbar} & & & \\ & e^{-i(b_1-b_2)t/\hbar} & & \\ & & e^{i(b_1-b_2)t/\hbar} & \\ & & & e^{i(b_1+b_2)t/\hbar} \end{pmatrix}$$

We perform the averaging by integrating the unitary evolution over the probability distribution function implied by our model.

$$\rho(t) = \overline{U\rho(0)U^\dagger} = \frac{1}{2\pi\sqrt{\det \Sigma}} \int U\rho(0)U^\dagger e^{-\vec{b}^T\Sigma^{-1}\vec{b}/2} d\vec{b}$$

We are interested in T_2 for Bell states $|\Psi_+\rangle = \frac{|01\rangle+|10\rangle}{\sqrt{2}}$ and $|\Psi_-\rangle = \frac{|00\rangle+|11\rangle}{\sqrt{2}}$. Thus, we evolve these states and extract the characteristic time scale of the decay of off-diagonal elements of the resulting density matrix. Let's proceed with $\rho(0) = |\Psi_+\rangle\langle\Psi_+|$, the other case is almost identical.

$$U\rho(0)U^\dagger = 1/2 \begin{pmatrix} & & & \\ & 1 & e^{-2i(b_1-b_2)t/\hbar} & \\ & e^{2i(b_1-b_2)t/\hbar} & 1 & \\ & & & \end{pmatrix}$$

So we have to calculate

$$\langle 01|\overline{U\rho(0)U^\dagger}|10\rangle = \frac{1}{2} \times \frac{1}{2\pi\sqrt{\det\Sigma}} \int e^{-2i(b_1-b_2)t/\hbar} e^{-\vec{b}^T\Sigma^{-1}\vec{b}/2} d\vec{b}. \tag{160}$$

$$= \frac{1}{2}\exp\left[-2t^2(\sigma_1^2 - \rho\sigma_1\sigma_2 + \sigma_2^2)/\hbar^2\right]. \tag{161}$$

So the decay is Gaussian, and the associated time scale is

$$\left(\frac{1}{T_{2,0110}}\right)^2 = 2\frac{\sigma_1^2 - 2\rho\sigma_1\sigma_2 + \sigma_2^2}{\hbar^2}.$$

We state the result for the $|\Psi_-\rangle$ initial state

$$\left(\frac{1}{T_{2,0011}}\right)^2 = 2\frac{\sigma_1^2 + 2\rho\sigma_1\sigma_2 + \sigma_2^2}{\hbar^2}.$$

Single qubit T_2's can be obtained in the same way. This allows us to determine σ_1, σ_2, and ρ with single qubit T_2's plus one of the 2-qubit T_2's. To be explicit;

$$\left(\frac{1}{T_2^{(i)}}\right)^2 = \frac{2\sigma_i^2}{\hbar^2}.$$

We can re-write the 2-qubit T_2's in terms of this

$$\left(\frac{1}{T_{2,0110}}\right)^2 = \left(\frac{1}{T_2^{(1)}}\right)^2 + \left(\frac{1}{T_2^{(2)}}\right)^2 - 2\rho\frac{1}{T_2^{(1)}}\frac{1}{T_2^{(2)}}.$$

Then the correlation can be obtained via

$$\rho = \frac{T_2^{(1)} T_2^{(2)}}{2} \left[\left(\frac{1}{T_2^{(1)}} \right)^2 + \left(\frac{1}{T_2^{(2)}} \right)^2 - \left(\frac{1}{T_{2,0011}} \right)^2 \right]$$

For a more general error model where $c \neq \pm 1$, decoherence is simulated by averaging the dynamics over many realizations of the noise numerically. The number of realizations is determined by examining the convergence of the computed quantities as the number increases. We used a convergence criterion of 2%, which was typically achieved after averaging over about 1000 realizations.

Deutsch-Jozsa Algorithm

As the first example, we consider two gate sequences for performing the Deutsch-Jozsa algorithm with a quantum oracle that encodes a balanced function. Following [63], $U_{f_i} = CNOT$ is implemented via exchange interaction and single qubit rotations. Two circuits that perform this algorithm are given in Fig. 11. Even though the initial and final states are the same, the sequences differ very substantially, particularly in their one-qubit gates.

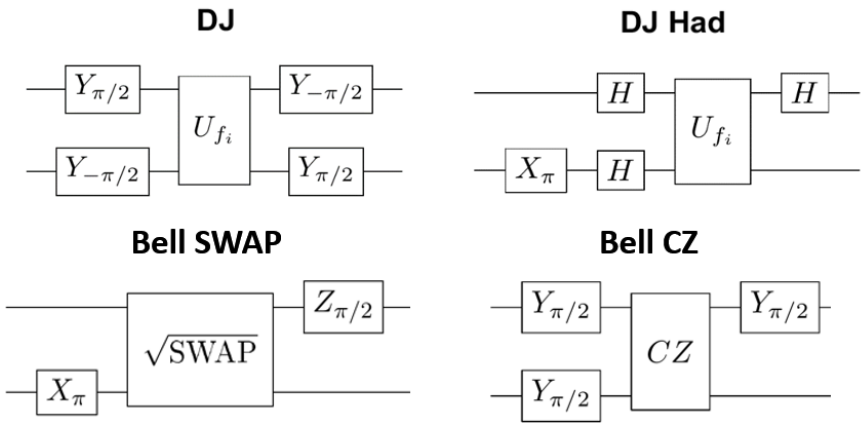

Figure 11: Gate sequences for performing common two-qubit information processing tasks. Top left (right) is the Y-gate (Hadamard gate) circuit for performing the Deutsch-Josza algorithm. Bottom left (right) is the $\sqrt{SWAP}$ (CZ) circuit for preparing a Bell state.

We calculate the ideal unitary evolution for the noise-free system, easily obtained from the gate sequences. We also compute the non-unitary dynamics of each circuit when it is

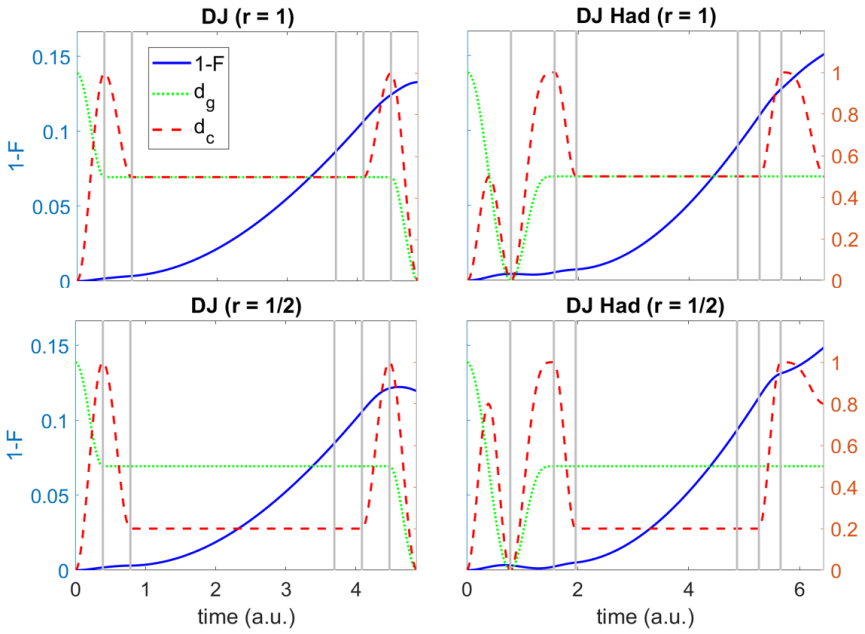

Figure 12: Two different circuits (Fig. 11) for performing the Deutsch-Jozsa algorithm are compared using infidelity along with $d_g(t)$ an $d_c(t)$ for the function $U_{f_i} = CNOT$. The circuits are subject to perfectly correlated quasistatic Gaussian dephasing noise where the ratio between the noise strength at the two qubit locations is r. Gray lines divide the time axis into intervals corresponding to each gate in the circuit.

subjected to noise. The results are summarized in Fig. 12. Comparison of the results of the two calculation allows us to plot the infidelity ($1 - F$, where F is the fidelity) as a function of time. For the computation of $d_g(t)$ and $d_c(t)$ we need only the noise-free state. $d_g(t), d_c(t)$ and the infidelity are all plotted as a function of time in arbitrary units for two different values of r. The relative times for each gate are taken from Ref. [63]. The success of the decoherence measures should be judged by the extent to which they resemble the time derivative of $1 - F$.

We focus first on the left panel of the Fig 12, in which the "Y-gate" circuit is analyzed. One first notes that although $d_g(t)$ and $d_c(t)$ track each other for a substantial portion of the evolution, there is also quite a bit of disagreement between them reflecting the fact that decoherence is not just a matter of distance from the DFS. In part this is because $d_g(t)$ is not sensitive to varying r: indeed its construction assumes an $r = 1$ DFS. This is true even though we chose a quite simple noise model. The difference between $d_g(t)$ and $d_c(t)$ allows us to distinguish certain ways in which one is better than the other. For example, at

short times $1-F$ rises quadratically with time. This is in disagreement with the geometric measure, since $d_g(0)$ is finite. The purity measure, which is linear in t at small times, does better. On the other hand, both measures capture the leveling-off of the infidelity at the end of the interval. In between, the main difference in $d_g(t)$ and $d_c(t)$ is the two bumps in $d_c(t)$. This is reflected only to a very small extent in $1-F$.

The results for the two values of r are rather similar. There is one interesting difference at around $t = 1.5$, where $d_c(t)$ captures the momentary leveling-off in the infidelity better. Comparing $r = 1$ (top) with $r = 1/2$ we see that d_g is not affected by r, whereas d_c and $1-F$ are somewhat reduced. Again, d_c seems to be the slightly better measure.

The right panel shows the same analysis for the "H-gate" circuit. This circuit has an anomalous region, near $t = 2$, where the infidelity actually decreases with time. One can trace this behavior back to an echo effect provided by the X and H gates. These subtleties are not captured by $d_g(t)$ or $d_c(t)$, which are of course both non-negative. Apart from this, the virtues and deficiencies in $d_g(t)$ and $d_c(t)$ are as in the other circuit. Note that both predict the increase in the infidelity at the end of the time interval.

As for using $d_g(t)$ and $d_c(t)$ to decide between the two circuits, the anomalous echoing effect clearly reduces the usefulness of the two measures. Overall, both $d_g(t)$ and $d_c(t)$ are larger for the "Y-gate" circuit, but the final $1-F$ for the two circuits is actually about the same.

In Fig.13 we compare the final $1-F$ and the time integral of $d_c(t)$ for a large range of values of the asymmetry r and the correlation c for the Y-gate circuit. In this circuit there is no anomalous behavior of $1-F$. It seems that when this is the case, then the integral of $d_c(t)$ is indeed a good predictor of fidelity for correlated ($c = 1$), uncorrelated ($c = 0$) and anti-correlated ($c = -1$) noise. This is true even when the noise is much stronger on one of the qubits.

Bell-state Preparation

The circuits start from an initial state $|00\rangle$ and end in the Bell state $(|01\rangle + |10\rangle)/\sqrt{2}$. The first circuit we call the $\sqrt{SWAP}$ circuit and the second is the CZ circuit. The names reflect the fact that the main difference between the two circuits is the nature of the entangling

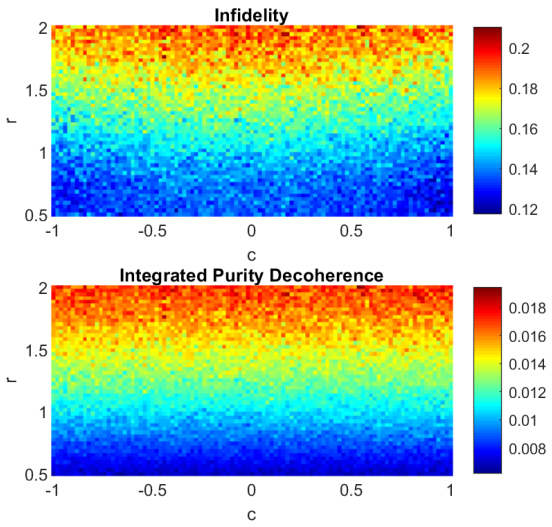

Figure 13: The final infidelity and integrated purity decoherence d_c for the Y-gate Deutsch-Jozsa gate sequence with $U_{f_i} = CNOT$.

gate. $d_g(t)$, $d_c(t)$, and $1 - F(t)$ are plotted in Fig. 14.

The comparison of the two circuits is more straightforward here, since there is no anomalous behavior in $1 - F(t)$. In the CZ circuit, the time integrals of $d_g(t)$ and $d_c(t)$ are both clearly bigger than in the $\sqrt{SWAP}$ circuit. Both measures predict that the final $1 - F$ should be bigger for the CZ circuit, and indeed it is. It is also true that the shape of $1 - F(t)$ resembles the integral of $d_c(t)$.

Passing to the r-dependence of the $\sqrt{SWAP}$ circuit, we note that at later times $t > 2$, $d_c\,(t)$ shows significant differences between the $r = 1$ and $r = 2$ cases. This is faithfully reflected in the higher final infidelity for $r = 2$. We note once more that near $t = 0$, $\mathrm{d_c}\,(t)$ is linear in time, while $d_g(t = 0)$ is finite and $1 - F$ is quadratic. Thus $d_c\,(t)$ always seems to be superior to $d_g\,(t)$ when $1 - F$ is small.

In Fig. 15 we again plot the the final $1 - F$ for a range of r and c and compare it to the time integral of $d_c(t)$ for the $\sqrt{\mathrm{SWAP}}$ Bell-state circuit. In contrast to the Deutsch-Jozsa Y-gate circuit, there are substantial differences between the two quantities. We see that the impurity is roughly independent of the asymmetry r, both qubits contributing roughly equally. In contrast, the fidelity depends more strongly on the asymmetry. This comes from the asymmetry of the circuit itself, specifically that there is an X-gate applied to qubit 2 but not to qubit 1. The X-gate echoes away the decoherence created by noise on qubit 2 but

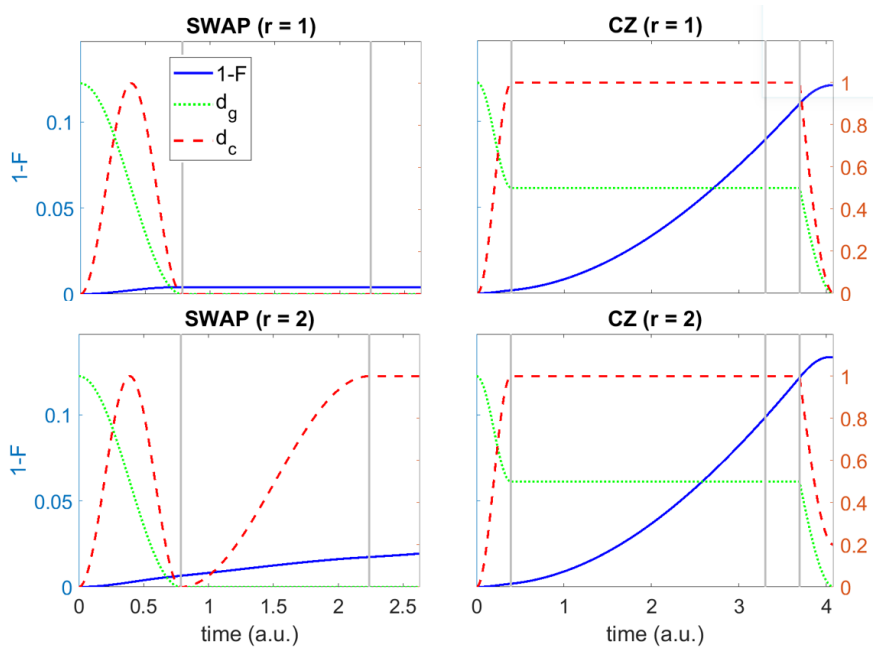

Figure 14: Comparison of two circuits for preparing the state $\Psi = (|{\downarrow\uparrow}\rangle + |{\uparrow\downarrow}\rangle)/\sqrt{2}$ to perform one of the measurements described in Sec. II. The left panels are for the Bell SWAP circuit and the right panels are for the Bell CZ circuit. The top panels are for $r = 1$ so the noise strength is the same on the two qubits. The bottom panels are for $r = 2$ so the noise strength is stronger on qubit 1. The solid blue, dotted green, and red dashed lines are respectively the state infidelity $1 - F$, the DFS projection metric d_g, and the purity-based decoherence d_c for each circuit as a function of time. The system is subject to quasistatic Gaussian dephasing noise. $d_g(t)$ and $d_c(t)$ are scaled and overlaid against the infidelity to illustrate how they capture dephasing effects. Gray lines divide the time axis into intervals corresponding to each gate in the circuit.

not that on qubit 1. Thus, once more we see that echo effects can reduce the information supplied by local decoherence measures. This indicates a subtle but important drawback to the use of $d_c(t)$ as a circuit quality measure, which stems ultimately from the difference between purity and fidelity. Consider the enlarged state space of the 2-qubit circuit as the real 15-dimensional Hilbert space of density matrices (actually a compact subset of this space when positivity constraints are added.) Each density matrix is a point in the space. The pure states live in a 6-dimensional submanifold. $1 - F$ is a measure of the distance in this space from the desired final state to the actual one: we may think of it as the length of the difference vector. The desired final state is a pure state. The integral of $d_c(t)$, however, only provides one component of the difference vector - essentially the vector that is perpendicular to the subspace of pure states. There is also a component of the difference vector parallel to

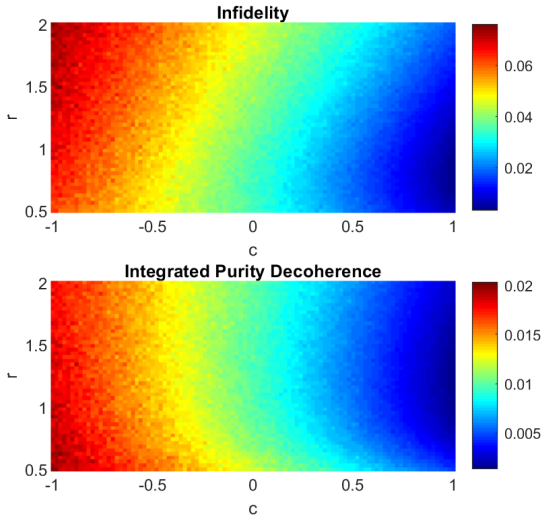

Figure 15: The final infidelity and averaged purity decoherence d_c for the $\sqrt{\text{SWAP}}$ Bell-state circuit. As explained in the text, the purity decoherence serves as a good predictor for the derivative of the fidelity so the integral, or average, over the gate sequence shares the same features as the infidelity.

the subspace. The vectors are shown schematically in Fig. 16.

0.15 Extension to Many Qubits

As noted above, if only a few qubits are involved and the noise model is known, the best strategy for deciding on a gate sequence is simply to calculate the infidelities. As the number of qubits increases, the length of this computation increases exponentially, and it soon becomes impractical. The same holds for the computation of $d_g(t)$ and $d_c(t)$, since they depend on the many-body wavefunction. The question is whether we can use the physical insight gained for few-qubit systems to give a meaningful presciption for "scoring" long gate sequences in a multi-qubit computer. We propose that this is indeed possible, based on a picture of the errors that occur during the computation as steps in a random walk, the walk taking place in a moving frame generated by the algorithm.

The density matrix space R for an n-qubit computer has real dimension $4^n - 1$. The Hilbert Schmidt inner product on R defines what is essentially a Euclidean distance metric. An error-free computation with circuit depth k consists of a sequence of k points in this

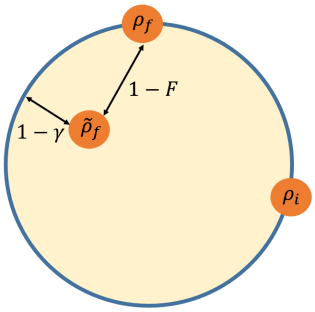

Figure 16: Schematic projection of the 2-qubit state space R as a ball with the boundary containing the pure state submanifold. The pure initial (ρ_i) and error-free final (ρ_f) states of an algorithm, and the partially decohered result of running that algorithm in a noisy environment are labeled ($\widetilde{\rho}_f$). State fidelity F provides a measure of closeness between the two states ρ_f and $\widetilde{\rho}_f$, while the impurity $1-\gamma$ only represents closeness to the pure state subspace.

space, labeled ρ_t, $t = 0, 1, 2..., k$. The states ρ_t are all pure, so this ideal evolution takes place in the $2^{n+1}-2$-dimensional submanifold of pure states. This non-random evolution moves by large distances at each step and defines a moving frame in R. In this moving frame the errors define a random walk, assuming that there is no correlation between the sequence defined by the algorithm and the local decoherence.

Taking a clue from the definition of d_g, decoherence will be worse if the random walk increases the perpendicular distance of ρ_t to the DFS. If we could compute a probability distribution $P_\perp$ for the perpendicular component of the steps in the walk then the expected value of the perpendicular distance after t gates would be $\langle d_t^2 \rangle^{1/2} = \sqrt{t}L$, where L is the rms step length computed using $P_\perp$. We may think of different gate sequences as having different $P_\perp$.

We therefore assign a "perpendicular step size" to every one or two qubit gate G. Since the walk takes place close to the manifold of pure states, We can use the usual Hilbert space $\mathcal{H}$ and we arrange the basis of $\mathcal{H}$ so that the D basis vectors of the approximate DFS, which we call $\mathcal{C}$, come first, and the $2^n - D$ vectors of the orthogonal complement $\mathcal{C}_\perp$ come second. We then partition the unitary matrix of G into four sectors:

$$G = \begin{pmatrix} G_\parallel & M \\ M' & G_\perp \end{pmatrix},$$

where $G_\parallel$ and $G_\perp$ move the state around $\mathcal{C}$ and $\mathcal{C}_\perp$ respectively. M and M' move weight between $G_\parallel$ and $G_\perp$. A "good" gate has $M = M' = 0$ since a state in C undergoes no perpendicular motion and therefore remains in $\mathcal{C}$ and a state in $\mathcal{C}_\perp$ undergoes random motion that is not biased in the perpendicular direction. M and M' give perpendicular motion and if they are large then G is a bad gate, i.e., one that we expect will increase the decoherence to which the state is exposed. To quantify this we use the unitarity of G and index the blocks of G as follows. The upper left corner $G_\parallel$ is indexed by $s_{G_\parallel} = (i, j)$ such that $1 \leq i \leq D$ and $1 \leq j, \leq D$; the lower right corner $G_\perp$ is indexed by $s_{G_\perp} = (i, j)$ such that $D + 1 \leq i \leq D_H$ and $D + 1 \leq j \leq D_H$; the upper right corner M is indexed by $s_M = (i, j)$ such that $1 \leq i \leq D$ and $D + 1 \leq j \leq D_H$; the lower left corner M' is indexed by $s_{M'} = (i, j)$ such that $D + 1 \leq i \leq D_H$ and $1 \leq j \leq D$.

We then define

$$B(G) = \frac{1}{4}\left(\sum_{(i,j)\in s_M} |M_{ij}|^2 + \sum_{(i,j)\in s_{M'}} |M'_{ij}|^2\right)^{1/2},$$

which is just a Euclidean measure of the size of the off-diagonal blocks. This may be thought of as the "badness" of G. The unitarity of G and the fact that one- and two-qubit gates are nearly diagonal imply that $0 \leq B \leq 1$. Table 1 gives the badness of several common gates. A circuit A then may be thought of as a random walk with N_A gates and the analog of the integral of d_g over the total circuit is

$$d_A = \sqrt{\sum_G B^2\,(G)}.$$

We expect the infidelity to be roughly proportional to this quantity. The key point is that we never need to compute any wavefunctions or other many-body quantities. Each one- and two-qubit gate has only a small number of off-diagonal elements, so the computation of B is efficient - in fact it is very fast. Thus we may score different gate sequences and choose the right one for our multi-qubit computation without prohibitive overhead.

We now propose a protocol for improving the performance of a many-qubit computer. The first step is a calibration phase, in which the experiments given in Sec. III are performed

G	$B(G)$
X	$1/2$
Y	$1/2$
Z	0
H	$2^{-5/4}$
CNOT	$2^{-3/2}$

C	d_A	$1-F$
Bell SWAP	0.500	0.004
Bell CZ	0.728	0.011
DJ	0.912	0.019
DJ Had	0.951	0.034

Table 1: On the left, badness $B(G)$ for some typical one and two qubit gates G. The right table shows d_A for a few of the circuits studied above, demonstrating the correspondence between d_A and final state infidelity. The calculation assumes the existence of an approximate DFS spanned by $\{|\uparrow\downarrow\rangle, |\downarrow\uparrow\rangle\}$.

for each pair of qubits. This gives all two-point correlation functions. Each pair of qubits is assigned a "+" sign or a "-" sign according to the results for T_2^+ and T_2^-. This then determines an approximate DFS for each pair. In the second step every one- and two-qubit gate G is assigned a score $B(G)$ and each candidate circuit A is assigned a score d_A. Finally, the circuit with mininum d_A is chosen.

Our model system gives numerical evidence for the validity of this idea, since it can process tasks with distinct circuits. These are the same circuits for Bell state preparations and the Deutsch-Jozsa algorithm from Sec V. Table VI.I shows some individual gate scores, and then d_A and $1-F$ for 4 circuits. One sees that $1-F$ and d_A are monotonically related, but not strictly proportional. This result is encouraging, but it is obtained for a very small system. Further work on larger systems will be needed to confirm the basic concepts and to refine the protocol.

0.16 Discussion

We have presented a method to measure spatial noise correlations in quantum information processors, focusing on those correlations that are most important for error mitigation. It was formulated for a 2-qubit machine, but it is clearly also immediately applicable to any 2-point correlation in a machine of arbitrary size. This information is sufficient to identify approximate DFSs, which in turn informs the design of gate sequences. This is done by identifying decoherence measures that are local in Hilbert space, and using sequences that

avoid regions where these measures are high. These measures can only be computed in few-qubit systems, which limits their usefulness. However, they point the way to a method that assigns scores to individual gates even in many-qubit systems. By means of a picture of errors generating a random walk in the state space, we can give a score to any candidate circuit. A circuit with a low score will be more resistant to correlated noise. This is confirmed by numerical calculation on a two-qubit system.

The method clearly does not offer a complete picture of the situation.

We found in particular that some circuits have echo effects that actually increase the fidelity (at least for a short time). Our decoherence measures do not capture this, though it is unclear whether this is ever a large effect.

It is also unlikely that the method is very useful for very general error models. We considered only dephasing noise. It is easy to produce 2-dimensional DFSs for this type of noise. If other noise that, for example, flips spins, is added, these DFSs disappear immediately. That does not prevent us from defining the decoherence measure d_c, which we found to be the most useful one, but if it varies little as we move around the space, it loses its power to distinguish different circuits.

The many-qubit method is however well-designed to be used in conjunction with error correction. It assumes that the system stays reasonably close to the pure state manifold, meaning that its usefulness degrades as k, the circuit depth, increases. However, if k instead represents the number of gates that are performed between each error-correction cycle, k can optimized to take advantage of our method. k will be larger for better circuits.

Coherent Error Correction

0.17 Fault Tolerance

A quantum error correction scheme encodes a logical qubit in many physical qubits. The usefulness of one of these schemes is characterized by its threshold physical error rate p_{th}. For physical qubit error rates lower than p_{th}, the encoded qubit will suffer logical errors less often than any of the physical qubits. This ensures that the encoding is actually protecting the data rather than just complicating it, and allows us to design a concatenated scheme of codes to reduce the logical error rate arbitrarily close to 0. If logical errors can occur due to a single physical error happening somewhere in the circuit, there is no chance for a threshold error rate. A way to protect against this problem is to insist that the circuit is "fault tolerant." A fault tolerant error correction circuit is defined through a few principles, the most relevant for this work being that a single error on a physical qubit during the error correction circuit does not propagate to many errors at the output. A fault tolerant circuit will have logical error probability proportional to the physical error rate squared, at worst. This ensures a finite threshold error rate.

Naive implementations of coherent error correction circuits (CEC) in [75] violate Shor and Preskill's principles of fault tolerance. These circuits have many data qubits coupled to the same ancilla qubit via CNOT gates. The "back action" of these CNOT gates allows for the propagation of one phase error in the ancilla to propagate to many errors in the data. The typical resolution of this for stabilizer codes is to use many ancillas. The number of ancillas necessary for any given syndrome measurement should be equal to the number of 1s in the row of the parity check matrix corresponding to the syndrome bit. In stabilizer language, the number of ancillas should be equal to the weight of the stabilizer operator that

is being measured. Many of the CEC Steane code and Bacon-Shor code implementations in the literature do not include these extra ancillas they do not produce threshold values at all.

Back-Action Error Propagation

Preskill writes "if a phase error occurs in one qubit, and that qubit is then used as the target qubit of an XOR gate, then the error will propagate 'backward' to the source qubit." [56] Here we will exemplify this notion and explore how it affects circuit construction for CEC. Consider two qubits coupled together with a CNOT gate. These will soon adopt the roles of a data qubit in state $|\psi\rangle$ and an ancilla qubit prepared in the $|0\rangle$ state. Using a well-known identity we have the following.

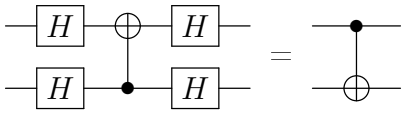

This can be shown quite simply in the computational basis where the action of the CNOT gates are given by the following unitary matrices.

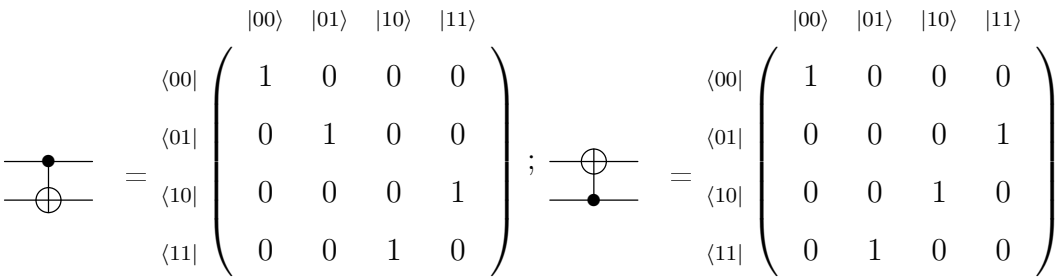

So we can compute the left hand side of the identity and we find that is indeed the matrix for the CNOT gate with qubit 1 acting as the control.

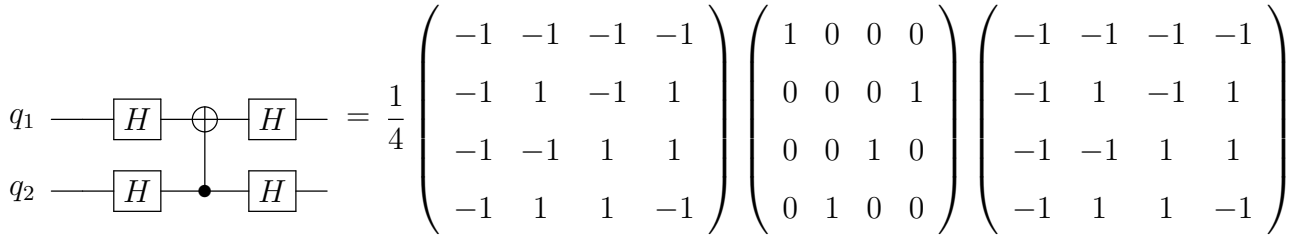

$$= \begin{pmatrix} 1 & 0 & 0 & 0 \\ 0 & 1 & 0 & 0 \\ 0 & 0 & 0 & 1 \\ 0 & 0 & 1 & 0 \end{pmatrix}$$

To see how the "back-action" error works consider two qubits in general states $|\psi\rangle = a|0\rangle + b|1\rangle$ and $|\phi\rangle = c|0\rangle + d|1\rangle$. We introduce a phase error on the second qubit before the gate operation.

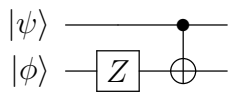

$$\begin{pmatrix} 1 & 0 & 0 & 0 \\ 0 & -1 & 0 & 0 \\ 0 & 0 & 1 & 0 \\ 0 & 0 & 0 & -1 \end{pmatrix} \begin{pmatrix} 1 & 0 & 0 & 0 \\ 0 & 1 & 0 & 0 \\ 0 & 0 & 0 & 1 \\ 0 & 0 & 1 & 0 \end{pmatrix} \begin{pmatrix} ac \\ ad \\ bc \\ bd \end{pmatrix} = \begin{pmatrix} ac \\ -ad \\ -bd \\ bc \end{pmatrix}$$

We can understand this a little better by relating this final state to the state we would have expected with no error.

$$= \begin{pmatrix} 1 & 0 & 0 & 0 \\ 0 & -1 & 0 & 0 \\ 0 & 0 & -1 & 0 \\ 0 & 0 & 0 & 1 \end{pmatrix} \begin{pmatrix} ac \\ ad \\ bd \\ bc \end{pmatrix} = \begin{pmatrix} 1 & 0 & 0 & 0 \\ 0 & -1 & 0 & 0 \\ 0 & 0 & -1 & 0 \\ 0 & 0 & 0 & 1 \end{pmatrix} \begin{pmatrix} 1 & 0 & 0 & 0 \\ 0 & 1 & 0 & 0 \\ 0 & 0 & 0 & 1 \\ 0 & 0 & 1 & 0 \end{pmatrix} \begin{pmatrix} ac \\ ad \\ bc \\ bd \end{pmatrix}$$

Comparing the first and last expressions in the above chain of equalities we have

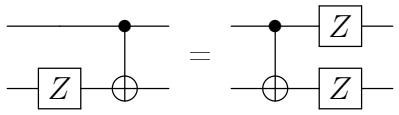

The Z operator on the control qubit exemplifies the unwanted back action.

To see how this effect occurs in stabilizer circuits, we will consider a method to extract syndrome information. Schematically, we couple a set of encoded data qubits to an ancilla qubit can with the following circuit, which stores the measurement value of Z_1Z_2 on the

ancilla.

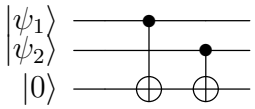

In principle, this is not fault tolerant. A single Z error on the ancilla qubit will propagate to the data qubits.

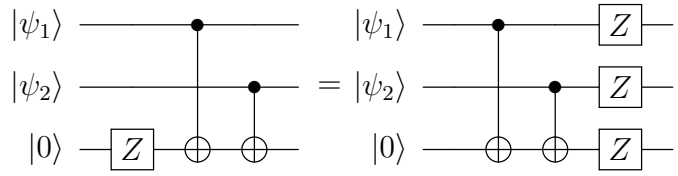

In practice, however, the output of this circuit is identical to the errorless implementation depicted above. This can be a source of logical error if these CNOT gates are situated between Hadamard gates. Storing stabilizer values in QEC involves these problematic gate sequences in both measurement-based and coherent error correction.

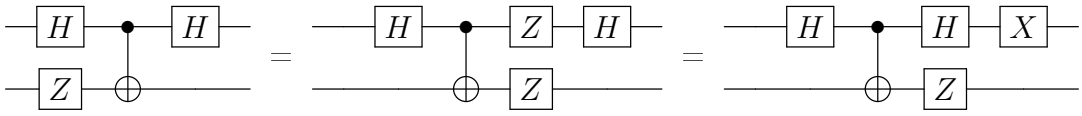

The phase flip on the ancilla propagates to the data qubit and shows up at the output as a bit flip error. If this ancilla is coupled to two data qubits, the circuit is not fault tolerant.

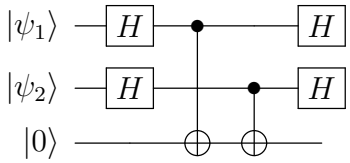

Now we can see what happens if a phase error occurs on the bottom qubit.

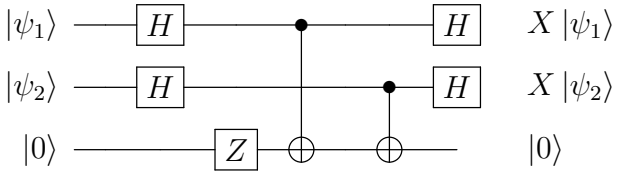

This circuit fails to meet the requirements of fault-tolerance since a single qubit error propagated to many data qubits. Situations like this are not always fatal, as we will see when we consider a real stabilizer code in the next section.

0.18 Steane Code Circuit

We do not review the full Steane code here, but the most important facts are that it is distance 3 stabilizer code, so it can correct all single qubit errors. It is also a CSS code, meaning we can separate the stabilizer generators into X-type and Z-type, so we can correct the two types of errors independently. It is useful to think of the circuit in Fig. 17 in quarters. The first and third quarters extract error syndromes for Z- and X- type errors, and the second and fourth quarters correct those errors. In contrast to most stabilizer code circuits, we use an extended set of stabilizers to identify errors. Typical implementations of the Steane code require the extraction of six stabilizer generators repeated until a majority-rules criterion is met to ensure that correction operations are actually due to qubit errors and not faulty measurements. Here, we instead extract syndromes using the entire stabilizer group to build in the redundancy we need to ensure fault-tolerance. More detail on this is given in the next chapter.

The C_kNOT gates used for error correction are inherently fault tolerant since it takes several faulty ancilla qubits to flip a data qubit. The problem appears in the syndrome extraction portion of the circuit. In Fig. 18 we can see several data qubits coupled to the same ancilla qubit. This is how we store the value of the stabilizer operators for this code. For example, the first ancilla qubit stores the value of the stabilizer $X_1X_5X_6X_7$. Since this ancilla qubit is coupled via $CNOT$ gates to several data qubits, a phase error on this ancilla qubit would propagate to four data qubits. There is no issue here, since the error propagated to the data is in fact in this code's stabilizer group. The dangerous errors are those which occur on an ancilla qubit after two $CNOT$s.

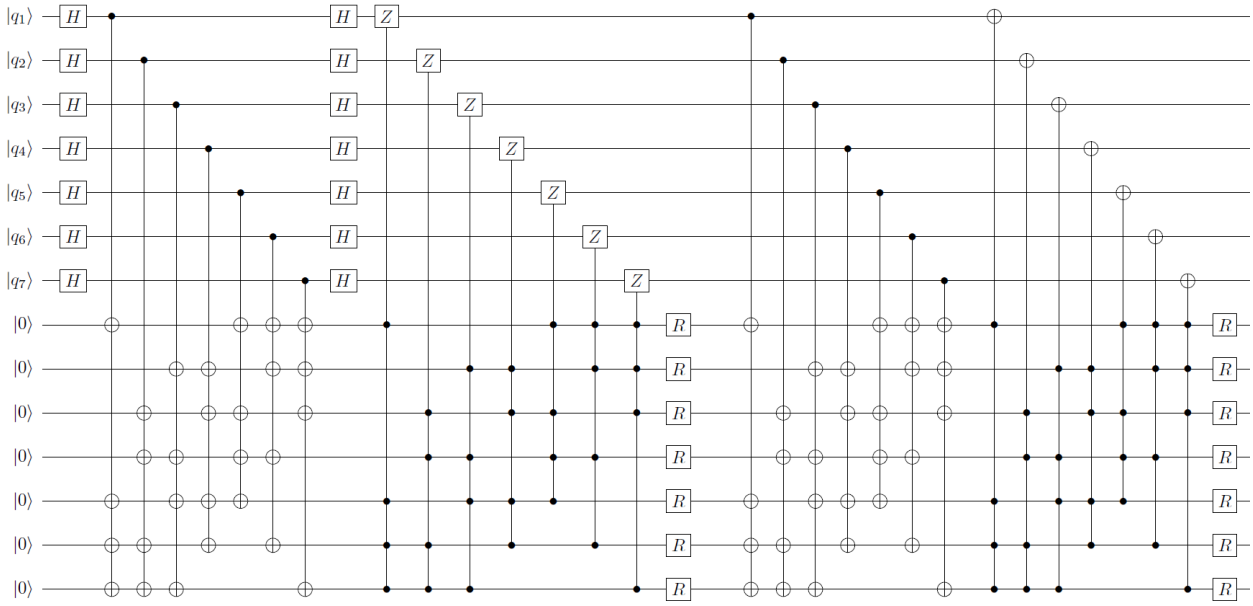

Figure 17: The proposed full coherent error correction circuit for the Steane code with redundant stabilizer measurements. It is best to think of this in quarters, the first extracting syndromes for phase errors, the second correcting them and the last half doing the same for bit flip errors. R gates reset the ancilla qubits to $|0\rangle$

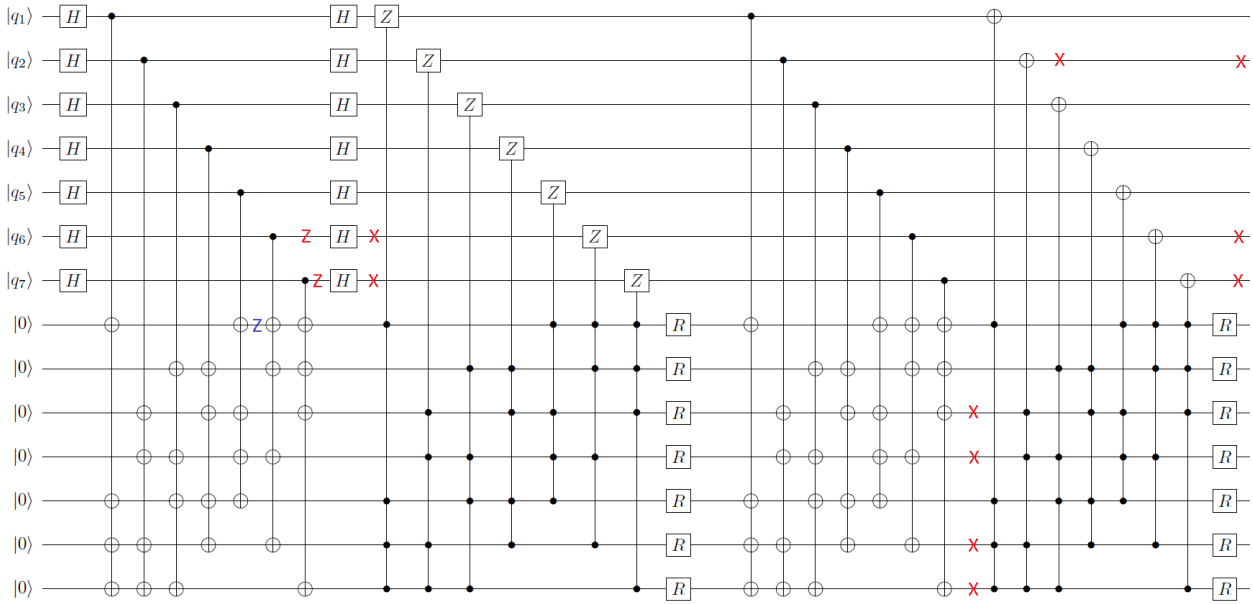

Figure 18: A possible fault path demonstrating how a single physical error can produce a logical error in the error correction circuit in Fig 17. The physical error is in blue, and the propagation of that error through the circuit is highlighted in red.

Back-Action Logical Errors

The other where either one, three, or four errors are propagated to the data are not dangerous.

Four errors will always be equal to a stabilizer, one error will be corrected appropriately, and

three errors are the same as 1 error, up to multiplication by a stabilizer. If a phase error happens on an ancilla qubit "halfway" through a syndrome extraction sequence, this phase error will propagate via $CNOT$ back-action to two data qubits. These phase errors will be rotated into bit-flip errors by Hadamard gates. In the bit-flip syndrome extraction phase, these two errors will be interpreted as a third error. In Fig. 18 we see that the $CNOT_k$ gates controlled by the faulty sixth and seventh data qubit will target the ancilla qubits associated to the C_kNOT gate which corrects the second data qubit. This amounts to three bit flip errors at the end of the error correction circuit due to one phase error in the ancilla. These three errors will amount to a logical X error on the data. This is not a pathology of our circuit, but rather a consequence of the code. That is to say, we cannot eliminate this problem by re-ordering gates or choosing new stabilizers.

To understand this we can look at the algebra of syndromes for the Steane code. Via back-action, a single phase error can result in two bit-flip errors. Supposing we take $2n$ stabilizers, these bit flip errors X_1 and X_2 will have associated syndromes S_1, S_2 in a vector space of dimension n over $\mathbb{Z}_2$. Storing both S_1 and then S_2 on n ancilla qubits will cause the circuit to read the syndrome $S_3 = S_1 \oplus S_2$. Since stabilizers form a group, this will be a legitimate syndrome indicating a single qubit error in the data block other than X_1 or X_2. The C_kNOT gate controlled by S_3 will erroneously introduce a bit flip X_3 to the data block. The combination $X_1X_2X_3$ will always be equal to the logical X operator on the code. The syndrome $(S_1 \oplus S_2) \oplus S_1 \oplus S_2 = 0$, so $X_1X_2X_3$ commutes with every stabilizer. Since it is not a stabilizer operator we can be sure it is a logical bit flip error.

If these errors are truly present, they should dominate the logical error rate at low physical error rates and we can make a prediction for $p_{log}(p)$. This amounts to counting the error sites between the first and second pair of $CNOT$ gates on each ancilla qubit and modifying this number by the fraction of errors that will involve a phase flip. These modifying factors arise from observing that two of the three single qubit errors and 8 of the 15 two qubit errors involve phase rotations. This counts the number of possible single errors that result in logical errors, hence giving us a prediction for the logical error rate as a function of the physical error rate. If the dangerous memory and gate error sites are N_{memory} and N_{gate} respectively

we have

$$p_{log}(p) = \left(N_{memory} \times \frac{2}{3} + N_{gate} \times \frac{8}{15} \right) p + \mathcal{O}(p^2) \approx 11.73\, p.$$

This prediction is plotted on top of the simulated results in Fig 19.

Simulation Comparison

The presence of logical errors that occur at a rate proportional to the physical error rate means that this circuit should have no threshold. We then need to explain why previous work indicated otherwise. This stems from a crucial assumption of the prior simulation, which is that ancillas can be treated as purely classical bits. Each of the ancilla qubits was stored as either 0 or 1, and if in the course of the random error assignment a phase operator Z was applied to an ancilla, it was instead replaced with the identity. To test the validity of this

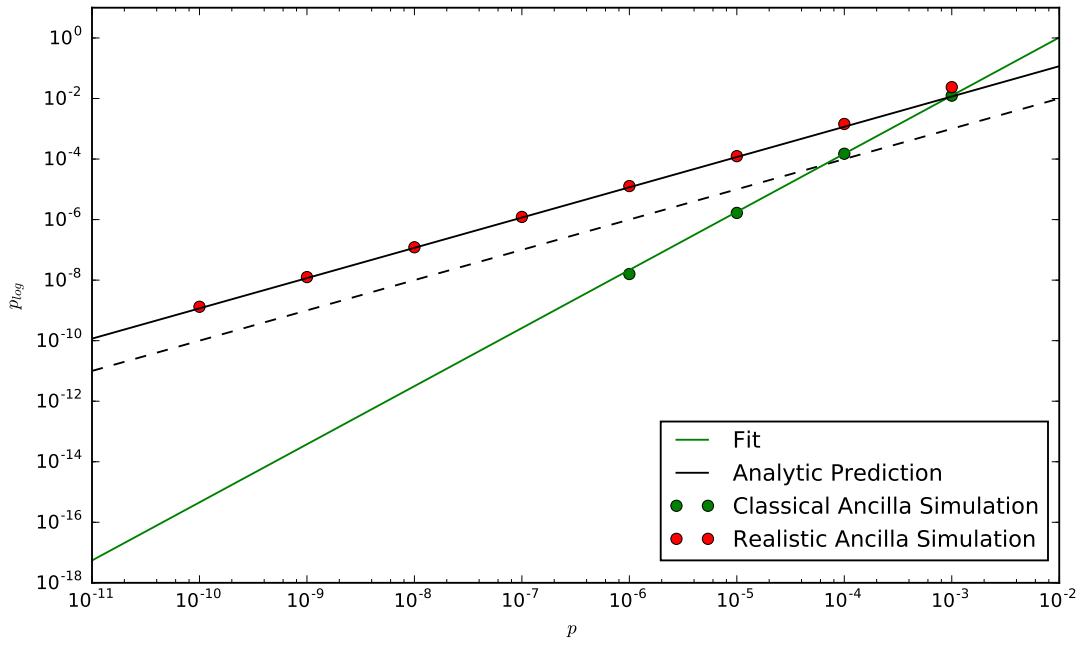

Figure 19: Simulation data comparing two methods of treating ancilla qubits in the coherent error correction Steane circuit. We emphasize that both curves are produced by the same circuit. The difference comes from the treatment of ancillas as either quantum or classical bits. The dashed line represents $p_{log} = p$.

assumption, we simulated the same circuit first using classical ancillas and again treating

data and ancilla qubits alike. The results are plotted in Fig. 19. In the first case we see a threshold value $\sim 10^{-5}$ and in the second case there was no threshold and the data matches our prediction based on back-action induced logical errors very well. We see that back-action induced logical errors indeed dominate p_{log} at low p.

Revised Circuit

Fortunately we can fix this problem. While there are several single ancilla errors that may propagate to many data qubits, there are only a few of these that cause logical errors. This is because of the stabilizer structure of the code. If we can arrange gates to extract each stabilizer in a single time step, therefore eliminating the possibility for errors to happen during syndrome extraction, we can recover a threshold even with realistic ancilla qubits. By using CNOT_k gates for syndrome extraction, the circuit in Fig 20 has this property. Although a single error on the ancilla can propagate to many data qubits, this will always result in a multiqubit error that is in the code's stabilizer group, hence there is no effect on the state of the data block. We emphasize that stabilizer extraction in a single time step is the key revision, since otherwise this method is not fault tolerant and there will be no threshold.

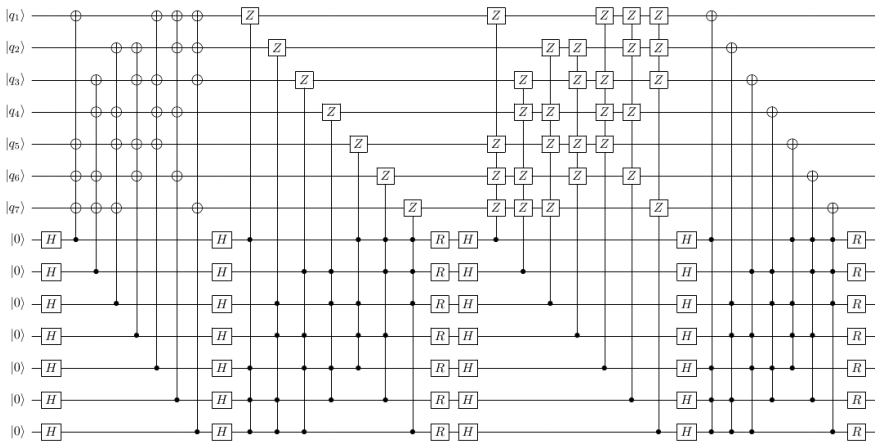

Figure 20: Revised syndrome extraction avoids any logical errors through back-action by extracting each stabilizer to an ancilla in a single time step.

Upon revisiting the circuit with correct treatment of ancillas and some other details adjusted to produce a more realistic threshold and we found $p_{th} = 3.88 \times 10^{-5}$.

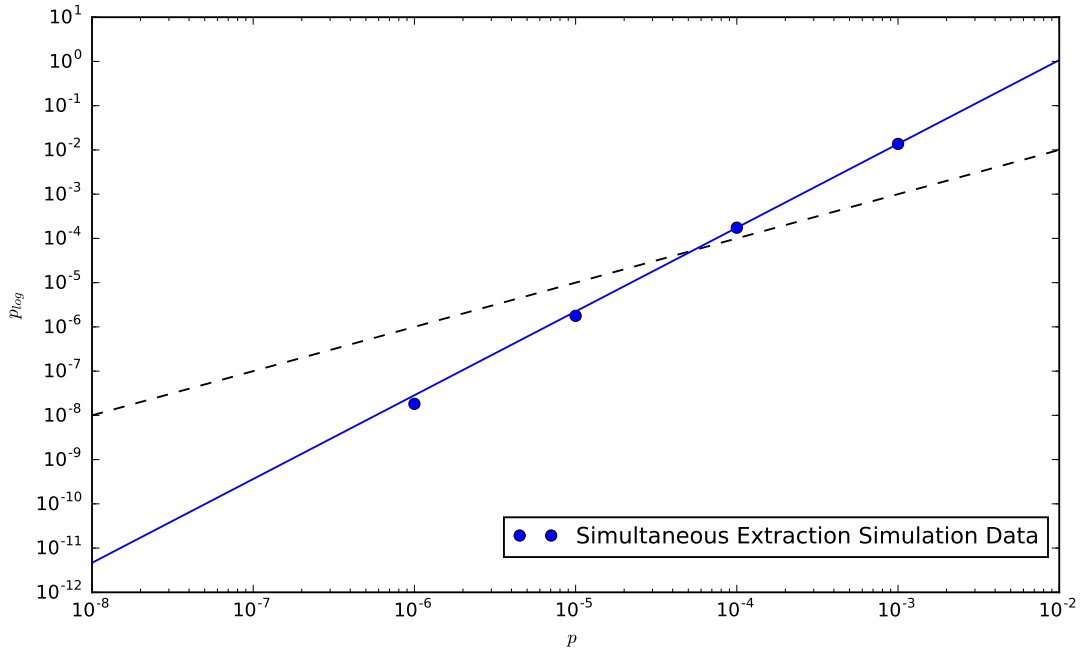

Figure 21: The behavior of p_{log} with the revised circuit presented in Fig 20 showing that a threshold does exist when we consider quantum ancilla bits. The dashed line represents $p_{log} = p$

0.19 Stabilizer Simulation of Non-Clifford Controlled Gates

QEC circuits can typically be divided into two parts, syndrome extraction and error correction. Syndrome extraction refers to encoding the values of stabilizer operators on the possibly erroneous codeword stored on the data qubits to the ancilla qubits.

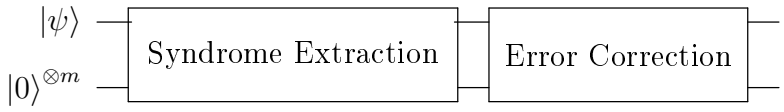

In this chapter's circuits we have used several C_kNOT gates to do error correction. To simulate them, we had to work around the fact that these gates are not simulable in the stabilizer formalism [76]. Here we aim to show that a C_kNOT gate can be simulated in the stabilizer formalism using false "measurement." We do this by showing that after syndrome extraction the state of the data and ancilla is separable, and we can write the state as a product of data and ancilla states. The syndrome extraction portion of the circuit consists

of gates which encode the syndrome into the ancilla and Pauli errors that may occur on any of the data or ancilla qubits. First we need a few definitions [77].

Definition 1. *The* ***Pauli group on n qubits*** $\mathcal{P}_n$ *consists of* $2^n \times 2^n$*-dimensional matrices of the form* $\lambda P_1 \otimes \cdots \otimes P_n$ *where* $\lambda \in \{\pm 1, \pm i\}$ *and* $P_1, \ldots, P_n \in \{I, \sigma_1, \sigma_2, \sigma_3\}$.

Definition 2. *The* ***Clifford group on n qubits*** $\mathcal{C}_n$ *is the normalizer of* $\mathcal{P}_n$ *inside* $U(2^n)$.

Definition 3. *An* ***encoding gate*** E_S *for* $S \in \mathcal{P}_n$ *is* $U \in U(2^{n+1})$ *given by* $(\mathbb{I}_n \otimes H)\, CS\, (\mathbb{I}_n \otimes H)$.

And the operator itself can be written as

$$E_S = \frac{\mathbb{I}_n + S}{2} \otimes \mathbb{I} + \frac{\mathbb{I}_n - S}{2} \otimes \sigma_1$$

It is well known that $\mathcal{C}_n$ is generated by Hadamard, phase, and CNOT gates [6]. Since all the stabilizers are in the Pauli group, CS can always be made out of CNOT and Hadamard gates and so $E_S \in \mathcal{C}_{n+1}$. Furthermore E_S are Hermitian as well so $E_S = E_S^{-1}$. In general, encoding gates produce entangled states, projecting some n-qubit state $|\psi\rangle$ onto the ± 1 eigenvectors of S tensored together with $|0\rangle, |1\rangle$ respectively. We will be interested in the action of these gates for storing syndrome information in stabilizer codes, which require $|\psi\rangle$ to be in a stabilizer state.

Definition 4. *Let* $G \subset \mathcal{P}_n$ *and consider the vector space* V_G *as the set of n-qubit states that are fixed by every element of* G. V_G *is the* ***vector space stabilized by G*** *and* G *is the* ***stabilizer*** *of* V_G.

We aim to show the following.

Proposition 1. *Let* V_G *be a non-trivial vector space stabilized by* $G \subset \mathcal{P}_n$ *and* $|\psi\rangle \in V_G$. *Then if* $U = U_1 \ldots U_t$ *where each* $U_i \in U(2^{n+m})$ *is either an encoding gate for elements of the stabilizer or a multiqubit Pauli gate, then* $U\left(|\psi\rangle \otimes |0\rangle^{\otimes m}\right)$ *is separable.*

Proof

Every U_i is either an encoding gate or it is in $\mathcal{P}_{n+m}$. Find the largest $j \leq t$ such that U_j is an encoding gate and U_{j+1} is not. Then $U_j U_{j+1} = \widetilde{U}_{j+1} U_j$ where $\widetilde{U}_{j+1} \in \mathcal{P}_{n+m}$ since

$U_j \in \mathcal{C}_{n+m}$. Do this for all encoding gates in $U_1 \dots U_t$ in order of decreasing index until they are all arranged on the right hand side of the product. What we will be left with is, up to reindexing, $U = \widetilde{U}_1 \dots \widetilde{U}_k U_{k+1} \dots U_t$ where $U_{k+1}, \dots, U_t$ are all encoding gates and the rest are in $\mathcal{P}_{n+m}$.

$$U\left(|\psi\rangle \otimes |0\rangle^{\otimes m}\right) = \widetilde{U}_1 \dots \widetilde{U}_k U_{k+1} \dots U_t \left(|\psi\rangle \otimes |0\rangle^{\otimes m}\right) = \widetilde{U}_1 \dots \widetilde{U}_k \left(|\psi\rangle \otimes |0\rangle^{\otimes m}\right) = U'\left(|\psi\rangle \otimes |0\rangle^{\otimes m}\right)$$

By virtue of the group product, $U' \in \mathcal{P}_{n+m}$, so we can write it as an $(n+m)$-fold tensor product of $\{I, \sigma_1, \sigma_2, \sigma_3\}$. To make the separability of this state explicit,we group these terms into those that act on the data and ancilla $U' = U'_D \otimes U'_A$ so that

$$U\left(|\psi\rangle \otimes |0\rangle^{\otimes m}\right) = U'_D |\psi\rangle \otimes U'_A |0\rangle^{\otimes m}.$$

This is manifestly the product of a data and an ancilla state.

This demonstrates that the data and the ancilla are not entangled after syndrome extraction with Pauli errors. Furthermore, since Pauli gates send computational basis states to one another, we can be sure that the ancilla state will be unchanged under measurements done in this basis.

In coherent error correction $C_k NOT$ gates perform corrections in the data conditioned on the state of the ancilla. The system, immediately before the correction phase, will always be a product of a single computational basis state and the possibly entangled data state. Thus, doing ancilla qubit measurements in this basis to determine whether or not to apply the error-correcting gate accurately reproduces the unitary, non-Clifford dynamics of the circuit under a discrete Pauli error model. We point out that this still gives a faithful representation of the effects of continuous, uncorrelated errors by linearity.

2-Designs and Redundant Syndrome Extraction

0.20 Introduction

A working quantum computer must be fault-tolerant: the reliability of all components must be considered, and appropriate measures taken for compensation of malfunctions [78, 79]. Error correction forms the core of this process. Error syndromes are extracted and used to generate the information needed to set the computer back on the right path. The syndrome information may itself contain errors because of imperfect measurements. This aspect of fault tolerance was recognized at an early stage of the development of the theory. In the two most prominent syndrome extraction protocols, the remedy was to repeat measurements already made [80, 81], thereby building in redundancy. This is a straightforward way to make the syndrome information more reliable.

In the last few years, more sophisticated schemes have been proposed. Fujiwara *et al.* noted that measuring more than a minimal set of stabilizers could be a more efficient way to extract reliable information and noted a possible connection to designs [82, 83]. Ashikmin *et al.* generalized existence theorems and the quantum Singleton bound of standard quantum error correction (QEC) theory so that they take into account redundancy in measurements [84]. Crow *et al.* used redundancy in syndrome extraction to give thresholds for qubit performance in a coherent error-correction scheme [75].

In this chapter, we show how to optimize measurement redundancy by applying the theory of 2-designs [1]. This is called design-based redundancy (DBR). 2-designs have long been used

[1] 2-designs are also known as balanced incomplete block designs. Our sense of the word 2-design is not

in classical error correction [85]. We investigate both a minimal redundant extraction scheme (MR) as well as the more comprehensive DBR.

It is sufficient to use a simple model for the faults. The key feature of this model is to separately define the qubit error probability p_q and the syndrome measurement error probability p_m. Different physical implementations of quantum computation will have very different values of the ratio p_q/p_m and this will strongly influence the optimal DBR protocol. In this work we will only consider the simple situation of a quantum memory that is periodically refreshed by error correction; more complicated scenarios with active gates would complicate the analysis but not introduce significant new concepts. The discussion is restricted to stabilizer codes [86]. It may be possible to use 2-designs to improve other codes, but it appears to be more complicated. We stress that DBR is equally applicable to measurement-based error correction and coherent error correction. For definiteness, we will use the language of measurement-based QEC in this work.

0.21 Bit Flip Code

This section is included in order to introduce the basic ideas of DBR. It treats the elementary example of the 3-qubit bit flip code [77]. The three physical qubits store a single bit of quantum information and there is a probability p_q of a bit flipping. No other qubit errors are allowed. Stabilizers $S_1 = Z_1Z_2$, $S_2 = Z_2Z_3$ and $S_3 = Z_3Z_1$ can each be measured, always yielding ± 1. An incorrect measurement result is obtained with probability p_m. The starting state (chosen arbitrarily in the code subspace) is $|000\rangle$; after a certain time 1 or more bits may flip and we measure a set of stabilizers, perhaps repeatedly. We define an event e to be the final state of the qubits together with the measurement results. Each event e has a probability $P(e)$ with $0 \leq P(e) \leq 1$ and a success factor $s(e) = 0$ or $s(e) = 1$ when the event is respectively uncorrectable or correctable. For example, if the textbook procedure of measuring only the generators of the stabilizer group S_1 and S_2 is used, a possible event is $e_0 = \{|001\rangle, +1, -1\}$. This can be made fault-tolerant by repeating the measurements and using majority rules on the measurement results. Assuming independence, the probability

related to quantum 2-designs, which are probability distributions over quantum states.

Protocol	Failure Rate	Cost
Minimal QEC	$2p_m - p_m^2 + 3p_q^2$	2
Fault-tolerant QEC	$6p_m^2 + 3p_q^2$	$4 + 2p_m$
DBR	$3p_m^2 + 3p_q^2 + 9p_m p_q$	3

Table 2: Failure rate and cost for 3 error-correction protocols for the 3-qubit bit-flip code.

of this event is $P(e_0) = p_q(1-p_m)^2(1-p_q)^2$ since there is 1 qubit error and 0 measurement errors. $s(e_0) = 1$ since the information obtained from the measurements allows us to correct the error. The total failure probability of an error correction protocol, including possible DBR, is $F = 1 - \Sigma_e P(e)s(e)$. In addition, we define the cost C of a protocol to be the expected total number of stabilizer measurements in a correction cycle.

The DBR protocol differs from both the simple protocol and its fault-tolerant extension in that one measures *the complete set of stabilizer group generators* S_1, S_2 and S_3. This already builds in redundancy; if there is one measurement error then exactly one of the S_i is equal to -1. If 2 of the S_i is equal -1 then there is a unique instruction as to which bit to flip back. (Here and henceforth we use S_i both for the operators and for the result of measuring the operators.) The key point is that there is a unique signal even if there is a measurement error. For this toy code, MR and DBR are identical; for large codes this is not the case.

Once protocols are established, then it is straightforward to sum over the events and compute the failure rates and costs. In Table 2 we tabulate the results to quadratic order in p_q and p_m and the cost to linear order.

The fact that minimal QEC has a linear term in p_m is the signature that it is not fault-tolerant and is therefore not a candidate for a working computer. More importantly, the fault-tolerant version of conventional QEC is always more costly than DBR and the failure rate for conventional QEC exceeds that of DBR whenever $6p_m^2+3p_q^2 > 3p_m^2+3p_q^2+9p_m p_q$. This reduces to $p_m > p_q/3$, which is likely to happen in many implementations. It is interesting that DBR is superior even for $p_m = p_q$, a case often considered.

0.22 2-designs

The crucial feature of DBR for the bit flip code is that the syndrome possesses a unique signature when there is a measurement error. This feature can be generalized to more complex codes that can correct phase flip as well as bit flip errors. Consider an $[[n, k, d]]$ stabilizer code with n the number of physical qubits, k the number of logical qubits and d the distance; the code can correct errors on up to $(d-1)/2$ physical qubits. We will focus on $k = 1$ and the logical operators are $X_L = \otimes_{i=1}^{n} X_i$ and $Z_L = \otimes_{i=1}^{n} Z_i$, as in the Steane $[[7, 1, 3]]$ code. Our notation in this chapter extends the usual one slightly, since we wish also to detect up to s syndrome measurement errors - hence we refer to $[[n, k, d, s]]$ codes. Standard quantum error correction without repetitions has $s = 0$.

In DBR for a CSS (CSS-DBR) code we measure $m = C/2$ stabilizer operators of the form $S = X_{i_1} X_{i_2} \cdots X_{i_w}$ and $m = C/2$ stabilizer operators of the form $S = Z_{i_1} Z_{i_2} \cdots Z_{i_w}$. Each stabilizer has weight w. Here $\{i_1, i_2, ..., i_w\}$ are chosen from the set $\{1, 2, \ldots, n\}$, and any given S is completely defined by this choice. Thus for CSS codes X and Z errors are handled separately, so we simply use 2 copies of a single design, and this gives a particularly economical and effective DBR protocol. The measurement result of the Z-type stabilizers is different for any bit flip error. Tabulating these possible syndrome results yields an $m \times (n+1)$ matrix E whose entries are ± 1. The entry E_{ij} is the result of correctly extracting the value of S_i for a bit flip on the j-th physical qubit. At a minimum, the rows of E must all be distinct in order to diagnose an error uniquely. We wish to go beyond this. *Fault tolerance in DBR is achieved not by repetition but by choosing our measurements so that the results differ by as much as possible.* This motivates the use of 2-designs for our choice of measurements.

A 2-design is a family of subsets of a larger set. This family must fulfill certain conditions. For present purposes there is a set of n qubits and the indices on each Z-type stabilizer to be measured defines a subset of the qubit indices. Thus the family of subsets is determined by the choice of Z-type stabilizers. There are m subsets. The conditions for this choice to be a 2-design are: (1) each subset has the same size w; (2) every index must appear in exactly ρ subsets; (3) every pair of indices appears in exactly λ subsets. The parameters are not all independent. They satisfy the basic 2-design relations $mw = n\rho$ and $\lambda(n-1) = \rho(w-1)$.

These equations are proved using counting arguments.

Let us define the Hamming-like distance D between any two Z-type stabilizers S_i and $S_{i'}$ as $D(S_i, S_{i'}) = \Sigma_{j=1}^{r} |E_{ij} - E_{i'j}|$, where E_{ij} is the result when the jth qubit has flipped. Then if the choice of the S_i is a 2-design we have that $D(S, S') = 2(\rho - \lambda)$ for all S and S'. This may be shown by arguments similar to those in [85]. This the key feature of 2-designs for error correction purposes: it enables us to systematically maximize $\rho - \lambda$.

To illustrate the definition we give the example of a simple 2-design known as the order-2 biplane. It applies to a system of $n = 7$ qubits. The stabilizers are $S_1 = Z_1 Z_5 Z_6 Z_7$, $S_2 = Z_2 Z_4 Z_6 Z_7$, $S_3 = Z_3 Z_4 Z_5 Z_7$, $S_4 = Z_1 Z_2 Z_4 Z_5$, $S_5 = Z_1 Z_3 Z_4 Z_6$, $S_6 = Z_2 Z_3 Z_5 Z_6$, $S_7 = Z_1 Z_2 Z_3 Z_7$. It is not hard to verify that this choice satisfies the constraints for a 2-design with $w = 4$, $m = 7$, $\rho = 4$ and $\lambda = 2$. We will use this 2-design below.

The fundamental criterion for the choice of stabilizers is the minimization of the failure rate F and the cost C. We have seen that the natural arena for this is the 2-design. However, not all 2-designs can be used in conjunction with stabilizer quantum error correction. There is one constraint for all DBR schemes based on 2-designs.

Constraint 1. The definition of a stabilizer requires that it must commute with the logical operators, *i.e.*, $[S, \otimes_{i=1}^{n} X_i] = [S, \otimes_{i=1}^{n} Z_i] = 0$ for all S. A short calculation shows that this is true if and only if w is even.

Proof of constraint 1 We must show that all the measured stabilizers S commute with all the logical operators L if and only if w is even. An example of such a commutator is

$$[S, L] = [Z_{i_1} Z_{i_2} ... Z_{i_w}, X_1 X_2 ... X_n],$$

where $\{i_1, i_2, ...i_w\} \subset \{1, 2, ..., n\}$. We then define the set of indices $\{k_1, k_2 ... k_{(n-w)}\}$ such

that $\{i_1, i_2, ...i_w\} \cup \{j_1, j_2...j_{(n-w)}\} = \{1, 2...n\}$ This can be simplified as follows:

$$\begin{aligned}
[S, L] &= [Z_{i_1} Z_{i_2} ... Z_{i_w}, X_1 X_2 ... X_n] \\
&= X_{k_1} X_{k_2} ... X_{k_{(n-w)}} [Z_{i_1} Z_{i_2} ... Z_{i_w}, X_{i_1} X_{i_2} ... X_{i_w}] \\
&= X_{k_1} X_{k_2} ... X_{k_{(n-w)}} \times \\
&\quad (Z_{i_1} Z_{i_2} ... Z_{i_w} X_{i_1} X_{i_2} ... X_{i_w} - X_{i_1} X_{i_2} ... X_{i_w} Z_{i_1} Z_{i_2} ... Z_{i_w}) \\
&= X_{k_1} X_{k_2} ... X_{k_{(n-w)}} \times \\
&\quad (Z_{i_1} X_{i_1} Z_{i_2} X_{i_2} ... Z_{i_w} X_{i_w} - X_{i_1} Z_{i_1} X_{i_2} Z_{i_2} ... X_{i_w} Z_{i_w}) \\
&= X_{k_1} X_{k_2} ... X_{k_{(n-w)}} \times \\
&\quad ((-1)^w X_{i_1} Z_{i_1} X_{i_2} Z_{i_2} ... X_{i_w} Z_{i_w} - X_{i_1} Z_{i_1} X_{i_2} Z_{i_2} ... X_{i_w} Z_{i_w}) \\
&= X_{k_1} X_{k_2} ... X_{k_{(n-w)}} [(-1)^w - 1] X_{i_1} Z_{i_1} X_{i_2} Z_{i_2} ... X_{i_w} Z_{i_w},
\end{aligned}$$

which is zero if and only if w is even. This proof clearly holds for all stabilizer/logical operator pairs.

Constraint 2. (CSS-DBR only.) The use of two copies of a design generates an additional constraint. The stabilizer group is commutative. All X-type stabilizers trivially commute with each other; the same is true for the Z-type stabilizers. An X-type stabilizer commutes with a Z-type stabilizer if and only if the intersection of the set of indices of the X-type stabilizer with the set of indices of the Z-type stabilizer has even cardinality. This happens for all such pairs of stabilizers if and only if λ is even.

These two constraints rule out a majority of 2-designs for CSS-DBR. The order-2 biplane with $w = 4$ and $\lambda = 2$ is allowed, but the natural successor is the order-3 biplane with $w = 5$: it cannot serve as the basis for an DBR scheme.

Proof of constraint 2 For the CSS-DBR codes, the same design is used twice, once for the X-stabilizers and once for the Z-stabilizers. The full group must be abelian, so one must check that the X-stabilizers commute with the Z-stabilizers. The relevant commutators have the form

$$C = [X_{i_1} X_{i_2} ... X_{i_w}, Z_{j_1} Z_{j_2} ... Z_{j_w}]$$

Here $\{i_1, i_2, ...i_w\} \subset \{1, 2, ..., n\}$. and $\{j_1, j_2, ...j_w\} \subset \{1, 2, ..., n\}$. Inspection of the proof for

constraint 1 then indicates that if we define

$$x = |\{i_1, i_2, ...i_w\} \cap \{j_1, j_2, ...j_w\}|,$$

then $C = 0$ if and only if x is even. This is true for all choices of the index sets if λ is even.

0.23 Results

5-qubit code

The [[5,1,3]] perfect code is not a CSS code, so a single 2-design is used for all errors. We take the stabilizer group generated by $S_1 = X_1Z_2Z_3X_4, S_2 = X_2Z_3Z_4X_5, S_3 = X_1X_3Z_4Z_5$, and $S_4 = Z_1X_2X_4Z_5$, which is then a [[5,1,3,1]] code. The full stabilizer group is an instance of the class of designs generated from Hadamard matrices, appropriately called Hadamard designs. In particular, the design here is the complement to the $n = 3$ Hadamard design [87]. Once the stabilizer set is chosen we can compute the failure rate F_{DBR} as a function of p_m and p_q. DBR stands for "design-based redundancy". We also compute the failure rate F_{MR} for a scheme in which minimal redundancy (MR) is employed: only one additional stabilizer is measured, namely $S_1S_2S_3S_4$. This operator is the product of the minimal set of generators. With this choice the resulting protocol is somewhat analogous to a single parity check in classical error correction. Finally we compute the failure rate F_{QEC} for fault-tolerant QEC. Analytical results for all three rates are given in the supplementary material. Choosing F_{QEC} as a basline, we plot the relative failure rates in Fig. 1 for a range of error probabilities relevant to near-term quantum information processing. Note that MR has an advantage over QEC for $p_m > XXXp_q$. Both are fault-tolerant with respect to p_m in that $F_{QEC}.F_{MR} \sim p_m^2$. However, DBR is superior to both QEC and MR for all p_m, p_q in the appropriate regime. This can be traced back to the fact that $F_{DBR} \sim p_m^4$. Note that MR is cheaper than DBR in terms of number of measurements, so it may be preferable in intermediate regimes of p_m.

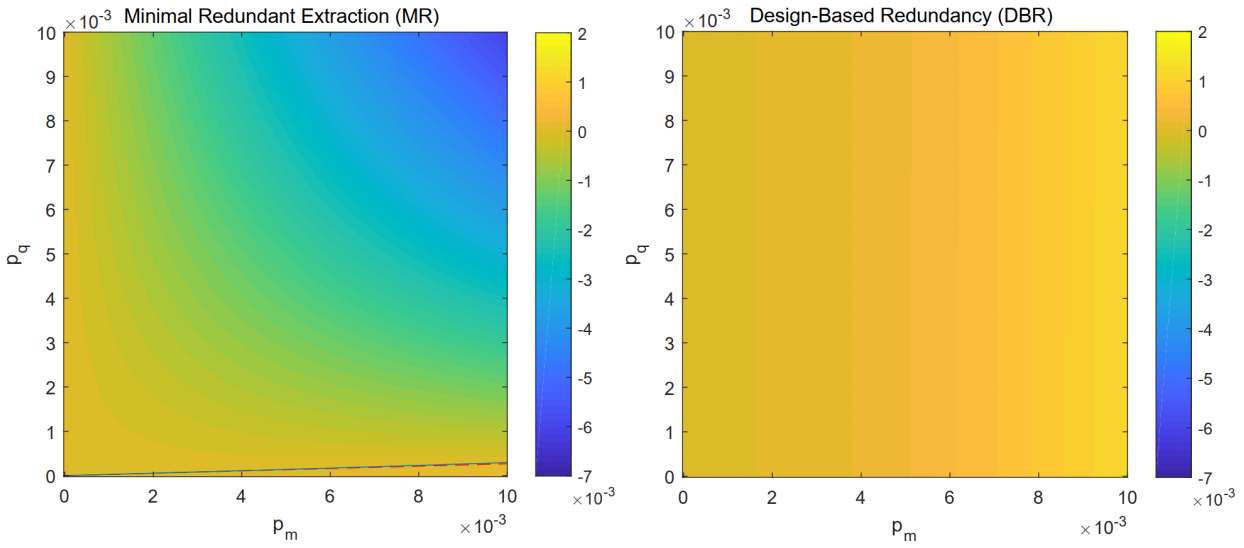

Figure 22: $F_{QEC} - F_{MR}$ and $F_{QEC} - F_{DBR}$ for the [[5,1,3]] Perfect code. The left plot shows a curve dividing the parameter space into configurations where QEC outperforms MR, whereas at all physical error rates DBR beats QEC. This comes at the cost of more stabilizer measurements.

Steane code

In our notation, the Steane code with the minimal set of measurements is a $[[7, 1, 3, 0]]$ code. When syndrome measurements errors occur, it is not fault-tolerant. 3-fold repetition of its measurement sequence with majority rules gives a $[[7, 1, 3, 1]]$ code. The order-2 biplane DBR procedure utilizes 14 stabilizers: those given in the previous section and another 7 with $Z_i \to X_i$. It is a fault tolerant $[[7, 1, 3, 1]]$ code. We again give the comparison of

Protocol	Failure Rate	Cost
Minimal QEC	$3p_m - 3p_m^2 + 21p_q^2$	3
Fault-tolerant QEC	$9p_m^2 + 21p_q^2$	$6 + 3p_m$
MR with S_7	$6p_m^2 + 21p_q^2 + 28p_m p_q$	4
DBR	$21p_q^2$	7

Table 3: Failure rate and cost for 4 error-correction protocols for the Steane [[7,1,3]] and [[7,1,3,1]] codes.

failure rates for 3 protocols: the repeated Steane code, denoted QEC; an MR code with two additional stabilizers, one of the X type and one of the Z type, in both cases a product of the usual generators; and the MR approach measuring the full stabilizer group. This final

set of stabilizers corresponds to 2 copies of the order-2 biplane. The results demonstrate that DBR has a distinct advantage over the other 2 protocols. It is even more dramatic than in the 5-qubit case. This combination of DBR with a CSS code is particularly effective in repairing measurement errors. Again, the MR approach may also be useful in practical cases - everything depends on the cost and reliability of measurements in a specific implementation.

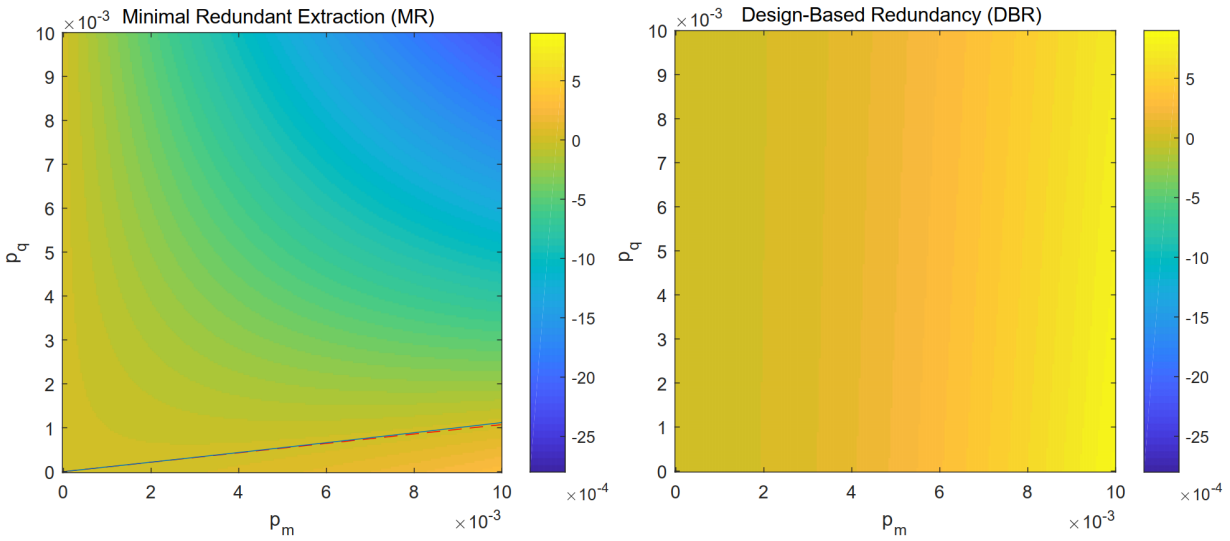

Figure 23: $F_{QEC} - F_{MR}$ and $F_{QEC} - F_{DBR}$ for the [[7,1,3]] Steane code. The left plot shows a curve dividing the parameter space into configurations where QEC outperforms MR, whereas at all physical error rates DBR beats QEC. This comes at the cost of more stabilizer measurements.

0.24 Discussion

We have focused on 2-designs that appear naturally in straightforward modifications of well-known codes. But a longer-term goal would be to use known 2-designs to improve syndrome extraction, thus improving quantum error-correction in cases where errors in the measurement process are important. This not straightforward, since there is no general classification theorem for 2-designs, though a large number of special cases and some infinite families are known [88]. This is a promising line of research.

Once a quantum processor is characterized and p_q, p_m are known, we can look at the failure rates to determine which approach to take. The next consideration is cost. In a Shor-

style extraction protocol each stabilizer measurement requires a number of ancilla qubits one greater than the weight of the operator itself [78]. In fault-tolerant QEC ancilla qubits can be reused on subsequent cycles of syndrome extraction. Thus, even though the number of QEC measurements may exceed that of DBR for a given code, the size of the quantum register required may in fact be larger for DBR. Recent ideas for using fewer ancilla qubits could be used to bring down the potential cost disparity between QEC and DBR [89]. This comes at the price of adding more gates, so an appraisal of which is the most fruitful approach involves a balancing act between number of qubits and circuit depth.

Conclusion

In this dissertation we have handled several topics with the aim of better understanding decoherence in quantum computers and developing strategies to mitigate the effects of these mechanisms on information processing tasks. Evanescent-wave Johnson noise can be the dominant noise source for spin qubits in strong magnetic fields, one of the eminent architectures for semiconductor quantum computing. We demonstrated the effects of this noise by developing a classical analogy to simplify the calculation of thermal field Green's functions and using the resulting analytic descriptions of the fields in conjunction with a multipole formulation of qubit dynamics.

Next, we constructed a general protocol for measuring the pairwise correlations between qubits in a quantum computer. We focused on this application in a specific semiconductor device, but the method generalizes a standard spectroscopy technique and therefore implementing it in other qubit implementations is a promising path for future research. New metrics for characterizing proposed circuits for a quantum information processing tasks are provided and justified by comparing them to full simulations of the fidelity under a given noise model. We finally generalized this to systems of many qubits circumventing the exponential scaling of unitary dynamics.

Towards quantum error correction, we proposed a refined set of criteria for implementing known quantum codes without the requirement of ancilla measurements. This relies on the classical simulation of quantum codes via the Gottesman-Knill theorem with a new extention to include non-Clifford gates under particular circumstances. Namely, the separability of the ancilla and data qubit registers. We proved that this can be achieved by insisting that the encoding of stabilizer eigenvalues in ancilla qubits be done in a single time step, which has been demonstrated in neutral atom qubit implementations.

We then explored the role of redundancy in stabilizer codes. The traditional approach ensures a threshold by utilizing a majority rules strategy when taking stabilizer measurements, but another method referred to as redundant syndrome extraction uses the group structure of the code to make the process fault-tolerant using potentially fewer total measurements. We gave guidelines for selecting one of these strategies once the decoherence and measurement fallibility of a quantum computer are known.

In the near term, we may expect the development of machines with 50-100 fairly noisy qubits and gates (the "NISQ" era). One important goal for this era is the development of a single fault-tolerant error-corrected logical qubit. The correction process involves multiple gates while the data qubits will often have reasonably long coherence times. In this situation, probably the most common one, we expect $p_m > p_q$. This means that the strategies outlined in Chapters 3 and 4 will be very relevant for this important goal.

Bibliography

[1] Richard P. Feynman. Simulating physics with computers. *International Journal of Theoretical Physics*, 21, 06 1982.

[2] Floris A. Zwanenburg, Andrew S. Dzurak, Andrea Morello, Michelle Y. Simmons, Lloyd C. L. Hollenberg, Gerhard Klimeck, Sven Rogge, Susan N. Coppersmith, and Mark A. Eriksson. Silicon quantum electronics. *Rev. Mod. Phys.*, 85:961–1019, Jul 2013.

[3] G Wendin. Quantum information processing with superconducting circuits: a review. *Reports on Progress in Physics*, 80(10):106001, sep 2017.

[4] D. Aharonov and M. Ben-Or. Fault-tolerant quantum computation with constant error. In *Proceedings of the Twenty-ninth Annual ACM Symposium on Theory of Computing*, STOC '97, pages 176–188, New York, NY, USA, 1997. ACM.

[5] Dorit Aharonov, Alexei Kitaev, and John Preskill. Fault-tolerant quantum computation with long-range correlated noise. *Phys. Rev. Lett.*, 96:050504, Feb 2006.

[6] Daniel Gottesman. Stabilizer codes and quantum error correction. 1997.

[7] J. B. Johnson. Thermal agitation of electricity in conductors. *Phys. Rev.*, 32:97–109, Jul 1928.

[8] H. Nyquist. Thermal agitation of electric charge in conductors. *Phys. Rev.*, 32:110–113, Jul 1928.

[9] Herbert B. Callen and Theodore A. Welton. Irreversibility and generalized noise. *Phys. Rev.*, 83:34–40, Jul 1951.

[10] R. Kubo. The fluctuation-dissipation theorem. *Reports on Progress in Physics*, 29(1):255, 1966.

[11] E.M. Lifshitz. The theory of molecular attractive forces between solids. *Sov. Phys. JETP*, 2:73, 1956.

[12] S. M. Rytov. *Theory of Electrical Fluctuation and Thermal Radiation.* Publishing House, 1953.

[13] S. M. Rytov, I.U.A. Kravtsov, and V.I. Tatarski. *Principles of Statistical Radiophysics*, volume 3. Springer-Verlag, 1989.

[14] G. S. Agarwal. Quantum electrodynamics in the presence of dielectrics and conductors. i. electromagnetic-field response functions and black-body fluctuations in finite geometries. *Phys. Rev. A*, 11:230–242, Jan 1975.

[15] H. B. G. Casimir. On the Attraction Between Two Perfectly Conducting Plates. *Indag. Math.*, 10:261–263, 1948. [Kon. Ned. Akad. Wetensch. Proc.100N3-4,61(1997)].

[16] E. M. Lifshitz and L.P. Pitaevskii. *Statistical Physics*, volume 9 of *Part 2.* Pergamon, 1980.

[17] A. I. Volokitin and B. N. J. Persson. Near-field radiative heat transfer and noncontact friction. *Rev. Mod. Phys.*, 79:1291–1329, Oct 2007.

[18] J.B. Pendry. Radiative exchange of heat between nanostructures. *J. Phys.: Condensed Matter*, 11:6621–6633, 1999.

[19] R. Neumann and L. R. Schreiber. Simulation of micro-magnet stray-field dynamics for spin qubit manipulation. *Journal of Applied Physics*, 117(19), 2015.

[20] A. Kha, R. Joynt, and D. Culcer. Do micromagnets expose spin qubits to charge and johnson noise? *Applied Physics Letters*, 107(17), 2015.

[21] C. Henkel, S. Pötting, and M. Wilkens. Loss and heating of particles in small and noisy traps. *Applied Physics B*, 69(5):379–387, 1999.

[22] C. Henkel and M. Wilkens. Heating of trapped atoms near thermal surfaces. *Europhys. Lett.*, 47(4):414–420, 1999.

[23] D. M. Harber, J. M. McGuirk, J. M. Obrecht, and E. A. Cornell. Thermally induced losses in ultra-cold atoms magnetically trapped near room-temperature surfaces. *Journal of Low Temperature Physics*, 133(3):229–238, 2003.

[24] J. A. Sidles, J. L. Garbini, W. M. Dougherty, and Shih-Hui Chao. The classical and quantum theory of thermal magnetic noise, with applications in spintronics and quantum microscopy. *Proceedings of the IEEE*, 91(5):799–816, May 2003.

[25] D.V. Averin. Adiabatic quantum computation with cooper pairs. *Solid State Communications*, 105(10):659 – 664, 1998.

[26] Y. Makhlin, G. Schön, and A. Shnirman. Quantum-state engineering with josephson-junction devices. *Rev. Mod. Phys.*, 73:357–400, May 2001.

[27] M. I. Dykman, P. M. Platzman, and P. Seddighrad. Qubits with electrons on liquid helium. *Phys. Rev. B*, 67:155402, Apr 2003.

[28] Peihao Huang and Xuedong Hu. Electron spin relaxation due to charge noise. *Phys. Rev. B*, 89:195302, May 2014.

[29] A. Poudel, L. S. Langsjoen, M. G. Vavilov, and R. Joynt. Relaxation in quantum dots due to evanescent-wave johnson noise. *Phys. Rev. B*, 87:045301, Jan 2013.

[30] L. S. Langsjoen, A. Poudel, M. G. Vavilov, and R. Joynt. Qubit relaxation from evanescent-wave johnson noise. *Phys. Rev. A*, 86:010301, Jul 2012.

[31] S. Kolkowitz, A. Safira, A. A. High, R. C. Devlin, S. Choi, Q. P. Unterreithmeier, D. Patterson, A. S. Zibrov, V. E. Manucharyan, H. Park, and M. D. Lukin. Probing johnson noise and ballistic transport in normal metals with a single-spin qubit. *Science*, 347(6226):1129–1132, 2015.

[32] T. Hayashi, T. Fujisawa, H. D. Cheong, Y. H. Jeong, and Y. Hirayama. Coherent manipulation of electronic states in a double quantum dot. *Phys. Rev. Lett.*, 91:226804, Nov 2003.

[33] T. Fujisawa, T. Hayashi, H.D. Cheong, Y.H. Jeong, and Y. Hirayama. Rotation and phase-shift operations for a charge qubit in a double quantum dot. *Physica E: Low-dimensional Systems and Nanostructures*, 21(2–4):1046 – 1052, 2004. Proceedings of the Eleventh International Conference on Modulated Semiconductor Structures.

[34] J. R. Petta, A. C. Johnson, C. M. Marcus, M. P. Hanson, and A. C. Gossard. Manipulation of a single charge in a double quantum dot. *Phys. Rev. Lett.*, 93:186802, Oct 2004.

[35] J. Gorman, D. G. Hasko, and D. A. Williams. Charge-qubit operation of an isolated double quantum dot. *Phys. Rev. Lett.*, 95:090502, Aug 2005.

[36] D. C. B. Valente, E. R. Mucciolo, and F. K. Wilhelm. Decoherence by electromagnetic fluctuations in double-quantum-dot charge qubits. *Phys. Rev. B*, 82:125302, Sep 2010.

[37] L. S. Langsjoen, A. Poudel, M. G. Vavilov, and R. Joynt. Electromagnetic fluctuations near thin metallic films. *Phys. Rev. B*, 89:115401, Mar 2014.

[38] R.E. Raab and O.L. De Lange. *Multipole Theory in Electromagnetism.* Oxford Science Publications, 2005.

[39] Jonas Bylander, Simon Gustavsson, Fei Yan, Fumiki Yoshihara, Khalil Harrabi, George Fitch, David G. Cory, Yasunobu Nakamura, Jaw-Shen Tsai, and William D. Oliver. Noise spectroscopy through dynamical decoupling with a superconducting flux qubit. *Nat Phys*, 7(7):565–570, Jul 2011.

[40] O. E. Dial, M. D. Shulman, S. P. Harvey, H. Bluhm, V. Umansky, and A. Yacoby. Charge noise spectroscopy using coherent exchange oscillations in a singlet-triplet qubit. *Phys. Rev. Lett.*, 110:146804, Apr 2013.

[41] Juha T. Muhonen, Juan P. Dehollain, Arne Laucht, Fay E. Hudson, Rachpon Kalra, Takeharu Sekiguchi, Kohei M. Itoh, David N. Jamieson, Jeffrey C. McCallum, Andrew S. Dzurak, and Andrea Morello. Storing quantum information for 30 seconds in a nanoelectronic device. *Nat Nano*, 9(12):986–991, Dec 2014. Letter.

[42] M. L. Levin and S.M. Rytov. *Theory of Equilibrium Thermal Fluctuations in Electrodynamics*. Nauka, Moskow, 1967. (In Russian). We understand that this subject is also treated here. However, we were not able to obtain a copy of this book.

[43] K. Joulain, J.P. Mulet, F. Marquier, R. Carminati, and J.J. Greffet. Surface electromagnetic waves thermally excited: Radiative heat transfer, coherence properties and casimir forces revisited in the near field. *Surface Science Reports*, 57:59–112, 2005.

[44] L.D. Landau and E. M. Lifshitz. *Electrodynamics of Continuous Media*, volume 8. Pergamon, 1980.

[45] J. A. Osborn. Demagnetizing factors of the general ellipsoid. *Phys. Rev.*, 67:351–357, Jun 1945.

[46] A. Garg. Conductors in quasistatic electric fields. *American Journal of Physics*, 76(7), 2008.

[47] A. Garg. *Classical Electromagnetism in a Nutshell*. Princeton University Press, 2012.

[48] M. Xiao, M. G. House, and H. W. Jiang. Measurement of the spin relaxation time of single electrons in a silicon metal-oxide-semiconductor-based quantum dot. *Phys. Rev. Lett.*, 104:096801, Mar 2010.

[49] L. H. Willems van Beveren B. Witkamp L. M. K. Vandersypen J. M. Elzerman, R. Hanson and L. P. Kouwenhoven. Single-shot read-out of an individual electron spin in a quantum dot. *Nature*, 430:431–435, 2004.

[50] S. Amasha, K. MacLean, Iuliana P. Radu, D. M. Zumbühl, M. A. Kastner, M. P. Hanson, and A. C. Gossard. Electrical control of spin relaxation in a quantum dot. *Phys. Rev. Lett.*, 100:046803, Jan 2008.

[51] Susan J. Angus, Andrew J. Ferguson, Andrew S. Dzurak, and Robert G. Clark. Gate-defined quantum dots in intrinsic silicon. *Nano Letters*, 7(7):2051–2055, 2007. PMID: 17567176.

[52] J.C.C. Hwang, C.H. Yang, M. Veldhorst, N. Hendrickx, M.A. Fogarty, W. Huang, F.E. Hudson, A. Morello, and A.S. Dzurak. Impact of g-factors and valleys on spin qubits in a silicon double quantum dot. *ArXiv e-prints*, 2016.

[53] Ron Folman, Peter Krüger, Donatella Cassettari, Björn Hessmo, Thomas Maier, and Jörg Schmiedmayer. Controlling cold atoms using nanofabricated surfaces: Atom chips. *Phys. Rev. Lett.*, 84:4749–4752, May 2000.

[54] M. A. Cirone, A. Negretti, T. Calarco, P. Krüger, and J. Schmiedmayer. A simple quantum gate with atom chips. *The European Physical Journal D - Atomic, Molecular, Optical and Plasma Physics*, 35(1):165–171, 2005.

[55] John Preskill. Sufficient condition on noise correlations for scalable quantum computing. *Quantum Info. Comput.*, 13(3-4):181–194, March 2013.

[56] John Preskill. *Fault-Tolerant Quantum Computation*, pages 213–269. World Scientific, 1998.

[57] Héctor Bombín. Resilience to time-correlated noise in quantum computation. *Phys. Rev. X*, 6:041034, Nov 2016.

[58] D. A. Lidar, I. L. Chuang, and K. B. Whaley. Decoherence-free subspaces for quantum computation. *Phys. Rev. Lett.*, 81:2594–2597, Sep 1998.

[59] Lu-Ming Duan and Guang-Can Guo. Reducing decoherence in quantum-computer memory with all quantum bits coupling to the same environment. *Phys. Rev. A*, 57:737–741, Feb 1998.

[60] Daniel A. Lidar, Dave Bacon, Julia Kempe, and K. B. Whaley. Decoherence-free subspaces for multiple-qubit errors. i. characterization. *Phys. Rev. A*, 63:022306, Jan 2001.

[61] Daniel A. Lidar, Dave Bacon, Julia Kempe, and K. B. Whaley. Decoherence-free subspaces for multiple-qubit errors. ii. universal, fault-tolerant quantum computation. *Phys. Rev. A*, 63:022307, Jan 2001.

[62] Kristan Temme, Sergey Bravyi, and Jay M. Gambetta. Error mitigation for short-depth quantum circuits. *Phys. Rev. Lett.*, 119:180509, Nov 2017.

[63] T. F. Watson, S. G. J. Philips, E. Kawakami, D. R. Ward, P. Scarlino, M. Veldhorst, D. E. Savage, M. G. Lagally, Mark Friesen, S. N. Coppersmith, M. A. Eriksson, and L. M. K. Vandersypen. A programmable two-qubit quantum processor in silicon. *Nature*, 555:633 EP –, Feb 2018.

[64] Mark Friesen, Joydip Ghosh, M. A. Eriksson, and S. N. Coppersmith. A decoherence-free subspace in a charge quadrupole qubit. *Nature Communications*, 8:15923 EP –, Jun 2017. Article.

[65] Michael J. Biercuk, Hermann Uys, Aaron P. VanDevender, Nobuyasu Shiga, Wayne M. Itano, and John J. Bollinger. Optimized dynamical decoupling in a model quantum memory. *Nature*, 458:996 EP –, Apr 2009.

[66] Gonzalo A. Álvarez and Dieter Suter. Measuring the spectrum of colored noise by dynamical decoupling. *Phys. Rev. Lett.*, 107:230501, Nov 2011.

[67] Tatsuro Yuge, Susumu Sasaki, and Yoshiro Hirayama. Measurement of the noise spectrum using a multiple-pulse sequence. *Phys. Rev. Lett.*, 107:170504, Oct 2011.

[68] Piotr Szańkowski, Marek Trippenbach, and Łukasz Cywiński. Spectroscopy of cross correlations of environmental noises with two qubits. *Phys. Rev. A*, 94:012109, Jul 2016.

[69] Gerardo A. Paz-Silva, Leigh M. Norris, and Lorenza Viola. Multiqubit spectroscopy of gaussian quantum noise. *Phys. Rev. A*, 95:022121, Feb 2017.

[70] Jan Krzywda, Piotr Szańkowski, and Łukasz Cywiński. The dynamical-decoupling-based spatiotemporal noise spectroscopy. *arXiv e-prints*, page arXiv:1809.02972, September 2018.

[71] Charles P. Slichter. *Principles of magnetic resonance*. Springer, 3rd edition, 2010.

[72] Jun Yoneda, Kenta Takeda, Tomohiro Otsuka, Takashi Nakajima, Matthieu R. Delbecq, Giles Allison, Takumu Honda, Tetsuo Kodera, Shunri Oda, Yusuke Hoshi, Noritaka Usami, Kohei M. Itoh, and Seigo Tarucha. A quantum-dot spin qubit with coherence limited by charge noise and fidelity higher than 99.9%. *Nature Nanotechnology*, 13(2):102–106, 2018.

[73] J. R. Petta, A. C. Johnson, J. M. Taylor, E. A. Laird, A. Yacoby, M. D. Lukin, C. M. Marcus, M. P. Hanson, and A. C. Gossard. Coherent manipulation of coupled electron spins in semiconductor quantum dots. *Science*, 309(5744):2180–2184, 2005.

[74] H. P. Breuer and F. Petruccione. *The theory of open quantum systems*. Oxford University Press, Great Clarendon Street, 2002.

[75] Daniel Crow, Robert Joynt, and M. Saffman. Improved error thresholds for measurement-free error correction. *Phys. Rev. Lett.*, 117:130503, Sep 2016.

[76] Scott Aaronson and Daniel Gottesman. Improved simulation of stabilizer circuits. *Phys. Rev. A*, 70:052328, Nov 2004.

[77] Michael A. Nielsen and Isaac L. Chuang. *Quantum Computation and Quantum Information: 10th Anniversary Edition*. Cambridge University Press, New York, NY, USA, 10th edition, 2011.

[78] P. W. Shor. Fault-tolerant quantum computation. In *Proceedings of 37th Conference on Foundations of Computer Science*, pages 56–65, Oct 1996.

[79] John Preskill. Fault-tolerant quantum computing. In Hoi-Kwong Lo, Tim Spiller, and Sandu Popescu, editors, *Introduction to Quantum Computation and Information*. World Scientific, 1999.

[80] A. M. Steane. Error correcting codes in quantum theory. *Phys. Rev. Lett.*, 77:793–797, Jul 1996.

[81] David P. DiVincenzo and Peter W. Shor. Fault-tolerant error correction with efficient quantum codes. *Phys. Rev. Lett.*, 77:3260–3263, Oct 1996.

[82] Yuichiro Fujiwara. Ability of stabilizer quantum error correction to protect itself from its own imperfection. *Phys. Rev. A*, 90:062304, Dec 2014.

[83] Y. Fujiwara, A. Gruner, and P. Vandendriessche. High-rate quantum low-density parity-check codes assisted by reliable qubits. *IEEE Transactions on Information Theory*, 61(4):1860–1878, April 2015.

[84] A. Ashikhmin, C. Lai, and T. A. Brun. Robust quantum error syndrome extraction by classical coding. In *2014 IEEE International Symposium on Information Theory*, pages 546–550, June 2014.

[85] Vera Pless. *Introduction to the Theory of Error-Correcting Codes*. Wiley-Interscience, New York, NY, USA, 3rd edition, 1982.

[86] Daniel Gottesman. Class of quantum error-correcting codes saturating the quantum hamming bound. *Phys. Rev. A*, 54:1862–1868, Sep 1996.

[87] J. H. Dinitz and D. R. Stinson. A brief introduction to design theory. In J. H. Dinitz and D. R. Stinson, editors, *Contemporary Design Theory: A Collection of Surveys*. Wiley, 1992.

[88] Rudolf Mathon and Alexander Rosa. Tables of parameters of bibds with r $\leq$ 41 including existence, enumeration and resolvability results: An update. *North-Holland Mathematics Studies*, 30:65–96, 12 1985.

[89] Rui Chao and Ben W. Reichardt. Quantum error correction with only two extra qubits. *Phys. Rev. Lett.*, 121:050502, Aug 2018.